Saltwater flushing from bathymetric hollows in a semi closed estuary

A study based on data from the Haringvliet

M.Sc. Thesis

17th of July 2024

University of Twente

Faculty of Engineering Technology

Department of Civil Engineering and Management

Summary

The Haringvliet estuary is semi closed in that it is separated from the sea by flood gates that since 2018 allow controlled saltwater intrusion to reduce the disruption induced by the original management strategy on the natural processes. While this is to the benefit of fish migration, it is also necessary to safeguard freshwater needs. Acknowledging that salt water can persist in estuarine bathymetric hollows, a dataset acquired by the University of Twente allows to address the conditions that induce the flushing of accumulated salt water.

Two bathymetric hollows are studied using records from three monitoring periods that repartition the winter of November 2022 to March 2023. The first two consider a bathymetric hollow that is more seawards in the estuary than that considered during the third. In each period, data from an Acoustic Doppler Current Profile [ADCP] pair are available alongside Conductivity Temperature Depth [CTD] time series collected from at least two depths. Further, at the start of each monitoring period a CTD profile is available at each ADCP that additionally incorporates a high resolution echosounder that can provide profiles indicative of the vertical density gradient.

The research objective is to study the flow dynamics through which salt water accumulated in bathymetric hollows is flushed out. This is approached by analyzing velocity and turbulence characteristics from the data collected in the Haringvliet estuary. More specifically attention is given to the delineation of the density interface to locate the main times at which an established interface is lowered. Thereby, the above and below interface depth averaged velocity parameters indicate the conditions required for flushing. Regarding the mechanisms associated to flushing, the study of along water column profiles of the velocity and turbulent kinetic energy [TKE] gives attention to the density interface tilting and the vertical shear induced TKE production that is compared to the TKE dissipation.

In the use of the ADCP data, the study of velocities remains more insightful than the turbulence statistics. For the prevalent conditions, it appears applicable to restrict the study of turbulence to the observation of along beam velocity variance to which the vertical beam lends itself the best. Indeed, while the found estimates of TKE production and dissipation rate need to be questioned in the low velocity environment, such that a TKE balance cannot be established, the calculated TKE and vertical velocity fluctuations are effective in indicating peak interfacial turbulence. The observations associated with saltwater flushing are however very different for both monitored locations.

At the most seawards hollow, the accumulated salinity reaches a level of around 5 PSU. Two events of interfacial lowering are observed with subsequent replenishment and a final complete flushing event. The latter and one of the former two are triggered by towards the sea directed overflowing currents of varying magnitudes that certainly do not need to be amongst the largest peaks observed. The prolonged nature of the flow velocity in the same direction appears more important and interfacial turbulence is only observed for times exceeding the effect of a single ebb, suggesting that first direct shear entrainment needs to settle the stratification. Indeed, as the interface establishes, the echosounder reveals interfacial instabilities that induce turbulent mixing that allows shear from the overflowing water to continue to transport salt water away from the interface due to a formed interfacial layer. This turbulent entrainment causes gradual interface lowering and as the salt layer is thinned the remainder is directly caried away by the induced overflowing water as the interface is broken up. The third event instead occurs while the water column is affected by the tidal cycle for which, in the estuary environment, the towards the sea directed

velocities do dominate the observed landward ones. Without observed interfacial peak turbulence upon the short time available for interface establishment under the ebb conditions, turbulent entrainment is not expected to contribute to the interface lowering. The only aspect in the available dataset that appears to set the flushing and non flushing times apart is the observed below interface dynamics. Indeed the systematic cycle of below interface flow orientations that is paired with the tidal one is disequilibrated during the flushing period. This only hints at the mechanism associated with the instability of the situation and the forcing that induces it is not retrieved.

The second hollow has a much more elongated geometry exceeding 5 times the length of the first for a comparable increase in depth relative to the surrounding bed level. Of the three times that salt water accumulates only once the interface is sufficiently raised for the CTDs to indicate an accumulated salinity peak of 1 PSU. In the absence of TKE peaking in the stratification transition region it is found that the shear exerted by the overflowing current tilts the horizontal interface indicated by the velocity profiles. Direct shear entrainment occurs that transports along salt water from the interface of which the density transition is gradual enough for the echosounder to not reveal its position which supposedly follows from the low density of the accumulated salt water. The observed behavior is also expected to link to how the hollow is more like a channel with direct shear just moving the salt water along in the downstream direction where its exit is to some extent restrained by the upward sloping bed out of the hollow.

At the Haringvliet estuary, it is possible to flush the observed accumulated salt water with a sustained towards the sea directed current without velocity magnitudes needing to be exceptionally high amongst those observed during the winter. However, this does require a sufficient supply of upstream freshwater availability. Indeed to completely flush the most seawards hollow with turbulent entrainment it takes a temporally averaged above interface overflowing velocity of 0.11 m/s over nearly four days. For the lower salinity accumulated in the other hollow, the most major flushing event takes 27 hours of direct shear entrainment with a temporally averaged forcing velocity of 0.10 m/s. Further, seeking to avoid salt water to accumulate appears possible as well because there are many occasions where there is saltwater inflow and inland directed currents at the hollow while no salt water accumulates.

Table of Contents

1. Introduction

Adopting a hard engineering approach to provide flood protection implies to directly disrupt the natural processes that are identified to induce the risk (Van der Nat et al., 2016). The acceptance of ecosystem based management challenges such an approach. It promotes the goal of preserving and restoring ecosystems alongside the target of utilizing their natural processes to the benefit of the societal problem that makes it necessary to intervene in the environment (O'Higgins et al., 2020). In addressing the societal concern of flood protection, the concept of ecosystem based management was not brought into practice with the construction of the flood gates that transformed the Haringvliet estuary to semi closed system. Indeed, controlling the outflow towards the sea while not allowing the opposite inflow tidal motion (Kranenburg et al., 2023) disregards natural processes.

For the existing flood gates, the effect these have on the local system is dictated by the management strategy. This is adjustable and accordingly can be formulated with ecosystem considerations in mind such that, in line with the ecologically enhanced hard engineering concept of Van der Nat et al. (2016), the negative effects from the artificial structure are reduced. Conform to this motivation, experiments with controlled saltwater intrusion are done since 2018 (Rijkswaterstaat, 2023c). Rijkswaterstaat, who is responsible for the floodgate operation, monitors the effect throughout the estuary.

The experimentation directed attention of research schemes to the area. One such field study temporally positioned a pair of five beam Acoustic Current Doppler Profilers [ADCPs] in former tidal channels while monitoring salinity levels with Conductivity Temperature Depth [CTD] sensors. ADCPs are vertical profiling instruments that allow to study how the water column evolves over time through derived flow velocities and estimated turbulence parameters (Stacey et al., 1999). Their deployment is justified by how in controlled estuary environments salt water in hollows can be an unwanted reserve at times when the active management desires to safeguard fresh water needs (Kranenburg et al., 2023). To clarify the research objective set to analyze this data set, the local problem definition is presented and put into context to restrict the focus conform to the scope that is tangible with the observations available.

1.1. Problem definition

Closing the Haringvliet estuary, located in the Rhine and Meuse delta, from the influence of the sea was part of the Delta Works initiated with the purpose of flood protection (Kranenburg et al., 2023). Thereby since 1970, the operation strategy destroyed the gradual transition between the saline sea and fresh water inland that is important for fish migration and serves as a habitat (Rijkswaterstaat, 2023c). Alongside the negative impacts on the natural dynamics that the operation of the floodgates caused (Buitenhuis & Dieperink, 2019), it also led to the estuary developing as an important source of fresh water (Kranenburg et al., 2023). Therefore, changing the original management strategy to allow controlled saltwater intrusion, can in turn have negative impacts on activities that evolved since the construction of the works (Kranenburg et al., 2023). In ecological restoration the two interests need to be balanced.

Research on the local response to an intervention is necessary to understand how management can meet the established policy objectives. For the Haringvliet, experimentation allows to obtain site specific details that complement theoretical understandings (Buitenhuis & Dieperink, 2019). It can inform the new management approach of controlled saltwater intrusion, reducing uncertainty such that support for the project can be gained (Buitenhuis & Dieperink, 2019). Under conditions that it is possible from the perspective of flood safety and estuarine salt content, the more natural salinity transition is sought to be

restored by also allowing the flood gates to remain partly open when the sea level exceeds that of the estuary (Rijkswaterstaat, 2023c). The choice of the opening extent differs upon the river discharge such that it is larger during high discharge periods then when there is less fresh water (Rijkswaterstaat, 2023c).

Kranenburg et al. (2023) study two bathymetric hollows in the Haringvliet estuary, demonstrating that at times of allowed saltwater intrusion this denser water can reach the deeper channel portions. When a subsequent period of freshwater discharge is allowed, as the water level of the estuary exceeds that at sea, a density interface establishes over the locally deeper hollow around the level at which the surrounding bed is. The discharging fresh water predominantly uses the water column portion that is above this interface, leading to the flow velocities below it to be relatively weak (Kranenburg et al., 2023).

Accumulated salt water can become difficult to flush from bathymetric hollows in the Haringvliet estuary (Kranenburg et al., 2023). The only gradual flushing observed by Kranenburg et al. (2023), with the higher during winter observed discharges, does indicate the reduced flushing potential for the seasons with traditionally lower upstream freshwater availability. When under too low upstream freshwater availability, the gates are kept closed and the estuary appears like a lake, it is possible that wind driven currents generate the shear required at the density interface to contribute to the flushing of salt water in the hollows (Kranenburg et al., 2023). These wind driven currents can subsequently be sufficiently strong to transport salt water from hollows in the upwind direction (Kranenburg et al., 2023). This can be problematic because the freshwater discharge needed to push salt water back to the sea is not always available during the spring and summer seasons (Kranenburg et al., 2023).

For the Haringvliet semi enclosed estuary, based upon the discussed observations from Kranenburg et al. (2023), it is relevant to study the flushing of accumulated salt water from two perspectives. The first is the management for timely flushing of salt water from the system towards the end of winter as freshwater discharges decrease. The second is the awareness of the potential for salt remaining in hollows to be washed out by wind driven currents at times of low freshwater discharge. A fundamental understanding of the flow conditions under which flushing occurs is relevant for both perspectives.

1.2. Context of relevance

The local problem definition gives a practical justification to be interested in the dynamics that can flush salt water accumulated in bathymetric hollows of the estuary. Experimentation at the Haringvliet can serve as a case study to inform other projects (Buitenhuis & Dieperink, 2019) and therefore has theoretical relevance. Local monitoring of the saltwater intrusion not only allows to devise context specific details but is also required to complement more general process understandings useful to manage the system.

To clarify the theoretical justification, it is appropriate to provide a short overview of the relevant literature. Established knowledge related to the topic is evidently used in the already introduced research of Kranenburg et al. (2023). Their discussion on the effect of external forcings, namely the discharge to the sea and wind induced currents, on the flushing of accumulated salt water from estuary hollows speculates on the importance of the density stratification interface tilting with a positive gradient along the flow direction. Context to this is given by the flume experiments of Debler and Armfield (1997) alongside Western et al. (1998) that, at a fundamental process level, identify that flushing of salt occurs through the interface tilting related downstream outflow layer and turbulent entrainment initiated by interfacial waves. While such small scale experiments indicate mechanisms of flushing, the forcings approach of Kranenburg et al. (2023) links the flushing with the conditions that influence the horizontal velocities.

The specific study of flow dynamics through bathymetric hollows has been undertaken from the perspectives of observations (Salas-Monreal & Valle-Levinson, 2009), using modeling (Roos et al., 2008), or a combination of both (Davies & Brown, 2007 and Cheng & Valle-Levinson, 2009). Despite variation induced by local conditions, these publications do tend to agree upon an underlying flow pattern that may be observed in hollows. However, these do not practically discuss flushing of accumulated salt. Greene et al. (2015) claim that in the study of flow dynamics, an ADCP allows to collect records that provide a suitable balance between the quantity of the data and the quality of the derived flow representative estimates. Extensive work has been done towards ADCP data processing by Stacey et al. (1999), De Serio and Mossa (2014) alongside Guerra and Thomson (2017), revealing the potential of the instrument to contribute to providing fundamental statistics on the velocity components and turbulent kinetic energy [TKE] alongside its production and dissipation rates. To complement this, a vertical ADCP beam allows to obtain profiles indicative of the stratification degree through the backscatter amplitude of the acoustic signals used (Kranenburg et al., 2023).

From linking the theoretical relevance with the practical justification in Figure 1 a research need is identified. A target contribution follows that can be addressed with the available ADCP observations. The actual Haringvliet data limits the realistic possible direct contribution to the research need because it would be required to study a broader range of hollow types and flow conditions to gain a potential generalizable understanding. The target contribution seeks to give an account of the observations, making connections with known physical process, taking a practice oriented research perspective to understand what the data allows to explain about large scale flushing.

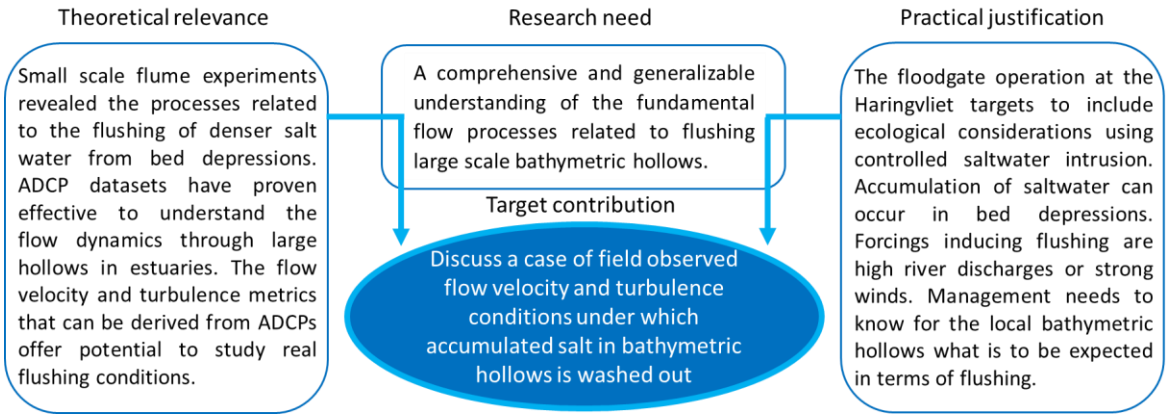

Figure 1: Identifying the research need and restrained target contribution.

1.3. Research objective and questions

Figure 2 clarifies the value that the available data, from the instruments positioned within a hollow, can have for the target contribution identified in Figure 1. Focusing on the bathymetric hollow as the system of interest, external forcings influence the datasets that provide the observations to study the relation between the density stratification and flow dynamics labeled as the research focus. The operation of the flood gates affects the influence that the forcings can have on the dynamics at the bathymetric hollow. These large scale morphological features can, for the context of the study, be perceived as static because they evolve over much longer temporal time scales than the flow velocities and turbulence associated with the competition between river feed fresh water and tidally forced salt seawater seconded by wind influences.

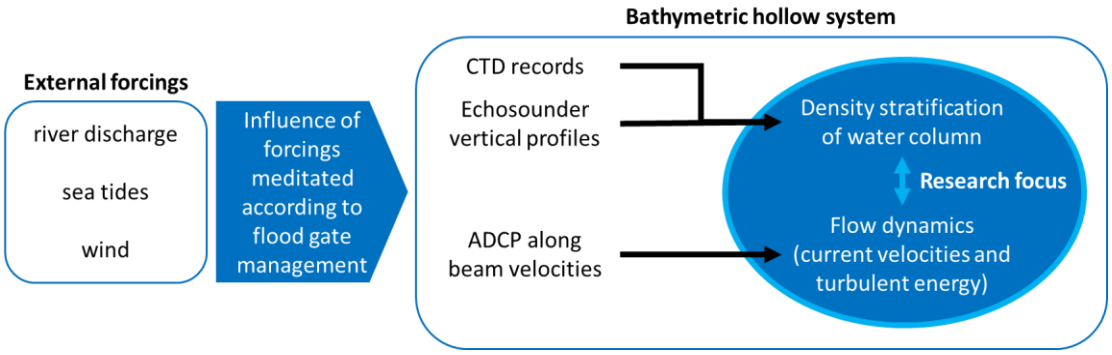

Figure 2: Identifying the research focus to address for the Haringvliet semi closed estuary.

The five beam ADCPs allow to derive vertical profile time series that characterize the flow velocity and turbulence. Because the instrument is equipped with an echosounder it can provide high resolution vertical profiles that are indicative of vertical density changes. However, while stronger retuned echo signals indicate a larger density transition, this is only an indirect observation of salinity. To put the echosounder data in perspective of water salinity, CTD sensor readings are available at specific depths along the water column and serve as a supporting dataset.

Setting the system boundaries as in Figure 2 allows to approach the topic of flushing salt accumulated in bathymetric hollows from fundamental flow descriptive values. By avoiding directly addressing the wider spectrum of causal relations involved in the estuary system, the research objective can be concentrated on the observed physics in the hollows such that its formulation is:

The research objective is to study the flow dynamics through which salt water accumulated in bathymetric hollows is flushed out by analyzing velocity and turbulence characteristics from data collected in the Haringvliet estuary.

In pursuing this research objective, the two way interaction between the flow metrics and an established density interface is of interest. A whole dataset understanding is needed for context before concentrating on the influence of the currents and mixing around the density interface established when there is accumulated salt in a hollow. To practically guide the research steps, these concepts are incorporated in the following main research question that is detailed by four sub questions increasing in specificity.

To what extent do flow velocity and turbulent energy vary with the vertical stratification across the water column to induce events of flushing out salt water accumulated in a bathymetric hollow?

- What are the flow velocity and TKE conditions at the times that the level of an established density interface is lowered?
- Which state of interface tilting and TKE production is observed in a hollow for a flushing event?
- Are interfacial waves involved in the transition from a stable interface to one in which the shear TKE production is not balanced by buoyant damping?
- To what extent, is it possible to use the ADCP data in the flow environment of the studied hollows to estimate the TKE dissipation rate for the comparison with the TKE produced in the context of the rate of change of TKE?

1.4. Report outline

Before describing, in Section 3, details on the study area and the monitoring scheme that produced the available data, a general theoretical background is presented in Section 2 on the flow dynamics and vertical stratification at hollows in estuaries in combination with the flow characterizing parameters that can be derived from ADCP data. To emphasize on the data preparation that precedes the analysis, Section 4 describes the processing steps, commenting on the activities and outputs. Section 5 subsequently presents the methodology, informed by the theory, applied to the prepared dataset to address the sub research questions for which the results are reported in Section 6. For coherence, the findings are commented on directly. Accordingly, this leaves for the discussion Section 7 the opportunity to take a more holistic view of the observations while drawing attention to the limitations of the performed analysis. This allows to transparently conclude with the main findings that contribute to answering the overall research question alongside finally listing relevant recommendations.

2. Theoretical background

The deployment of the ADCP pair in bathymetric hollows of the semi closed estuary provides a quantitative observation set upon which the application of data analysis techniques can allow to extract some information from. The literature mentioned in section 1.2, that informed the study orientation, provides the basis for the application of the data analysis techniques and the interpretation of the observations.

2.1. Vertical salinity stratification

Despite that the situation of interest is a semi closed estuary with controlled water fluxes, observations from natural estuaries, where the competition in the interaction between river fed fresh water and salt sea water dictates the stratification profile in the water column (Blaise & Deleersnijder, 2008), are insightful to understand the establishment and persistence of a vertical density stratification at a bathymetric hollow. There is a continuous natural dynamic that is part of a unique type of coastal ecosystem habitat with high biodiversity (Buitenhuis & Dieperink, 2019).

Stratification driving forces in natural estuaries

The velocity field, mixing patterns and stratification profiles in natural estuaries are dictated by the forcings of sea tides, river discharge and wind. When fresh and salt water are forced to interact, the density difference tends to establish a stratification along the water column (Simpson et al., 1990). In explaining the dynamics of vertical stratification profiles in estuaries the three concepts of density current flow, variable tidal mixing and tidal asymmetry in vertical shear are important (Simpson et al., 1990). These are respectively discussed below and summarized in Figure 3. Lange et al. (2020) acknowledge these, calling upon the horizontal density gradient alongside the friction effect at the bed and between fluid layers, but additionally emphasize on the role of wind.

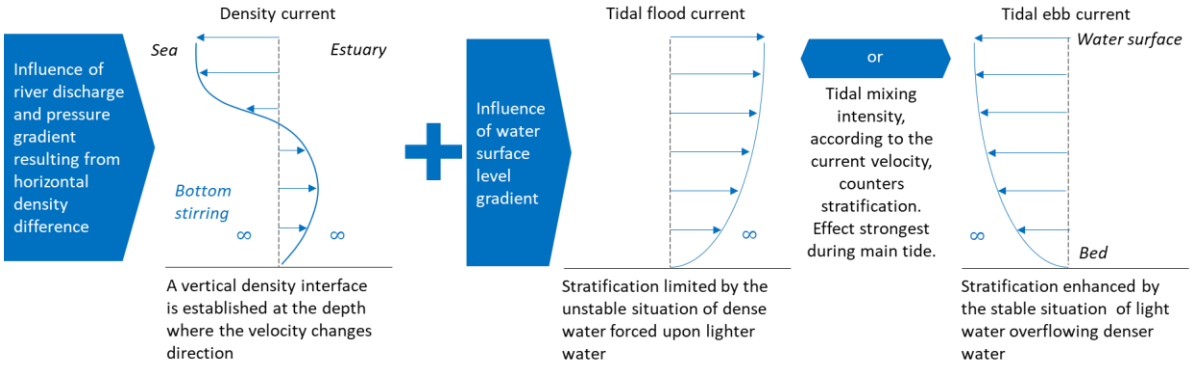

Figure 3: The velocity profile components relevant in estuary environments and their expected effect on the vertical density stratification.

The density current flow is linked to the horizontal density gradient established when a freshwater river discharges in a denser sea. Under this condition, the horizontal density difference establishes a pressure gradient of which the towards the river directed magnitude increases with depth (Fugate & Jose, 2019). Based on the buoyancy principle, the lighter fresh water from the river will tend to enter the sea near the surface while the stated pressure gradient induces a flow of salt water at deeper depths towards the river (Simpson et al., 1990). This is in turn partly opposed to by bed friction that induces bottom stirring (Simpson et al., 1990). The density current flow promotes an increased density towards the water layers near the bed than closer to the surface (Simpson et al., 1990). Thereby strong river discharge events

contribute to enhancing the stratification that can be seen to develop from the density current flow (Geyer et al. 2000). The strength with which it can be observed is however further affected by the variability in the flow and mixing related to the tide (Geyer et al., 2000).

Variable tidal mixing intensity is controlled by the magnitude of the tidal current velocity over the bed (Simpson et al., 1990). The water surface level gradient established between the tidal sea and the estuary induces a corresponding pressure gradient that drives either the flood inflow into the estuary or the ebb outflow (Blaise & Deleersnijder, 2008). Due to bottom friction the velocity profile tends to increase upward from the bed, at which bottom stirring dominates, according to a logarithmic profile (Kranenburg et al., 2023). The law of the wall provides a mathematical description of the along stream velocity u_{as} acting as a function of distance from the bed z based upon equation 1 (Petrie & Diplas, 2015). Thereby, $\kappa = 0.41$ is the von Karman constant and z_0 the level where $u_{as} = 0$ (Petrie & Diplas, 2015). Fitting a linear regression to the velocity as function of $\ln(z)$ allows to estimate the shear velocity u_{as}^*, defined as the square root of the ratio of the bed shear stress to the fluid density, that indicates the efficiency of the current to induce mixing (Petrie & Diplas, 2015). The amount of turbulence is highly variable over the tidal cycle because of the large differences in flow velocities (Simpson et al., 1990). During the time of the main flood or ebb current there is bottom friction induced mixing that limits the stratification that can be induced by the density current flow (Simpson et al., 1990). However, the bottom friction related mechanism becomes less relevant as the boundary layer occupies a less significant portion of the water column.

$$u_{as}|_z = \frac{u_{as}^*}{\kappa}\ln\left(\frac{z}{z_0}\right) = \frac{u_{as}^*}{\kappa}\ln(z) - \frac{u_{as}^*}{\kappa}\ln(z_0) \quad (1)$$

Tidal asymmetry is connected to the tidal cycle with its variable flow and mixing patterns (Geyer et al., 2000) and arises from the difference in the vertical shear induced by tidal velocity profiles at ebb and flood (Simpson et al., 1990). The vertical stratification undergoes a periodic cycle with its stability increasing during ebb and decreasing during flood (Simpson et al., 1990). Based upon the horizontal density gradient, during ebb conditions the induced velocity profile caries less dense water from the inland part of the estuary towards the denser sea. With the velocity profile having larger velocities near the surface than the bottom, a stable situation is created in which the less dense fluid flows over the denser one (Simpson et al., 1990). Instead, during flood, the saltwater column from the sea is moved into the estuary with larger velocities near the surface than at the bottom such that the shearing of a denser fluid over a less dense one creates an unstable situation (Simpson et al., 1990). The unstable shear generates strong turbulence along the water column (Geyer et al., 2000). Therefore, during ebb a clear stratification is expected while during flood the vertical profile is mixed such that the water column is less stratified (Geyer et al., 2000). If bottom friction induced mixing is also relevant, this counters the stratification induced by stable shear during ebb while for the flood it complements its breakdown (Simpson et al., 1990).

Winds with an along estuary component directed from the river mouth to the sea can increase the vertical stratification when the water is sufficiently deep, reinforcing the density current flow (Lange et al., 2020). Winds directed in the opposite direction, from the sea towards the fresh water of the river, oppose the horizontal density gradient driven circulation and may even reverse it (Lange et al., 2020). Rotational currents in the estuary can be expected for the combined action of the longitudinal and lateral wind components (Kranenburg et al., 2023). Thereby, the lateral component attenuates the straining discussed for either of the two, inland or seaward, pure longitudinally directed winds (Kranenburg et al., 2023). While wind can thus both induce straining and mixing depending upon its orientation, its effect can blend with the processes linked to the interaction between the tides and river discharge.

Vertical salinity stratification in bathymetric hollows

The bathymetry of the estuary contributes to where vertical stratifications can form and persist as induced by the stratification driving forces. Salt water can accumulate in the morphological feature of large circular to elongated bathymetric hollows that are a common feature in estuaries where the incoming tide can supply this salt water during flood conditions (Debler & Armfield, 1997). Indeed, Kranenburg et al. (2023) observe an established strong stratification with a distinct interface that separates the dense salt water in the hollow from the lighter portion above. Such an interface only becomes most distinct under the action of retreating ebb that enables the discharge of low salt content water predominantly across the upper part of the water column (Salas-Monreal & Valle-Levinson, 2009). A new incoming salt containing flood tide current would nevertheless again decrease the density gradient by increasing the salt content in the upper water column as well (Salas-Monreal & Valle-Levinson, 2009) for an estuary naturally exposed to the tidal cycle.

2.2. Flushing salt from bed depressions

To gain insight in the mechanisms that are relevant to flush salt water, from local areas with a lower bed level, experiments conducted in controlled environments are useful. Debler and Armfield (1997) alongside Western et al. (1998) use a flume to study what happens to dense water in a hollow once a freshwater flow is enabled to pass over it. Accordingly, the experimental observations on the formation of a saline outflow stream, that follows the bed downstream of the hollow, and turbulent mixing can be discussed before giving an account of large scale observations from estuarine bathymetric hollows. For reference a schematic overview of the main points of interest is included in Figure 4.

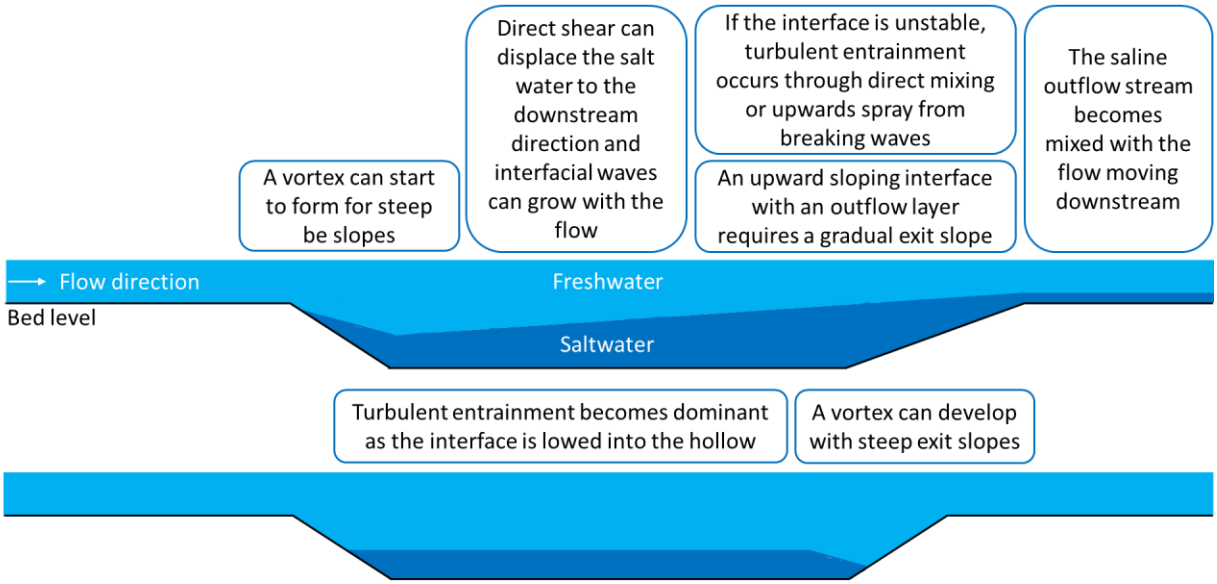

Figure 4: Schematic summary on the flushing of salt water from a hollow using the observations of Debler and Armfield (1997) alongside Western et al. (1998).

Saline outflow stream

In their laboratory experiments, Western et al. (1998), use a gradually sloping trapezoidal bed depression filled with salt water to observe that its removal, triggered by overflowing fresh water, is progressive and occurs through a thin stream of salt water flowing out along the downstream bed. The phenomenon is

explained by how, through the gentle slope, there is a gradual transition to the outside bed level which allows interfacial shear to transport the top denser fluid layer away (Debler & Armfield, 1997). As the threshold velocity of the fresh water to initiate the saline outflow stream is exceeded, the density interface remains linear and horizontal while not showing a pattern hinting at turbulence for which larger velocities are required (Western et al., 1998). This indicates that under laboratory conditions it is possible to observe a saline outflow stream not masked by turbulence. Because the saline outflow stream is reported to follow the bed, it is questionable how well this translates to an upscaled estuary environment where bed roughness is expected to influence the flow through turbulence, more rapidly prompting mixing of the outflowing saltwater stream. Indeed Western et al. (1998) do acknowledge that in their experiments the flume bed stress is negligible. However, the saline outflow stream does mix with the flow as it is moved along (Western et al., 1998).

The quantity of water caried by the saline outflow stream is strongest when the density interface is close to the level of the hollow exit (Debler & Armfield, 1997). This indicates that as the hollow is progressively being flushed, and thus the interface level is lowered, the direct contribution that the saline outflow stream can have to flushing decreases. It does also partly explain the immediate response to the sudden inflow of fresh water. Indeed, Debler and Armfield (1997) observe that the instantaneous introduction of the fresh water overflowing the dense layer, that completely fills the hollow, creates a surge wave that lowers the interface at the upstream while increasing its level at the downstream (Debler & Armfield, 1997). This initial response also applies to rectangular bed depressions (Debler & Armfield, 1997). However, if the observations are to be used in an upscaling context, the reported findings connected to the impulse of freshwater input are not relevant because the sudden release of water at the start of the experiments does not appropriately translate to a real environment where, according to Western et al. (1998), flows change more gradually.

Beyond the initial surge wave and while the amount of accumulated salt water is sufficiently large, the interface tilts due to the shear induced by a continuously overflowing current that strongly contributes to carrying along salt from the hollow (Debler & Armfield, 1997). From the tests of Western et al. (1998), the interface can be observed to tilt with a slight upwards slope in the downstream direction once the freshwater velocities overflowing the saline pool are sufficiently large to trigger the saline outflow stream that follows the downstream upward sloping bed out of the hollow. This explains that the upwards tilting of the interface is initiated from the downstream end of the hollow, to a degree that allows the interface at the downstream to be slightly above the outflow point (Western et al., 1998). In this case the saline outflow stream is the primary driver of saltwater flushing, but interfacial waves and associated turbulent mixing can be present if freshwater flow velocities are sufficiently large (Western et al., 1998). The observation of the interface tilting in experiments is possible because Debler and Armfield (1997) claim that the mixing layer tends to be thin, and therefore it can be expected that the density transition remains sufficiently distinct to notice a tilt.

Western et al. (1998) alongside Debler and Armfield (1997) agree by reporting that the upward slope at the downstream end should have a maximum inclination of around 20 degrees for the saline outflow stream, accompanied by overall interface tilting, to remain possible once the interface level is lowered into the pool. Such behavior is more expected for elongated hollows that tend to allow such bed slopes in natural conditions (Debler and Armfield, 1997). For short hollows, seiches can remove accumulated salt water and as the interface is lowered a circular motion can develop in the layers above the dense fluid inducing mixing through molecular diffusion and shear stress (Debler & Armfield, 1997).

Turbulence mixing

The flow of the fresh water over the denser fluid can produce waves between the two liquids which when they become unstable break to produce turbulent eddies (Debler & Armfield, 1997). The generated turbulence is effective to transport salt water from the instable interface to the overflowing fresh water that transports it away while incoming turbulence along the freshwater column itself has little effect on flushing (Debler & Armfield, 1997). The interfacial waves grow in amplitude moving downstream along the density interface and, accordingly, can cause surges in the quantity of salt water transported by the saline outflow stream (Western et al., 1998). The turbulent eddies, inducing mixing amongst the layers, can occur when a large enough velocity shear develops between the two layers compared to the density difference that seeks to keep the layers separated (Western et al., 1998). The degree of stratification of a water column is linked to the vertical mixing intensity which affects fluxes that can be observed in the water (Simpson et al. 1990) and thus also the transport of salt from a hollow. Indeed, the rate of the flushing is increased by more intense mixing, larger freshwater flow velocities, a larger overflowing fluid density and viscosity alongside a greater height of the overflowing water column (Debler & Armfield, 1997). Instead, the longer the hollow, the larger the vertical density gradient and the further the interface has already been displaced downward from its original position, the less flushing occurs (Debler & Armfield, 1997).

For hollows where the saline outflow stream can form, it can complement the turbulence related salt transport that on its own is also expected in hollows with steeper inclined sides. In the experiments of Debler and Armfield (1997), both mechanisms have about the same contribution to the overall saltwater entrainment when the hollow is still close to full. However, as the hollow is emptied further, the importance of the saline outflow stream component decreases more strongly than the turbulent mixing mechanism (Debler & Armfield, 1997). Debler and Armfield (1997) find that the density of the fluid near the bottom of the hollow does not change much during their experiment. This indicates that turbulent mixing is limited to the interface environment.

If a hollow has steep side slopes, it is possible to get vortex effects at both the downstream and upstream edges (Debler & Armfield, 1997). The influence of hollow edges becomes less important as the hollow length to depth ratio is increased (Western et al., 1998). Just upstream of the downstream side, the rapid reduction in available flow depth forces mixing to occur that can be very effective to remove accumulated salt (Debler & Armfield, 1997). From their experiments Debler and Armfield (1997) state that the effect becomes noticeable for downstream bed edge inclinations exceeding 30 degrees. Further, vortex shedding can occur at the upstream edge, as a result of flow separation induced by the sudden increase in available flow depth, to also induce local but intense mixing (Debler & Armfield, 1997). Because of this localized effect, the contribution to overall saltwater entrainment is limited for long hollows. For the flow separation to occur there should be a side slope decline exceeding 10 degrees with respect to the horizontal (Debler & Armfield, 1997). Further, as the density interface is situated deeper in the hollow, the vortex is weakened (Debler & Armfield, 1997). However, it should be acknowledged that the experiments only worked with freshwater currents characterized by Reynolds numbers much smaller than those expected in reality (Debler & Armfield, 1997).

Large scale flushing

Similar to the flume experiments, if the towards the sea directed velocity would persist in an estuary, an increase in the discharge of overflowing fresh water goes paired with a more rapid flushing of accumulated

salt water from a bathymetric hollow (Kranenburg et al., 2023). However, the large scale environment itself offers further opportunities to induce flushing, notably by the influence of wind.

In the absence of tidal influences and a dominant river discharge, as can exist for a semi closed estuary depending upon the management choice, the perceivable contribution of the wind to currents increases (Lange et al., 2020). When wind blows over an enclosed basin, the surface level may tilt, developing a pressure gradient that induces a vertical circulation that is marked by a current along the wind direction near the surface and an opposingly oriented one at greater depths (Kranenburg et al., 2023). Kranenburg et al. (2023) hypothesize specifically for hollows the expectation that the shear induced by the wind related current on the interface is not sufficiently large to prompt mixing at its level in the deeper sections of the bathymetry. Further, the oscillatory effect of wind driven surface waves is restricted to the upper portion of the water column and thus not expected to interfere with the density interface that can establish in deep hollows.

It is only when the interface in the hollow tilts that Kranenburg et al. (2023) believe that salt water can be removed from the hollow through the thin outflow stream over the downstream slope where it is further mixed with the fresh water. Indeed, the experiments of Western et al. (1998) show that turbulence only develops at flow velocities higher than those necessary to induce an interface tilt. The incline can follow from the established wind driven circulation, where the surface current flows in the opposite direction as its deeper counterpart, for a sufficiently deep enclosed basin (Kranenburg et al., 2023). The tilting can itself induce two circulation cells of which the one below the interface is the weakest (Kranenburg et al., 2023). In such circumstances, the tilt tends to be more noticeable than the water surface tilt that is inclined in the opposite direction (Kranenburg et al., 2023).

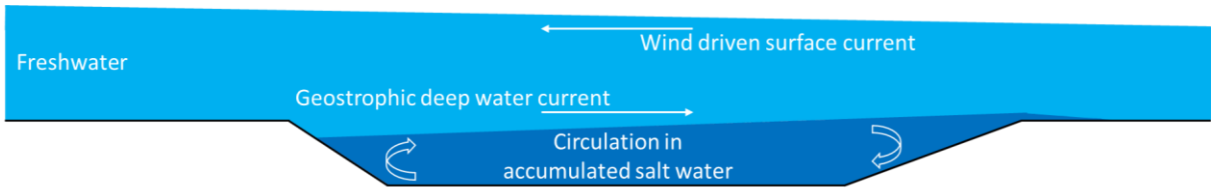

Figure 5: Two dimensional schematic illustration of the possible two cell circulation described by Kranenburg et al. (2023) that stems from the wind driven surface current with the pressure driven geostrophic return flow.

2.3. Stability of the density stratification

Kranenburg et al. (2023) observe that for a vertically stratified water column at a bathymetric hollow, the density difference becomes adjoint to a velocity transition between the faster overflowing currents and the more stagnant water below the interface. This condition of vertical shear allows instabilities to establish at the interface (Van Gastel & Pelegrí, 2004). The concept of the Richardson number ratio is useful as an indication of when the velocity shear overcomes the stratification such that instabilities induce mixing (MacDonald & Geyer, 2004).

Gradient Richardson number

To characterize the stability of a density interface, the gradient Richardson number R_g [-] is a practical criterion and calculated, according to Van Gastel and Pelegrí (2004), by equations 2 to 4. In this formulation, N [1/s] is the buoyant frequency and S [1/s] the vertical shear. While S is presented as

featuring the velocity gradients from both horizontal velocity components, Salas-Monreal and Valle-Levinson (2009) alongside Kranenburg et al. (2023), who work with ADCPs, use $S = \delta u_{ch}/\delta z$ where u_{ch} [m/s] is the along channel horizontal velocity component. Further, the term ρ_0 is a representative mean density (Wells and Troy, 2022).

$$R_g = N^2/S^2 \tag{2}$$

$$N = \left(-\frac{g}{\rho_0}\frac{\delta\rho}{\delta z}\right)^{0.5} \tag{3}$$

$$S = \left(\left(\frac{\delta u}{\delta z}\right)^2 + \left(\frac{\delta v}{\delta z}\right)^2\right)^{0.5} \tag{4}$$

The buoyancy and shear forces have opposite effect on turbulent mixing. A stronger density gradient damps TKE while a higher velocity gradient is associated to stronger shear that produces TKE (Krvavica et al., 2016). The gradient Richardson number thus represents the ratio of the stabilizing to the destabilizing force and indicates if the flow at the interface is subject to instabilities (Krvavica et al., 2016). The critical value of R_g marks this threshold and takes a value around 1, which is precisely used in the descriptions of Van Gastel and Pelegrí (2004) alongside Kranenburg et al. (2023). The larger the values of R_g , the more distinct the stratification and thus the lower the amount of turbulent mixing at the interface (Krvavica et al., 2016).

Alternative definitions of the Richardson number exist. Krvavica et al. (2016) use the shear layer Richardson number R_s [-], defined in equation 5, as an estimate for R_g when velocity profiles are not available. When R_s becomes inferior to the critical 1.2 threshold turbulent mixing occurs (Krvavica et al., 2016). Noteworthy is that this value thus is larger than the 1 taken by Van Gastel and Pelegrí (2004) and Kranenburg et al. (2023) suggesting that the shear layer Richardson number estimate could systematically exceed that of a properly calculated R_g.

$$R_s = \frac{g(1-r)i}{c^2} \tag{5}$$

In the formulation of equation 5, r [kg/m^3] is the homogeneous density of the layer overflowing that of the interface divided by the density of that below it. The term c [m/s] is the difference in velocity between those upper and lower layers. Krvavica et al. (2016) use the assumption that the width of the shear layer i [m] is equal to the thickness of the interface that they obtain from salinity profiles by considering the depth range between 0.25 and 0.75 times the maximum salinity value.

Instabilities at the density interface

With their field observation program set in an estuary, MacDonald and Geyer (2004) observe Kelvin Helmholtz billows initiating turbulence generation as the fresh water overflows the salt water during ebb conditions. In the more controlled setting of a flume, Sullivan and List (1994) make a distinction between interfacial wave breaking, Kelvin Helmholtz to turbulence instabilities and link these regimes to the state of interface stability. Figure 6 summarizes these

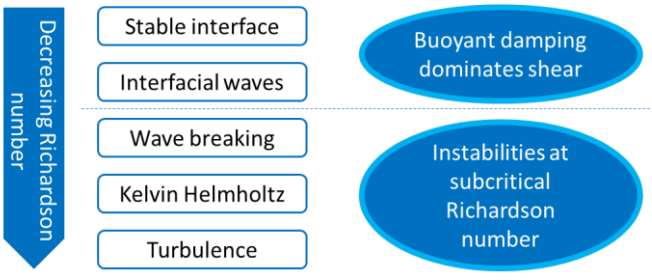

Figure 6: Progression of stability of the vertical density stratification.

concepts. Indeed, for low values of the Richardson number, large scale disturbances of the interface brought forward by turbulent instabilities at the interface tend to be present. It is only when the Richardson number increases, coupled to a decrease in the scale of the turbulent eddies, that Kelvin Helmholtz instability can become perceivable. As the interface further stabilizes for still higher values of the Richardson number, mixing of the stratified water column becomes attributable to breaking interfacial waves (Sullivan & List, 1994). For even larger Richardson numbers, as the interfacial waves tend to reach their finite amplitude less, the mixing contribution of the interfacial waves is suppressed and the interface becomes more stable (Sullivan & List, 1994).

Internal waves in open oceans can exist with undulations in the range between the buoyant and Coriolis frequency (Garrett, 2001). While the latter is irrelevant, in the case of a semi closed estuary, it follows that oscillatory patterns possible at the interface should exceed the buoyant frequency. For waves near this frequency, where buoyancy is the main restoring force, the fluid motion associated to it is nearly vertical (Garrett, 2001).

Interfacial waves tend to resort from turbulent fluctuations in pressure within the layers adjacent to the interfacial one (Sullivan & List, 1994). The vertical water column portion affected by interfacial wave breaking events tends to be smaller than that affected by the Kelvin Helmholtz instability (Sullivan & List, 1994; Van Gastel & Pelegrí, 2004). For wave breaking instabilities, a small cloud of mixed fluid is formed above the interface that is then further taken up by the overflowing layers (Sullivan & List, 1994). Instead, for Kelvin Helmholtz instabilities, such an observed cloud grows until turbulence can no longer be sustained within it (Sullivan & List, 1994). The phenomenon of Kelvin Helmholtz instabilities is closely linked to the Richardson number because these occur as the stabilizing buoyancy force is insufficient to compensate for that induced by shear from the overflowing velocities (Sullivan & List, 1994). Further going into the turbulent instabilities, the presence of larger eddies that mix the denser fluid at the interface to the overflowing layer goes paired with the establishment of a layer with intermediate density such that the transition is smoothed between the extremes (Sullivan & List, 1994). The associated lower density gradient appears well linked with the low Richardson numbers while Sullivan and List (1994) further observe that the Kelvin Helmholtz instabilities contribute to the interface thickening.

2.4. Flow in bathymetric hollows

Next to the interrelation between the currents and the vertical stratification, the shape of the large scale hollows in estuaries also dictates the flow patterns. Before considering how this too is affected by local density gradients, the basic situation where a freshwater current encounters a hollow is addressed.

Density homogeneous water

The constraint imposed by the finite width of a bathymetric hollow can induce flow contraction, as the current enters the hollow, which translates to an increased flux of water over the hollow (Roos et al. 2008). The additional flux is feed by lateral flow entering the hollow near the upstream side that comes from established recirculation cells (Roos et al. 2008) schematized in Figure 7. To explain the recirculation, Roos et al. (2008) note how continuity would specify that the increase in depth would decelerate the flow, which subsequently, according to the principle of Bernoulli, is accompanied by an increased longitudinal along flow pressure. This is a two dimensional perspective and a more evolved insight becomes apparent when linking the implications of this to three dimensions. With the restricted width of the hollow an associated lateral cross flow pressure gradient needs to coexist. From the lateral momentum balance Roos et al.

(2008) identify that this leads to a lateral velocity diverted outward from the longitudinal flow axis of which the magnitude increases toward the end of the downstream side of the hollow. This is the input for the recirculation that occurs around the hollow that ends with the previously mentioned lateral inflow near the upstream side. Thus, on one side of the hollow there is a counterclockwise recirculation while on the opposite side there is the clockwise counterpart of which the symmetry can be affected by the Coriolis effect (Roos et al. 2008). However, for an increase in flow velocity to be possible through the hollow, the bed depression should be sufficiently large to accommodate the recirculation while the lateral water influx to the upstream side should be enough to influence the flow (Roos et al., 2008).

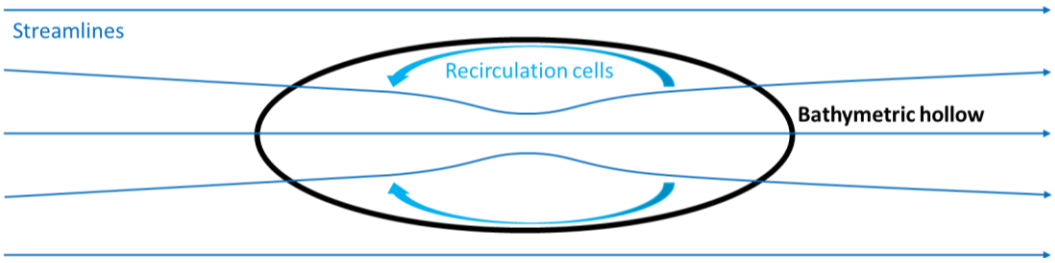

Figure 7: Using streamlines to illustrate the flow contraction over an ellipsoidal hollow where recirculation cells can potentially become established based upon a concept from Salas-Monreal and Valle-Levinson (2009).

Density stratified water

The horizontal density gradient established along estuaries can affect the flow dynamics in a bathymetric hollow with the flow field differing under ebb and flood conditions (Cheng & Valle-Levinson, 2009). During flood tides, where the density of the water decreases along the flow direction, there is an increased velocity along the lengthwise component as the incoming water flows over the deepest portion of the hollow, with maximums attained just after the deepest point when following the inland directed current (Cheng & Valle-Levinson, 2009). The flow acceleration during flood can theoretically be explained with the three dimensional flow dynamics concept (Cheng & Valle-Levinson, 2009). This phenomenon, introduced above for non density stratified water, is similarly captured by Davies and Brown (2007) who also report on the convergence as the flow enters the estuary hollow and the subsequent divergence upon exit, attributing their observation to the hollow influencing the regional pressure field. Opposed to the behavior during flood tide, the ebb outwash flow velocity decreases as it interacts with the hollow (Cheng & Valle-Levinson, 2009). Not bringing in that the hollow has a finite width leaves a two dimensional approach that thus mathematically stops at the continuity and Bernoulli step in the three dimensional description of Roos et al. (2008) that by default leads to flow deceleration with the increase in depth. However, neither the two or three dimensional perspective offers a comprehensive way to reproduced the observations.

Cheng and Valle-Levinson (2009) show that the inclusion of the horizontal density gradient in numerical experiments, that focus on a well mixed vertical environment and solve momentum and continuity balances, allows to explain the ensemble of their field observations for both tidal conditions. Thereby, the decrease and increase in flow velocity during the respective ebb and flood tide are more extreme than the flow alteration predicted to be induced by the hollow in the absence of a horizontal density gradient (Cheng & Valle-Levinson, 2009). However, the vertical stratification can further influence the flow structure in environments that are not fully mixed (Cheng & Valle-Levinson, 2009). When modeling a highly stratified estuary with a vertical stratification at the hollow, Cheng and Valle-Levinson (2009) still find that it is possible to obtain a velocity increase for the flood tide and a decrease for ebb.

It should be noted that the control experiment, where there is no horizontal or vertical stratification, of Cheng and Valle-Levinson (2009) achieves a velocity reduction in the hollow compared to the surrounding. This contradicts the results produced by Roos et al. (2008) for non stratified flow. Therefore it requires an explanation because the recirculation, previously discussed for the three dimensional case of homogeneous water based on Roos et al. (2008), also returns in the observations of Cheng and Valle-Levinson (2009). Indeed, Cheng and Valle-Levinson (2009) recognize a two cell recirculation in each of their three numerical experiments that range from no horizontal stratification to the density gradient accompanying the flow or opposing it. Cheng and Valle-Levinson (2009) state that the convergence phenomenon is most distinctly present in the flood flow case and the least in the ebb flow situation, with the control situation being situated in the range that is in between. Therefore, the circulation phenomenon is modeled, and the degree of flow contraction coincides with the sequence of lowest to highest flow velocity. This suggests that for the data of Cheng and Valle-Levinson (2009), the two dimensional perspective of Bernoulli dynamics dominates the three dimensional recirculation that follows from it. A careful consideration of local conditions is essential when formulating an interpretation.

To emphasize upon how each situation is unique it can be mentioned that Salas-Monreal and Valle-Levinson (2009) find that, for both flood and ebb conditions, there is the acceleration of the flow as it enters the hollow towards the deepest part and the subsequent deceleration upon the exit. Thereby the formation of lee waves is possible and can cause the density interface to tilt downwards (Salas-Monreal & Valle-Levinson, 2009). As such this appears a larger scale version of the upstream vortex effect also reported in the flume experiments and reported in Figure 4 as a downward inclined interface.

Influence of hollow shape properties

The hollow dimensions affect the degree of velocity alteration the morphological feature induces, but the geometry contribution also depends on the state of the horizontal density gradient. Through incorporating this in the three dimensional flow description, Cheng and Valle-Levinson (2009) find that under flood conditions an increase in the depth of the hollow produces larger velocities. Instead, during ebb, lower velocities would be the result while this also holds for a homogeneous flow environment (Cheng & Valle-Levinson, 2009). To put this in perspective, Cheng and Valle-Levinson (2009) claim flow enhancement under flood conditions while a reduction under the other two. Accordingly, it appears more general to state that deeper hollows can exert a greater influence on the local flow condition. Therefore, it is expected that the behavior that can be observed for a shallower hollow is exaggerated in a deeper one.

Turning to the hollow shape, a wider hollow makes it less important to mathematically consider the across flow finite span of the hollow. Therefore, when there is no horizontal density gradient, wider circular hollows will feature lower velocities than their narrower elliptical equivalents. The flow acceleration or deceleration linked to a horizontal density gradient further becomes more attenuated as the width of the hollow is increased (Cheng & Valle-Levinson, 2009).

2.5. Acoustic Doppler current profilers

Multiple analysis possibilities exists for processing the along beam collected time series to understand the evolution of the water column based upon the sampled depths. Measurements collected with an ADCP allow to derive the horizontal velocity components, estimate turbulence parameters (Guerra & Thomson, 2017) and obtain vertical profiles indicative of the stratification degree (Kranenburg et al., 2023). To give context to the parameters that can be derived, first the way the ADCP collects data is covered.

Along beam data

Each of the beams of an ADCP has a platform that emits acoustic pulses and collects the signal that is returned after it has been reflected off particles in the water (Stacey et al., 1999). The movement of these particles makes that the reflected signal is Doppler-shifted whereby the phase shift is related to the velocity of the element on which the signal reflected (Stacey et al., 1999).

Figure 8 schematically shows the beam configuration for a five beam ADCP. The four slanted beams sample with an inclination of θ [deg] to the horizontal. When using the beams in the derivation of a quantity, awareness of how the pitch and roll of the instrument affect the orientation of the beams through the water column is relevant. A positive pitch implies a rotation around the y axis such that the positive side of the x plane is rotated upwards. Similarly, positive roll describes a rotation around the x axis by which the positive y plane is rotated upwards.

Near the ADCP, turbulence due to flow interferences with the measuring device can not be ruled out and is a possible explanation for abnormal results at the bottom of the measured column (Geyer et al., 2000). More generally, near the bed or water surface, these boundaries are limiting factors to the sizes of eddies that characterize turbulent motions (Stacey et al., 1999). Because the vertical velocity component must be present in turbulent flow, while it tends to be a weak element of other flow regimes, the inclusion of beam *e* is important for the turbulence statistics that can be derived from the ADCP measurements (Greene et al., 2015). The vertical sampling spacing resolution is however a limiting factor to the size of eddies that can contribute to the observed along beam velocity (Stacey et al., 1999). Indeed, eddies inferior to at least twice the size of the vertical bins averaged over, to obtain the values at the representative along water column sample points, will not be resolved because their effect on the resulting velocity is smoothed out (Stacey et al., 1999). Because turbulence is dominated by the larger eddies, the sampling size does not need to be an issue to study TKE (Stacey et al., 1999). Nevertheless, when utilizing ADCPs in stratified flow environments it should be acknowledged that this can restrict the size of the eddies such that smaller ones are to be expected relative to an unstratified situation (Stacey et al., 1999).

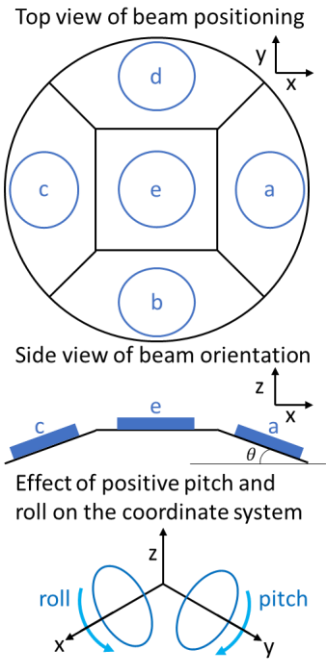

Figure 8: Beam arangement of a five beam ADCP, based on Nortek (2017)

Vertical stratification

It is possible to use the acoustic backscatter to study density interfaces and their displacements (Stacey et al., 1999). The backscatter amplitude from the vertical ADCP beam characterizes how strongly the signal is reflected and accordingly is representative for how dense the water column is (Kranenburg et al., 2023). The stronger the density difference the higher the signal produced (Gostiaux & Van Haren, 2010). However, additional sensors are required to calibrate the backscatter signal to a physical quantity that is of interest (Gostiaux & Van Haren, 2010).

Because no actual salinity or density data is recorded, particles or elements in the flow more generally affect the observations. Indeed, it is common that sediments in the water column affect the backscatter (Kranenburg et al., 2023). The vertical profiles indicative of the stratification degree that can be obtained

with the backscatter are restricted in resolution by the beam vertical sampling cell size. A dedicated echosounder integrated in the ADCP, next to the vertical oriented fifth beam, labeled with e in Figure 8, can collect higher resolution data (Nortek, 2017).

Horizontal velocities

The two pairs of slanted beams allow to derive the horizontal velocity components by how the beams in a pair are inclined in opposite direction. The vertical velocity component w [m/s] is directly known from the fifth vertical beam (De Serio & Mossa, 2014). Referring to the beam labeling of Figure 8 the along beam velocities b [m/s] are used to identify the instrument based x an y velocity components of u and v [m/s]. Stacey et al. (1999) prescribe equations 5 and 6 when the along beam velocities directed towards the instrument take the positive values.

$$u = \frac{b_c - b_a}{2\sin(\theta)} \tag{5}$$

$$v = \frac{b_b - b_d}{2\sin(\theta)} \tag{6}$$

The raw data of along beam velocity measurements tends to be averaged over time using an interval of 5-10 minutes to ensure stationary mean flow conditions (Guerra & Thomson, 2017). The averaging is claimed to reduce the random Doppler noise inherent to the instrument observations that rely on the use of acoustic beams (Guerra & Thomson, 2017). Guerra and Thomson (2017) settle on using an averaging period of 10 minutes which is judged short enough so that the current does not change, allowing to claim stationary, and long enough to allow to observe large scale turbulence (Guerra & Thomson, 2017).

Reynolds decomposition

Reynolds decomposition allows to define each velocity time series as the sum of its mean and a remaining series of fluctuating quantities (Stacey et al., 1999). For the instrument coordinate based x, y and z velocity components this gives $u = \bar{u} + u'$, $v = \bar{v} + v'$ and $w = \overline{w} + w'$. To calculate a Reynolds stress, the negative fluid density ρ [kg m^{-3}] is multiplied with the mean of the product between two velocity fluctuations, also termed the covariance (De Serio & Mossa, 2014). Based upon the three velocity components, nine covariance combinations can be made that are presented in matrix form in equation 7.

$$Reynolds\ covariances = \begin{bmatrix} \overline{\boldsymbol{u'u'}} & \overline{\boldsymbol{u'v'}} & \overline{\boldsymbol{u'w'}} \\ \overline{v'u'} & \overline{\boldsymbol{v'v'}} & \overline{\boldsymbol{v'w'}} \\ \overline{w'u'} & \overline{w'v'} & \overline{\boldsymbol{w'w'}} \end{bmatrix} \tag{7}$$

Only six elements of the matrix are unique, shown in bold, because the mirrored elements are equal. Those along the diagonal are in principle just the variance for the velocity component, being the covariation between the same term, and therefore are further referred to as the normal Reynolds covariances. The other three terms are the shear Reynolds covariances.

Combining the slanted along beam velocities in the calculation of u and v time series does not leave the series properly representative of the inherent flow variability that can be observed, making it unsuitable in the study of turbulence. Indeed Stacey et al. (1999) claim that turbulence statistics should be found by using the observed variances in the along beam collected data (Stacey et al., 1999). However, the inclined beams sample the water column at increasingly large distances apart when moving vertically away from the ADCP (Stacey et al., 1999). It is likely that at a particular time each of the beams will be sampling its velocity data records based upon different local turbulent eddies (Stacey et al., 1999). The sampled

instantaneous velocity field is therefore inhomogeneous, implying that the along beam velocity data does not together characterize a common condition such that it is not directly usable to calculate turbulence statistics. The variance method offers a solution to cope with this instantaneous inhomogeneity (Stacey et al., 1999).

To calculate the Reynolds covariances, the variance method combines the along beam velocity variances $\overline{b'^2}$ [m^2/s^2], computed over a selected interval of time such as 10 minutes, of opposite beams (Stacey et al., 1999). In this sense the variance technique seeks to relate the mean and variance statistics of beams which in turn only requires the assumption of homogeneity for these two statistics in amongst beams (Stacey et al., 1999). Complementarily to this, De Serio and Mossa (2014) also emphasize that the turbulence statistics should be steady across the interval employed to find them. To identify if the homogeneity assumption in the two statistics is justifiable, Stacey et al. (1999) first claim that it is the change in bathymetry that dictates the length scale over which variation in the flow field can be expected. Subsequently verifying if this length scale amply exceeds the spread of opposite beams, characterized by $2Hsin(\theta)$, can allow to state that homogeneity is sufficient (Stacey et al., 1999). The term H [m] is the water depth extent over which the ADCP is sampling.

Instead of the formulation employed by Stacey et al. (1999) for the four beam ADCP, Guerra and Thomson (2017) elaborate on the variance method for a five beam configuration that allows for a direct estimation of five out of six of the unique Reynolds covariances. However, in the relations for two of the shear Reynolds covariances the unknown third $\overline{u'v'}$ is used. To cope with this, Guerra and Thomson (2017) use the derived u and v in instrument coordinates directly in a covariance calculation to obtain an estimate of $\overline{u'v'}$. However, this approach is questionable and it can be avoided if the instrument is horizontally positioned. Indeed the equations of Guerra and Thomson (2017) include parts dependent upon the pitch and roll to account for the instrument tilt. Equations 8 to 12 are simplifications, applicable when the pitch and roll are zero, of the equations presented Guerra and Thomson (2017) that are corrected by consulting Dewey and Stringer (2007).

$$\overline{u'u'} = \frac{\overline{b_c'^2} + \overline{b_a'^2} - 2\cos^2(\theta)\,\overline{b_e'^2}}{2\,sin^2(\theta)} \quad (8)$$

$$\overline{v'v'} = \frac{\overline{b_b'^2} + \overline{b_d'^2} - 2\cos^2(\theta)\,\overline{b_e'^2}}{2\,sin^2(\theta)} \quad (9)$$

$$\overline{w'w'} = \overline{b_e'^2} \quad (10)$$

$$\overline{u'w'} = -\frac{\overline{b_c'^2} - \overline{b_a'^2}}{4\,sin(\theta)\,cos(\theta)} \quad (11)$$

$$\overline{v'w'} = -\frac{\overline{b_b'^2} - \overline{b_d'^2}}{4\,sin(\theta)\,cos(\theta)} \quad (12)$$

The simplified equations of $\overline{u'w'}$ and $\overline{v'w'}$ presented by Guerra and Thomson (2017) do not exactly reduce to those formulated by Stacey et al. (1999) for a four beam ADCP when accounting just for the differences in beam labeling in the $x\ y$ plane. There is a difference in sign despite that Appendix 1 shows that both forms can be correctly mathematically derived. However as explained in Appendix 1 there is an interpretation side to the problem as well that allows to conclude that the subtraction order of the along beam variances should be based upon the beam positioning in the context of the positive axis orientation. Thereby subtracting the beam that is further towards the positive axis side from the one is further towards the negative axis side allows to obtain a positive Reynolds stress when the observed velocity variance

increases along the positive flow direction. This, for the beam set up of Figure 8, would imply that the negative sign in front of equations 11 and 12 is removed.

Because the pitch and roll correction included in the equations of Guerra and Thomson (2017) is omited in equations 8 to 12, it is relevant to consider alternatives to address the tilt more fundamentally by considering the along beam velocities directly, which is thereby also valuable for the derived horizontal velocity components. With a tilted instrument, it follows that the beams will not be sampling at corresponding depths for the same cell number away from the ADCP. Although the results are reported for the expected cell size that applies to when the instrument is leveled, the tilting of the equipment alters the cell size (Nortek, 2017). For a pair of opposite beams one real cell extent is thus reduced while the other is increased. Pitch and roll become a problem when the inclination of the instrument is such that sampled positions in the water column are shifted beyond the cell size (Nortek, 2023). In this case two cells with the same number no longer sufficiently match, with respect to the sampling resolution, in terms of the depth they represent. A possible way to deal with instrument tilt directly when the data is still in the form of along beam velocities is referred to by Nortek (2023) as bin mapping. This principal advocates to adjust the cell numbering on the beams so that corresponding numbers relate to a similar depth level again.

Doppler noise in the frequency domain

The along beam velocities recorded by the ADCP feature an instrument inherent Doppler noise (Stacey et al., 1999). This noise stems from the use of acoustic signals to sample the water column. It is expected that the noise is white such that its spectrum is horizontal in the frequency domain (Greene et al., 2015). More specifically, the white noise can be expected to be Gaussian (Stacey et al., 1999). Gaussian white noise implies that the randomness is characterized by a symmetrical Gaussian distribution centered around a zero mean with a spread represented by a constant standard deviation (Balakrishnan & Mazumdar, 2011).

The measured along beam velocity is the sum of the actual velocity plus the random white noise (Stacey et al., 1999). Thereby, the noise affects the signal variance, influencing the along beam velocity variance estimates calculated from the observations. Therefore Guerra and Thomson (2017) mention that it is common practice to remove detectable white noise that can be expected to be the same for all beams (Stacey et al., 1999). Because the random noise in the ADCP records is uncorrelated with the actual velocity it applies that $\overline{b'^2_{corrected}} = \overline{b'^2_{observed}} - \overline{b'^2_{noise}}$ (Greene et al., 2015).

To identify $\overline{b'^2_{noise}}$ Greene et al. (2015) prescribe to use spectral analysis on several selected time windows, across the different beams, over which the mean and variance are stationarity. Spectral analysis relies on applying the Fourier transform to transfer the along beam velocity fluctuations time series, obtained by removing the mean followed by the potential application of a taper to reduce spectral leakage, to the frequency domain (Davis, 2002). It exploits the concept that a time series can be represented by the sum of a set of cosine waves that have different frequencies and amplitudes (Davis, 2002). Spectral analysis allows to produce a periodogram that represents the variance in the series at each frequency up to the Nyquist frequency f_N that is dictated as half the instrument sampling frequency (Davis, 2002). Therefore, a periodogram produced based upon an along beam velocity time series shows for each frequency f [Hz] the along beam velocity variance S [(m/s)^2/Hz] that the associated signal explains and as such can uncover dominant cyclic patterns. Based upon the area of interest, different smoothing strategies can make the periodogram more accessible. Segment averaging can be employed if the studied phenomenon persists in

time and periodograms obtained over consecutive segments of the overall series can be averaged (Davis, 2002). Alternatively bin averaging is possible when variance values at consecutive frequencies are correlated (Lewis, 1970). The averaging weighting scheme applied in the smoothing is suggested to be uniform by Lewis (1970) when interested in a linearly varying pattern as opposed to peak identification oriented weighting choices.

Taking the mean over the periodograms produced per beam for a certain time window, allows to obtain an estimate of the average spectral density of the along beam velocity (Greene et al., 2015). The part of the spectrum that flattens out at high frequencies describes the white noise and the average value of this horizontal portion $\bar{S}$ can be used in $\overline{b'^2_{noise}} = (f_N + f_t)\,\bar{S}$ (Greene et al., 2015). In this expression f_t is the inverse of the time window period used (Greene et al., 2015). When f_t is small, $\overline{b'^2_{noise}} = f_N\,\bar{S}$ (Greene et al., 2015). This gets fundamentally back to how the area under the periodogram reflects the variance in the time series.

Turbulent kinetic energy

Turbulence related to the stratified water column and bed shear is important in the flow dynamics of estuaries (Stacey et al., 1999). The values that the TKE production and dissipation rate have, alongside total TKE, are dictated by the stage in the tidal cycle and tend to increase with velocity (Guerra & Thomson, 2017). The TKE balance allows to have an overview of the components that can be expected to contribute to the rate of change of TKE that is characterized by the sum of the terms shown in Figure 9.

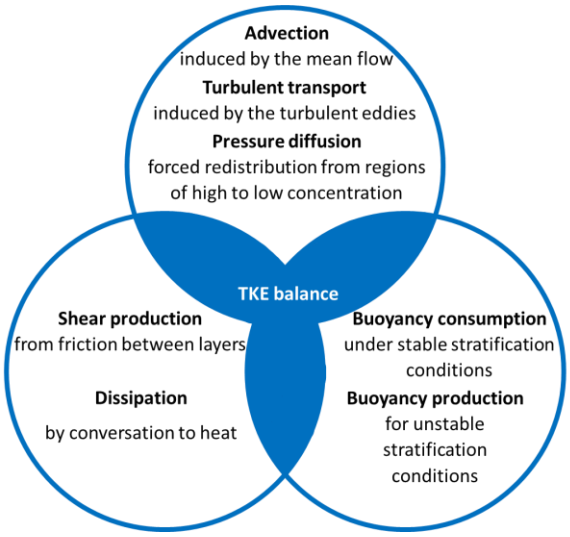

Figure 9: Components of the TKE balance, based upon concepts from Aupoix et al. (1990)

Figure 9 categorizes the elements of the TKE balance into three spheres. The sphere containing dissipation and shear production indicates the components that can be studied with ADCP data. Instead, the sphere at the top pertains to the TKE that is present and is being moved around. An ADCP allows to study the flow through an Eulerian perspective and thereby can provide insights regarding how TKE interacts with the local water column while being insufficient to track TKE movement. It is noteworthy that Stacey et al. (1998), studying turbulence in stratified estuaries, refer to the TKE budget as a balance between the production through shear, dissipation through viscosity and a buoyancy term. Thereby they do not allude to the components in the sphere at the top of Figure 9. This prompts the idea that when interested in the interaction between the TKE and the stratification it is not how TKE is moved along by the flow that is of direct concern.

In shear dominated flows the dissipation rate is close to the production (Stacey et al., 1998), indicating that for such flows the buoyancy term is relatively small. Indeed, when dissipation and shear production rates of TKE do not balance this is indicative that other components are relevant (Guerra & Thomson, 2017). Under non well mixed environment it should be expected that buoyancy term is important while it tends to be neglected for well mixed environments (Guerra & Thomson, 2017). However, to put this into

context, a stratified water column with a distinct interface is not well mixed as a whole but within the two separate portions it can be properly mixed. Based upon the way buoyancy production and consumption are described by Aupoix et al. (1990), the interpretation that can be formulated for estuaries is as follows. During flood conditions the unstable water column of dense water moving into the estuary, as captured by Figure 3, is associated with buoyant production. However, during ebb as a density interface can become clearly established over a hollow the buoyancy consumption limits the contribution TKE can have on mixing the stratified layers separated according to density properties.

The TKE balance is based upon the rate of change of total TKE which has units [m^2/s^3]. Stacey et al. (1999) provides estimates of the total TKE [m^2/s^2] based upon a four beam ADCP. However when a five beam is available, that provides and independent estimate of $\overline{w'^2}$, it is more suited to exploit its benefits so that the definition of De Serio and Mossa (2014) applies in terms of equation 13.

$$TKE = \frac{1}{2}\left(\overline{u'^2} + \overline{v'^2} + \overline{w'^2}\right) \quad (13)$$

Turbulence production rate

Guerra and Thomson (2017) indicate that the production rate of TKE, termed P [m^2/s^3], resulting from flow mean shear can be estimated from the five beam ADCP data with equation 14. Other formulations focus on only the first component (Stacey et al., 1998) or the first two (Simpson et al., 2004). In Simpson et al. (2004) the result is portrayed as P/ρ. Considering the units of the TKE as [m^2/s^2], it more logically follows to focus on formulations that omit this complementary density such that the TKE production rate has the same units as the TKE rate of change.

$$P = P1 + P2 + P3 = -\overline{u'w'}\,\frac{\delta\bar{u}}{\delta z} - \overline{v'w'}\,\frac{\delta\bar{v}}{\delta z} - \overline{w'w'}\,\frac{\delta\bar{w}}{\delta z} \quad (14)$$

The formulation of equation 14 is based upon the Reynolds stresses and vertical velocity gradient of all three components. The expression assumes that horizontal shear is small such that the vertical shear of different flow velocities along the water column dominates (Guerra & Thomson, 2017). To calculate estimates for the derivatives in this equation Guerra and Thomson (2017) use the centered gradient between subsequent depth entries of the 10 minute averaged velocity values. This gives values in between the z points sampled by the ADCP but resampling through interpolation allows to rectify this. The use of the horizontal velocity estimates derived from the inclined ADCP beams implies that the uncertainty associated with the TKE production rate increases up along the water column (Guerra & Thomson, 2017), for the case where the ADCP is positioned on the bed, because of the longer horizontal span between the positions sampled by the slanted beams.

Dissipation of turbulence

The quantities until now addressed are in a direct way derived from the along beam velocities. Instead TKE dissipation rate requires an indirect method (Guerra & Thomson, 2017) which explains why multiple alternatives are available. Two techniques that are applicable in the analysis of ADCP data are turbulent kinetic energy spectra and turbulent structure functions (Guerra & Thomson, 2017). While these methods are applicable to find an indication of persistent turbulence, more sporadic intermittent turbulence cannot be addressed (Greene et al., 2015). Further, in the study of a vertically stratified water column, the turbulent structure function method of Wiles et al. (2006) is not suited because it relies on along depth relations amongst the vertical beam velocity fluctuations w'. In a stratified water column, it cannot be expected that eddies along this vertical profile are relatable.

To derive a TKE spectrum, spectral analysis is applied on a time series segment of along beam velocity fluctuations from the vertical beam e to convert it to the frequency domain that represents how the TKE is redistributed amongst a variety of sizes of eddies (Guerra & Thomson, 2017). Accordingly, a consistent choice in the analysis of ADCP data for a TKE balance would be to use segments based upon those employed in the Reynolds decomposition. The turbulent kinetic energy spectra method exploits the Kolmogorov's hypothesis which explains that energy contained in larger eddies, that depend upon the local circumstances, are transferred down to smaller eddies that instead are similar across all turbulent flows (Guerra & Thomson, 2017). This phenomenon is referred to as the energy cascade and can be observed when representing the data in the frequency domain (Guerra & Thomson, 2017). A schematized illustration is included in Figure 10.

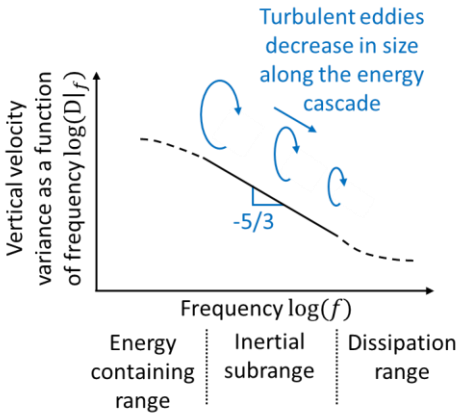

Figure 10: Schematic of the frequency domain representation of the vertical velocity variance to illustrate the energy cascade. Adapted from Seuront (2008)

The inertial subrange of the energy cascade comprises turbulent length scales for which the transfer of energy is dictated only by the dissipation part of the TKE balance (Guerra & Thomson, 2017). In the application of the TKE spectra method Guerra and Thomson (2017) use segment averaging to smoothen the periodogram, providing an estimate to the underlying spectrum that more clearly can bring out the inertial subrange. According to Guerra and Thomson (2017), for the universal scales of smaller eddies, the inertial subrange in the frequency domain is expected to follow a pattern characterized by equation 15.

$$D|_f = \alpha \varepsilon^{2/3} f^{-5/3} \left(\frac{m}{2\pi}\right)^{2/3} \quad (15)$$

In Figure 10, $D|_f$ [$m^2s^{-2}Hz^{-1}$] is the variance in vertical velocity as a function of the frequency f [Hz] (Guerra & Thomson, 2017). The constant α is equal to 0.69, while ε [m^2s^{-3}] is the TKE dissipation rate of interest (Guerra & Thomson, 2017). Under the stationary conditions the term m [m/s] is the average velocity with which the turbulence is advected past the monitored position (Guerra & Thomson, 2017). The stationary conditions should be applicable with the used segment for Reynolds averaging. However, for m to take the value of the along channel flow velocity $\overline{u_{ch}}$ it is required to employ the Taylor's frozen field hypothesis (Guerra & Thomson, 2017). This theory implies that the advection contribution from the turbulent eddies is negligible compared to the mean flow (American meteorological society, 2012). The Doppler noise can be an obstacle to observing the inertial subrange in the frequency domain (Guerra & Thomson, 2017). Indeed, in Figure 10 for the higher frequencies, the shown line levels off to a horizontal portion that, for acoustic based measurements, indicates the Doppler noise level. If the noise dominates turbulence, such that the associated vertical velocity variance is higher, this masks the inertial subrange.

3. Data collection in the study area

The data set available to the University of Twente is part of the SALTISolution program funded by the Dutch organization for scientific research termed the “Nederlandse Organisatie voor Wetenschappelijk Onderzoek”. The available CTD sensors and ADCPs were deployed over three consecutive monitoring periods, throught the winter spanning between November 2022 to March 2023, in bathymetric hollows of the Haringvliet estuary. Additionally, ADCPs from Rijkswaterstaat provide data of the conditions outside the main hollows during the temporal span of interest.

3.1. Instruments

ADCPs and CTDs from two different manufactures were involved in the overall data collection scheme. While this has insignificant influence on the CTD records, the effect on what is available from the ADCPs is important. An overview of the beam configuration differences is provided in Figure 11. Further references to beams use the alphabetic labeling convention introduced with Figure 8.

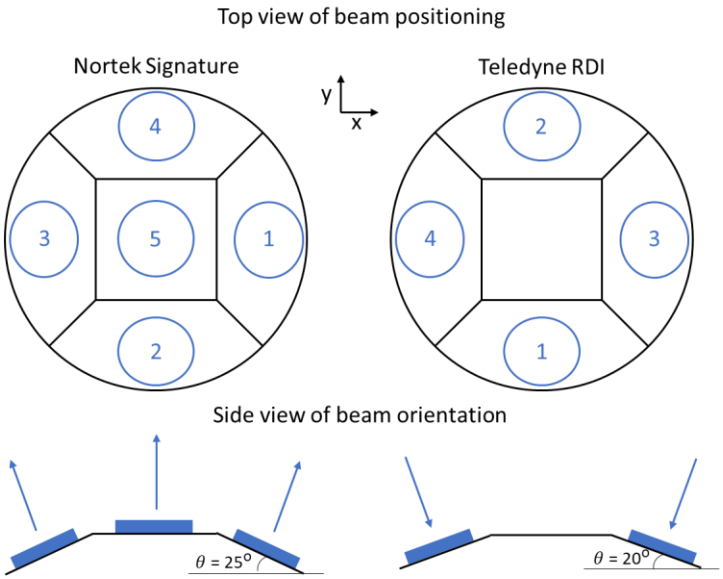

Figure 11: Schematic comparison of the beam characteristics of the two ADCP instruments interpreted respectively from Nortek (2017) and Teledyne RD Instruments (2011)

Nortek Signature ADCP

A pair of the Signature 1000 ADCPs from Nortek was used to monitor the bathymetric hollows of interest. It’s broad band encoded pulses of 1000 kHz frequency appear suitable over the narrowband option because it allows to measure weaker turbulence (Greene et al., 2015). The instrument is capable of a 16 Hz sampling rate but was, for the purpose of longer term monitoring, deployed at 4 Hz. The vertical cell size for the along beam velocities of the ADCP is 0.3 m while that applicable to the vertical echosounder is 0.05 m. Thereby, both have a blanking distance of 0.1 m which indicates the portion above the sensor over which the signal is ignored. Time series of the pressure at the instrument alongside its heading, pitch and roll are collected by the ADCP and are important to situate the ADCP in the environment it monitored. From the five ADCP beams matrices for along beam velocity, backscatter amplitude and correlation are of interest. These matrices have a row for each time entry and a column for sampled points along the water column. From the echosounder, a similarly structured matrix is available that reports the echo intensity values.

Teledyne RDI ADCP

The instruments not positioned in the hollows themselves have a 4 beam configuration. Instead of the 25 degree beam plate inclination from the horizontal used by the Signature, the RDI employes 20 degrees. Further, the positive along beam velocity direction differs between the instruments with the positive orientation being directed towards the instrument for the RDI. The blanking distance is 0.5 m while the vertical cell size of the 600 kHz RDI is 0.8 m and that of the 1200 kHz RDI is 0.5 m. The sampling frequency of both instruments is 1.25 Hz but the 1200 kHz RDI stored the data as 60s ensembles.

Conductivity Temperature Depth sensors

CTD sensors from Seabird Scientific [SBS] and RBR were used. The SBS sensors provide most of the data, with only a single RBR is involved during the first and second monitoring periods. The time series available consist of conductivity, temperature and pressure records.

3.2. Monitored locations

Based upon the georeferenced locations of the ADCPs, the bathymetric map of Figure 12 allows to give an indication of the local depth variations. Across the monitoring periods the flood gates positioned in the top left corner of Figure 12 are operated according to different management regimes, dictating the balance between the discharge to the sea and the allowed salt water intrusion into the estuary. Fresh water, that contains some background salinity, enters the Haringvliet estuary through the shown Spui but also further upstream through the Hollandsch Diep. The imaginary line connecting Middelharnis and the outflow point of the Spui indicates the limit to how far saltwater intrusion is tolerated (Rijkswaterstaat, 2023c). In terms of winds, the dominant source is around the southwest (Kranenburg et al., 2023). This, alongside the winds from the northwest, tend to be the strongest (Kranenburg et al., 2023).

The ADCP data was collected with the instruments secured in tripods that face upwards from the bed. The pair of Signature ADCPs was first deployed on the 10th of November 2022 in the bathymetric hollow that is closest to the sea and labeled as location 1 in Figure 12. After the collected data was retrieved on the 19th of December the instruments were redeployed in the same setting on the 20th. Monitoring at this first hollow ended on the 23rd of January 2023. Subsequently the ADCP pair was transferred to the more inland bathymetric hollow to collect data from the 24th of January to the 13th of March. The two hollows of interest are the same as studied by Kranenburg et al. (2023) who instead use a single centrally positioned ADCP. Of the Signature ADCPs deployed in the hollows, the instrument that is closest to the sea is further termed ADCP-1. Outside of the main hollows the RDI ADCPs collected data. The 1200 kHz RDI ADCP-4 is consistently deployed across the three monitoring periods at the downstream of most landwards hollow that is labeled as location 2. Instead, the 600 kHz RDI ADCP-3 is each time positioned upstream of the hollow from which data is collected.

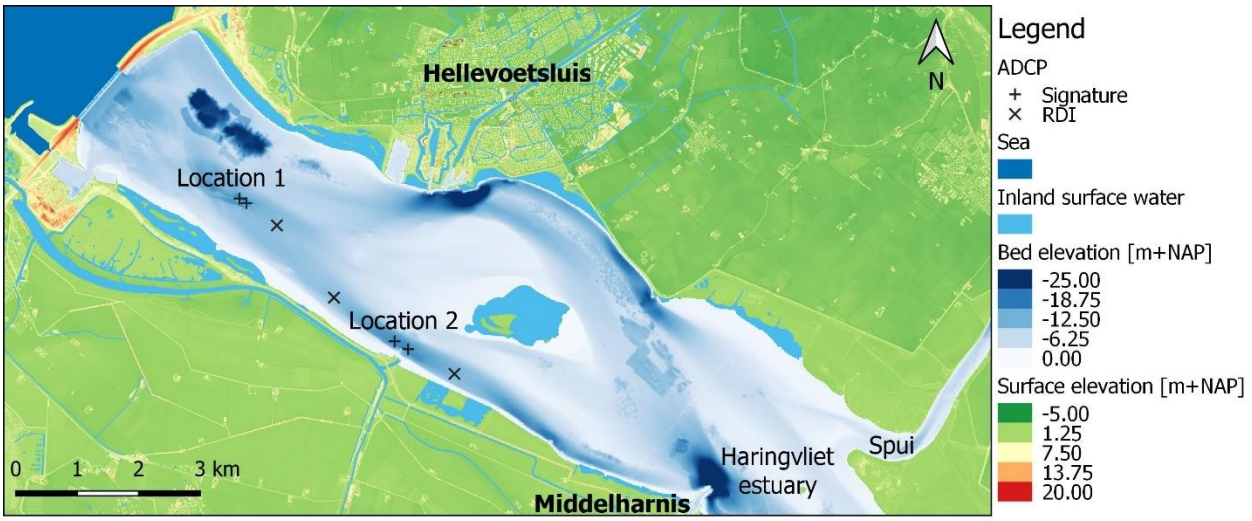

Figure 12: Positioning the ADCPs used on the bathymetry map of the Haringvliet estuary. Data layers from Rijkswaterstaat (2023a-b), Kadaster (2022) and Kadaster (2023)

Unlike the ADCPs, CTD instruments cannot provide continuous profiles of data along the water column collected over time. The CTDs were attached to lines anchored to the ground and with a buoy at the top such that their position with respect to the bed should not change more than induced by the tilting of the line along with the current direction. During the first monitoring period, a line with three instruments was positioned aligned with the main hollow direction near each ADCP but without interfering with the measurements of this acoustic instrument. The line near ADCP-1 was lost on the 5th of December such that during the second monitoring period only the one near ADCP-2 was redeployed with the upper and lower CTD attached. During the first and second monitoring period, the RBR CTD is the one at the lowest position along the line closest to ADCP-2. During the third period a single line was mounted with SBS sensors in between the Signature ADCPs. Further, at the start of each monitoring period, an along water column profile of CTD records is available near each ADCP that was obtained by letting the CTD sink from the surface to the bed.

4. Prepared data

The data files from the instruments require initial standard processing and it is necessary to situate the observations in the data collection context, offering insights to remain aware off when formulating the methods that use the prepared data to address the sub research questions. Therefore, to give an impression of what is available to work with, the prepared dataset is presented alongside the undertaken steps. An overview of the instrument positioning properties and used time periods of the available data is provided in Appendix 2.

4.1 Signature ADCP

Data extraction and quality

The data files from the Nortek ADCPs were converted using their SignatureViewer data processing software that repartitions the full temporal length of data across multiple files to allow to deal with the large digital storage capacity required for the dataset. Subsequently the continuity of the time series entries was verified. Thereby, several expected times during the first monitoring period are skipped in the series of times that indicates when records are available. Therefore, these are added and place holder entries are introduced in the corresponding time series of the quantities of interest. This issue does not apply to the other two monitoring periods.

The backscatter amplitude and correlation are useful to verify the quality of the data of the ADCP beams. For the Nortek instrument, Guerra and Thomson (2017) only use data with beam correlations exceeding 50 % and a backscatter amplitude larger than 30 dB. Accordingly, a place holder entry is used to substitute for the records in the dataset that do not meet these quality requirements. Because the largest portion of the entries of insufficient quality are situated above the water surface, the percentage of values removed is more representatively reported by considering only the water column portion that is interest as defined below in the depth alignment section. Thereby, it is in the dataset of ADCP-2 during the second monitoring period that most entries are removed with 4.85 % of the values affected while on average this is only 1.92 %.

Valid data range

The range of valid data, that spans in between the placement and retrieval of the instrument, is identified by looking at the pitch, roll and heading time series. However, because upon placement the settling can gradually continue after the most extreme initial values, often the limit time is selected based upon the echosounder data. Further, for the first monitoring period, it tends to apply that the adjacent times to the missing segments of temporal entries feature anomalies in the pitch, roll and echo. Accordingly, these portions of available records are regarded as invalid and substituted with placeholder entries.

Echo data use in calculations

Because the decibel scale is logarithmic it is unsuitable to directly use the echosounder data in processing calculations. The echosounder intensity in decibels I_{dB} can to be converted to a relative intensity value, found on the ratio between the actual intensity value I [W/m^2] and a reference intensity I_{ref} [W/m^2], according to $I_{dB} = 10 * log_{10}(I/I_{ref})$ (Gostiaux & Van Haren, 2010). However, the decibel scale remains useful for visualizations due to the more compact way to represent the large range of numbers involved.

Tilt correction

The first representative along depth positions for which the Signature ADCP reports values is at a distance above the ADCP that is equal to the summed instrument blanking distance B_i and the cell size C_i (Nortek, 2017). Both of these are vertical distances such that the slanted beams and the vertical beam can be matched conveniently to the same profile sample points. The cell size refers to how far apart the representative along depth sample points are and thus not to the extent along the water column in which the representative point is centered and its along beam velocity values estimated from.

The pitch and roll need to be considered to judge if it is required to rematch corresponding sampling depths. Estimating the difference between vertical expected instrument cell size C_i, in which the data is stored, and the actual cell size C_a, gives an indication of the importance of the pitch and roll. If significant beyond the vertical sampling resolution the bin mapping strategy proposed by Nortek (2023) allows to more appropriately align sampled water depth positions.

Figure 13 illustrates the effect of a pitch p of -10 degrees on the along water column position for which the sampled value is returned by the ADCP. For the vertical beam, any combination of pitch and roll decreases the observed cell size. Instead for the slanted beams, the beam towards which the instrument is tilted has an observed cell size lower than expected while the opposite beam has a larger one. Thereby, the slanted beam towards which the instrument is tilted experiences a larger effect on the sampled positions than the opposite beam.

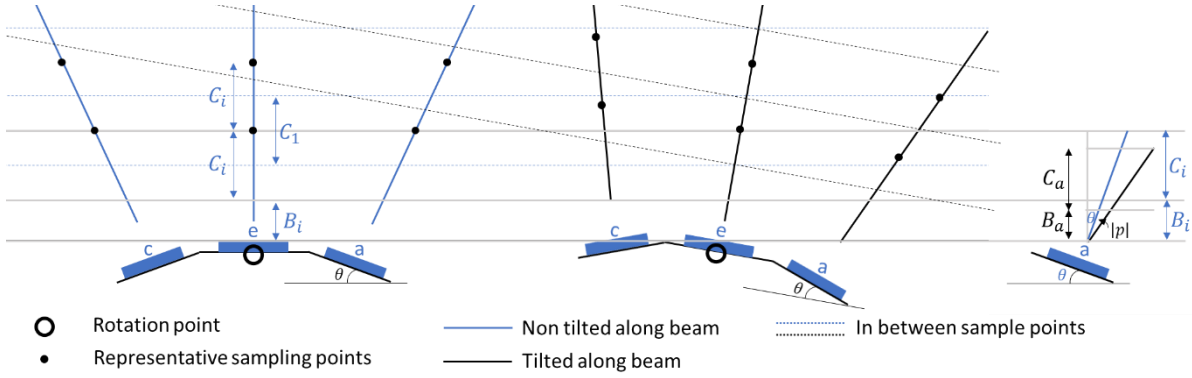

Figure 13: Schematic illustration, informed by Nortek (2017), on the effect of a -10 degree instrument pitch for the along water column position of the representative sampling points.

To determine the observed cell size, it is used that the along beam spacing of the representative sample points remains constant under the instrument tilt and is known for the slanted beams based upon the instrument vertical cell size and beam inclination angle. The blanking distance is also affected, but this change is less relevant overall because there is only one blanking region while there are many cells. In any case, the schematic at the right of Figure 13 illustrates how the combined angle of the beam slant and the instrument pitch is related to the expected cell size. This allows to write, based upon trigonometric relations, equation 17 that uses equation 16 for the adapted blanking distance B_a. This relation applies specifically for the beam on the positive side of the axis system such that if this relation were drawn up for the opposite beam a positive sign should replace the current minus included inside the cosine of the two equations. The same relation applies for roll r on the two other beams that align with the y axis.

$$B_a = \frac{B_i}{cos\,(\theta)} * cos\,(\theta - p) \qquad (16)$$

$$C_a = \frac{C_i + B_i}{cos\ (\theta)} * cos(\theta - p) - B_a \quad (17)$$

The formulations of equations 16 and 17 are based specifically for an instrument axis of interest. However, for the vertical beam, the combined action of pitch and roll needs to be considered such that the actual cell size is instead dictated by equation 19 that uses equation 18 to account for the effect of the instrument tilt on upper position of the blanking region.

$$B_a = B_i * \cos\left(\text{atan}\ (\sqrt{tan^2(p) + tan^2(r)}\right) \quad (18)$$

$$C_a = (C_i + B_i) * \cos\left(atan\ (\sqrt{tan^2(p) + tan^2(r)}\right) - B_a \quad (19)$$

With the known instrument cell size and the estimated actual value, the series of along depth positions follows and a comparison is possible. When the absolute difference between two points exceeds half the expected instrument cell size this implies that the observed representative sample point is closer to the neighboring expected data point. Accordingly it is more representative of that position. For any beam where the vertical cell size is decreased by the instrument tilt the entry is removed such that the higher up data point is shifted one position downwards to replace the one omitted. If the actual cell size exceeds the expected a place holder entry is incorporated such that the data point, for which a larger than half the cell size difference between the observed and expected series is found, is shifted upwards. Linear interpolation is used to fill the created voids along the profile. It is important to adjust the positioning of the observed data points above the first cell from the bottom where the allowed difference between the observed and expected position is exceeded because it prevents larger differences to accumulate.

While through the monitoring time, the heading of the instrument remains around a clearly identifiable mean, that of the pitch and roll is not so stationary. Continued instrument settling affects a large extent of the data. Therefore, to correct for the instrument tilt, a moving average spanning a day of data is used to obtain a smoothened time series of the pitch and roll that facilitates an assessment that varies over time. Overall, the instruments were well leveled during placement such that the influence of pitch and roll is minor. The instrument deployment is best during the first monitoring period such that only a single cell shift is necessary based upon the roll of ADCP-2 when considering the water column portion of interest as identified during the depth alignment described in the next section. During the other two monitoring periods, a 1 cell correction is at least necessary over some portions of the data records. However, the pitch of ADCP-2 during the second monitoring period is the largest amongst the inclinations observed. Indeed, beam c needs to have up to 3 cells removed along the water column while two void cells are incorporated into the profiles of beam a. This to compensate for a pitch that has a time averaged value of 5.32 degrees that also causes 2 cells to be removed from the observed echosounder profile such that those remaining appropriately fit to the expected sampling points for a horizontally placed instrument.

Depth alignment

The differences in depth between ADCPs in a pair need to be known to make their observations comparable. The high vertical resolution of the echosounder data is helpful to determine the depth monitored by each ADCP due to the high peak in its profile that results from the strong density transition between the surface water and the air above. The relative echo intensity dataset is smoothened and reduced in size by finding the 10 minute averages at 10 minute intervals. This allows the remaining data to be contained in a single file from which the time series of peak echo value positions is retrieved. The

depth range over which the maximum is calculated is the upper two thirds of the stored cells to avoid the influence of high echo backscatter values observed close to the instrument.

The obtained surface level time series is surprisingly smooth and does not feature any outliers that deviate from the systematically undulating pattern. The oscillation period of 12.4 hours, retrieved by consulting the time series transformed to the frequency domain in a periodogram, suggests that there are two moments with a peak surface water level in a day. This regardless of the flood gate operation regime. Further, computing the correlation coefficient between the time series of the ADCPs in a pair returns the high values of 0.97, 0.99 and 0.97 across the three monitoring periods. Shifting the time series of ADCP-1 with respect to that of ADCP-2 does not improve the correlation.

Taking the average of each surface level index time series and comparing the value within each ADCP pair allows to state that the instruments are at the same depth during the first monitoring period. During the second, ADCP-2 has on average two index positions more in the profile, up to the water surface, than ADCP-1. This suggests that it is positioned 0.10 m below ADCP-1. Therefore, no depth alignment is necessary for the non echosounder data because the observed difference is smaller than the vertical sampling cell size of 0.3 m. However, for the most landward hollow, ADCP-2 is placed 0.45 m higher than ADCP-1.

The lowest ADCP of each pair is used as a reference and time series of place holder entries are used to complete the matrix of the higher up positioned ADCP. To omit the influence from the surface on the data Kranenburg et al. (2023) recommend to remove 1-1.5 m below the identified surface level. Based upon excluding surface level influences, a water column of 15.1 m is kept for location 1 and one of 14.5 m for location 2. For these water depths the largest slanted beam separations are respectively 12.8 m and 12.3 m. Because the length of the bathymetric feature amply exceeds these values there should, according to Stacey et al. (1999), be sufficient homogeneity in the flow to derive metrics from a pair of slanted beams.

Reynolds decomposition

To practically apply Reynolds decomposition to the along beam velocities, the approach of Stacey et al. (1999) is followed. Thereby, for each beam, $\bar{b}$ and $\overline{b'^2}$ are estimated with the population mean and variance calculated with 10 minute intervals for the times centered at the corresponding 10 minute windows within which the statistics are assumed stationary. Such an assumption can be verified with a run and reversal test on the series of the 30 second based mean and variance of along beam velocities (Stacey et al., 1999). This is feasible considering that the sampling of the instrument stores a value every 0.25 second. The estimators have two types of error incorporated, namely bias and spread (Stacey et al., 1999). The latter random component can be reduced by having more frequent observations in the period taken to average over. This would have been possible were the sampling frequency of the instrument increased which is not worthwhile at the expense of the associated increased rate of battery drainage.

The testing for stationarity involves counting the number of times that the median value of the 10 minute window is crossed in the series of the 30 seconds spaced mean and variance values that allow to apply the test to both statistics. If the count deviates sufficiently from that expected for a randomly generated series, then the null hypothesis supporting the presence of randomness can be rejected in favor of the alternative hypothesis. Therefore, according to the nature of statistical testing focus is upon demonstrating with a certain significance level that there is a systematic pattern present instead of seeking to prove that there is none. Therefore, to not dwell on this testing procedure, it is just further stated that the approach

and statistics are implemented as described in Davis (2002, pp. 185-187) for this run and reversal statistical test type recommended by Stacey et al. (1999). The strategy is applied on all 10 minute windows present along the water column in 5 randomly selected 8 hour periods from the dataset. From these no rejection of the null hypothesis applies at the 95% confidence level. Thereby, only allowing to state that there is not sufficient evidence that the observed pattern deviates from randomness. Therefore, the use of the stationary assumption is not opposed but also not confirmed.

Mean and variance validity

The condensed dataset featuring mean and variance values at 10 minute intervals is revised to exclude any windows that contain less than 800 valid entries from the expected 2400 data points that should be available to calculate the estimators. The amount of removed data points is however minor being 3.7% for the beam with most omitted entries following the data quality verification. Accordingly, it is demonstrated that the invalid entries removed for quality reasons tend to be clustered.

The created open voids are filled by first linearly interpolating to the missing positions along each row and column separately. Then, for each cell the weighted average of the two estimated values is used where $1/3^{rd}$ of the weight is given to the along time interpolation and $2/3^{rd}$ to the along depth. This choice follows from how Kranenbrug et al. (2023) report that their smoothing strategy the uses of seven 10 minute points in time and three 0.5 m cells in space, indicating that the along space probably gives more information about a local point than the along time with the set up used. The missing data profiles present during the first monitoring period are not interpolated.

The choice of the threshold of 800 entries is based upon the number required to reproduce the normal distribution that is not proven to be significantly different from that based upon the mean and variance statistics from the complete 10 minute window during which the statistics are stationary. Two randomly selected 8 hour periods are used and from each five hundred random 10 minute segments drawn. For the segments with 2400 entries, the normal distribution is fitted. Subsequently, values are randomly removed from the segment and each time a new normal distribution is derived from the result. As long as this newly fitted distribution is not proven by a chi squared test to be statistically different from the original with 95% confidence, the process of removing entries is continued. The comparison between the two distributions is set up according to the procedure described in Robinson (2014, pp. 142-147). When the null hypothesis, that states that the approximated distribution is equivalent to the original distribution, is rejected, the number of remaining entries is taken note off because this is an indication of the minimum number of values for which the fit is proven to be wrong. Therefore, when not rejecting this just implies that based upon the series there is not sufficient evidence that the two distributions are different. In that context the values in the series are deemed better representative of the monitored conditions than an interpolation based upon the surrounding 10 minute segments. The process is also repeated by replacing the random entry removal with a systematic one. The first is initiated at the segment start while the second from end.

Three series with the number of values that can be removed from each segment are obtained. From these, empirical distributions are estimated. The two types of systematic removals yield similar distributions and are more conservative in indicating the minimum required entry number than the random approach. Accordingly it is found that 95% of the tested segments allow to remove more than 1600 records prior to the chi squared test showing that the distributions are not possible to be statistically similar anymore.

Heading alignment

Using the 10 minute averaged velocities from the Reynolds decomposition, the horizontal velocity components are calculated using equations 5 and 6 presented in Section 2.5. The result is in instrument coordinates, but the heading of the ADCP allows to relate the value amongst the instruments. However, a common axis system should first be defined. It is useful to have one based upon the local main channel direction where the majority of the velocity vectors are clustered along. This coincides with the maximum velocity variance orientation (Kranenburg et al., 2023).

Principal component analysis [PCA] is used to retrieve the orientation that explains the dominant portion of the variations in the dataset of horizontal velocities available for each ADCP for the respective monitoring periods. The input variables for the PCA, performed using the dedicated MATLAB function, are the two velocity components along the instrument axes. The observations are taken as regrouped over the valid time and water column portion of interest. As such the two data matrices take the restructured form of to two column vectors that are used as input for the PCA.

With the pair of variables as input, two principal components should be returned that are orthogonal to each other. A strong agreement between ADCPs is found. Despite the lower variance explained during the first monitoring period, the averaged orientation of the principal component is equal to that for the second monitoring period for which the variance explained is 96%. At location 2 the principal components from the ADCPs differ up to just 1.2 degrees from the value characteristic for location 1 such that it is relevant to use a common along channel positive x axis pointing 303.5 degrees clockwise with respect to north. Thereby positive velocities are directed towards the sea. Similar to the configuration of the instrument coordinate system, the y axis direction is taken 90 degrees counterclockwise of the x.

The resultant velocity vectors in the new axis system are found by adjusting their orientation such that they are relative to the new x direction by considering the difference between the chosen along channel and the instrument heading. Using the newly identified common axis, the adjusted resultant vector of each velocity is projected upon it to obtain the corresponding u_{ch} and v_{ch}.

4.2 RDI ADCP

Data extraction and quality

The software from Teledyne to extract the binary data files retrieved from the instruments was not accessible for use. Therefore, the conversion of the files relies on the readADCP function in the rdi path of the MATLAB script of Vermeulen (2023). While originally both instruments have the same sampling, ADCP-3 stores the data with a 0.8 second interval while ADCP-4 instead does so based upon a processed ensemble of 60 seconds. The application of the script of Vermeulen (2023) allows to completely extract the data of ADCP-4 while only the first 20 minutes of each hour of possible entries for ADCP-3. Thereby it is unclear if the original binary file contained the remaining two thirds of potential data. Only entries for which the correlation exceeds 64 % and the backscatter amplitude is above 50 db are further used according to the minimums indicated by Bender and DiMarco (2009). The highest percentage of along beam data removed for a monitoring period is 1.45 % for ADCP-3 while it is 0.96% for ADCP-4.

Valid data range and tilt correction

For each ADCP deployment, the valid time range is identified by starting at the latest time that either the pitch, roll or heading stabilizes and ending as these values are strongly disturbed again. Because over the data collection period no anomalies in these metrics occur, also no further sections are removed. The pitch and roll remain over the portion of interest well represented by the average value and therefore allow to determine a single representative observed cell size for each beam per deployment. This is done in the same way as for the Signature instrument because the vertical sampling point positioning up from the ADCP identically applies to the RDI instrument for which it is further indicated by Teledyne RD Instruments (2011) that the along water column portion used to estimate the representative sample point value takes a range that is twice the vertical resolution cell size and surrounds the sample point. Considering the water column portion that omits the abnormal along beam velocities near the water surface, the number of expected instrument and actually observed cells is compared and allows to conclude that a correction for the pitch and roll is not necessary.

Along channel alignment

The along beam velocities are 10 minute averaged and for the ADCP-3 a linear interpolation is applied over time to fill the 4 missing entries in each hour. As for the Signature data, PCA allows to determine the dominant flow direction. Considering the deviations that arise relative to the more constant principal flow component indicated by the Signature ADCPs it is chosen to use separate along channel directions for each deployment position. Indeed, the local bathymetry differences can slightly alter the direction of the main current that passes through the observation points.

Considering that ADCP-3 is intended to be deployed at the same position during the first two monitoring periods while ADCP-4 across all three, it is chosen to use an average of the flow orientations that characterize most variance during each monitoring period to obtain the general value per deployment location. Accordingly, the main flow orientation derived from ADCP-3 during the third monitoring period at the location only monitored on this occasion is directly used. All variances explained for the main principal component exceed 94% except that of ADCP-3 during the first monitoring period that is only 69%. Nevertheless, the orientation of this principal component is only 2 degrees from that observed during the second monitoring period at the same location. Looking at the horizontal velocities, the difference in variance explained follows from that the first monitoring period has much lower flow velocities with more unclear directionality than observed under the stronger along channel currents present during the second monitoring period. For ADCP-4, of which the data is only of interest during the third monitoring period, the average orientation from all three periods perfectly coincides to the degree with the value for the period of interest. Upon implementing the realignment of the horizontal velocity components with the identified along and across channel directions, this processed dataset is matched to the closest corresponding 10 minute averaged times of the Signature data.

4.3 CTD time series and profiles

Data extraction and quality

To process the instrument files from SBS, their Fathom software is used. Similarly, RBR have their Ruskin package. Either product allows to retrieve the time series of conductivity, temperature and pressure. These are further processed with the UNESCO based method presented in Appendix 3 to retrieve salinity and ultimately density estimates. For the CTD profiles collected at the start of each monitoring period, the

portion in between the time that the lowering of the instrument is initiated up to where it reaches the bottom before being pulled up again is identified. This is done by considering the portion over which the pressure observed by the instrument increases. For the CTD time series along the monitoring periods, it is verified if none of the expected temporal entries are skipped in the files while attention is given to extreme values. Within the temporal range of valid data, that is not affected by the placing and retrieval of the instrument, no anomalies are present. Based upon the variety of data sampling rates with which the instrument data is stored, the time series of 10 minute averages are derived to allow comparability with the ADCP data.

CTD profiles depth series estimated from density and pressure

For a CTD falling down through the water column the pressure and density are known over the short segment of time that it takes for it to travel down the water column. The first record is close to the surface and therefore its depth is estimated by directly applying equation 20. This formulation incorporates the depth D [m], pressure P [dbar] and density ρ [kg/m^3]. Subsequently the increase in pressure and density allows to identify the depth increase for each data point such that a depth position series replaces the time series of observations. The physical quantities of interest are interpolated to a depth series with constant increment and the depth averages are retrieved per profile.

$$D = \frac{10000P}{\rho g} \tag{20}$$

The times at which the CTD profiles are collected around the start of each deployment period can reasonably be associated to the first found valid time point from the 10 minute averaged Signature data. Indeed, for the first monitoring period, ADCP-1 and ADCP-2 have a valid processed observation that is, to the nearest 5 minutes, separated by 20 and 15 minutes relative to the earlier taken corresponding CTD profiles. During the second deployment this time difference is 10 minutes for both sampled locations while it is only 5 minutes for the profiles collected at the start of the third period. Considering that there is an unavoidable temporal lag, these values seem acceptable to compare ADCP data with CTD profiles.

Associating the depth averaged density obtained from each CTD profile with that of the closest corresponding Signature ADCP pressure record, a depth estimate can be made for each position. This gives a second insight into the depth differences between the ADCPs. The findings are comparable to the long term based estimation from the comparison of the surface level detected by the echosounder. For periods 1 and 2 the correspondence is nearly equally close with the values of 0.08 and 0.19 m being within the range of the 0 and 0.1 m estimated based upon the echo delineated surface. For period 3 the match is perfect with the 0.44 m to 0.45 m connection. Accordingly, the depth alignment strategy to make the two ADCPs comparable is confirmed. Further, knowing the depth position of the ADCP allows to use the along depth series of salinity, density and temperature to find the values of these metrics at the positions along the water column sampled by the ADCP echosounder.

Position of the CTDs collecting time series relative to the Signature ADCP position

Because the depth of the CTD instruments collecting time series varies with the surface water level it is desirable to relate their along water column position to those of the ADCPs. The approach used for the CTD profiles employs the information of the density along the water column. However, the first valid found times from the CTDs reporting a time series throughout the monitoring period is not sufficiently close, extending beyond the hour, to be associated with the CTD profiles. Therefore, a differ approach is used.

Under the absence of accumulated salt water in the hollow, the pressure is expected to linearly increase downwards along the water column and accordingly induce a corresponding density increase. This observation is confirmed, and further elaborated upon in Section 6.1, by four of the processed CTD profiles available near the Signature ADCPs under conditions that there is no salt in the hollows. Therefore, because at least two CTD's are attached to a line, a least squares linear regression can be fitted to the observed densities. This requires that an average density value is used as an initialization to calculate an approximation of the depths of the CTDs and the Signature ADCP based upon the observed pressure value using equation 20. With the depth values, the down to the bed linearly increasing density regression fit allows to find above each position of interest a more representative depth average density value. With each of these, the depth value of the instruments is recomputed. This process is repeated until the value stabilizes to give the final estimated depths of the CTD and Signature instruments.

To not base the position of the CTDs above the Signature ADCP upon a single profile, two sets spanning 8 hours of the 10 minute spaced series, selected at times that the CTDs show that there is no accumulated salt water, are used for each deployed ADCP per monitoring period. There is a strong consistency in how far the CTDs are found to be above ADCPs, with values rounded to decimeters being equal. Accordingly a transect based representation of the monitored site is provided in Figure 14. This plot is produced by positioning the ADCPs at the level of the bathymetry dictated depth with respect to NAP and the CTDs at the determined distance above these positions. Alphabetical labeling is used for the CTDs, with CTD-a and CTD-c employed to destinate the lowest and highest instrument along a line. CTD-b is involved if there is a third ADCP. For location 1 no specific different distinction is made between the first and second monitoring period because the distance of the CTD-a and CTD-c above ADCP-2 is the same in the unit of decimeters.

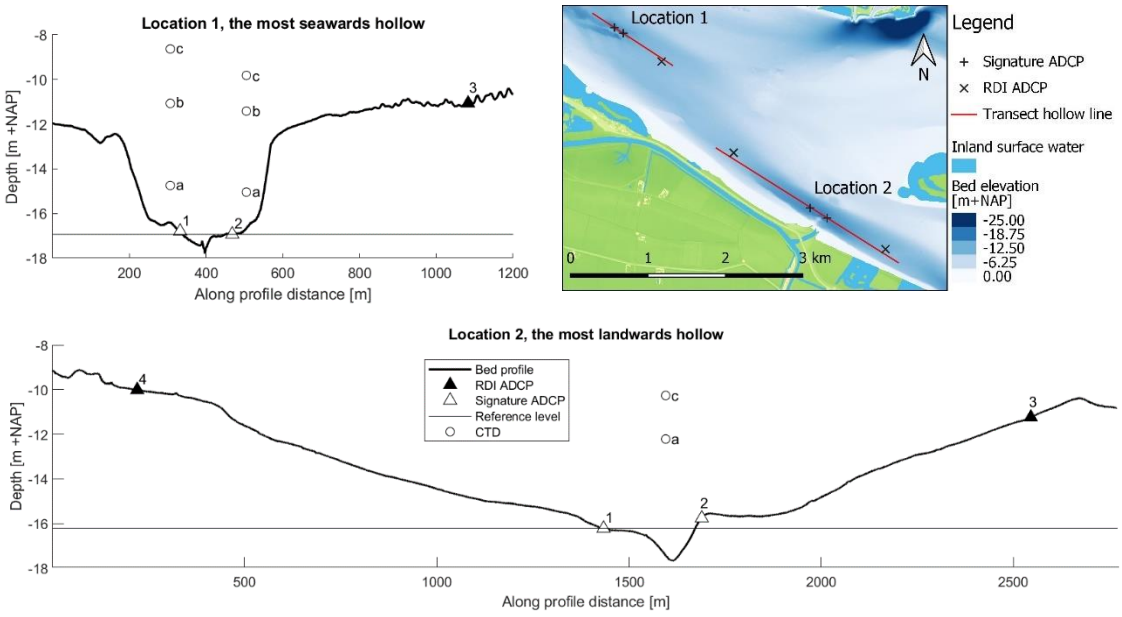

Figure 14: Position of the monitoring instruments shown on the along channel transects of the two hollows that is based upon the bathymetry of Rijkswaterstaat (2023a-b).

5. Method

Details on the approaches used in the process to understand the flow dynamics associated with the flushing of accumulated salt water from hollows are presented per set sub research question. The techniques that tend to be used to understand ADCP data as described in Section 2.5 are directly applicable to the prepared data. Therefore, attention is principally upon indicating to what purpose the strategies are employed while giving details upon less standardized supporting processes used.

5.1. The interrelation between the density stratification and flow conditions

With the target to obtain an overview perspective of the data, the most direct flow characterizing parameters of velocity and TKE are used to identify how the flushing events fit into the overall time series. Focusing first upon the effect of the salt water on the flow itself allows to subsequently consider how the incoming current can lower an established vertical stratification.

Interface delineation

To identify the position of the density interface, focus should be on the echosounder data and the along channel velocity profiles. The first offers a direct insight into density transitions while the second is the velocity component that is expected to show the strongest response to the presence of the interface because it explains most of the variance in the dataset. Despite that the study of the echosounder data for the water surface interface definition is based upon the clear peak that the water to air transition induces, no consistently prominent secondary peak pertaining to the density interface can be observed. While this is further explained in Section 6.1, it follows that the density interface delineation uses the along channel velocity profiles. The applied approach relies on visual confirmation of the interface position with an element of automatic selection. This allows its application over the full monitored extend with control over which velocity profiles actually show a response to the presence of the interface.

A smoothed version of the along channel velocity data from the Signature ADCPs is obtained by using a moving average with six points in time and three in space which is similar to that reported by Kranenburg et al. (2023) for the Haringvliet conditions. The density interface position is sought to be derived from the point of maximum along channel velocity profile gradient. That gradient value is obtained using a central point estimate in between the by the instrument reported representative sampled depths. Lineally interpolating this profile gives the estimates of the gradient at the original positions.

In the semi automatic interface delineation, an initialization plot is produced that contains a fixed along depth position axis while the second axis is set to reflect various quantities on a normalized scale. The first element incorporated on this axis is the time that contains the velocity profiles with nine 10 minute instances on either side of the position assessed. Subsequently, it is used to plot the velocity profile of the instance assessed as well as its gradient profile. When an interface is present the maximum gradient position is expected to yield the position of interest. However, the used set up allows to assess this per case and possibly select a different point that better appears to characterize the position of the interface when the along water column dynamics are more complex. Alternatively when there is no salt water accumulated, or no clear interface related response shows up in the velocity profile, a dedicated value is used to indicate the absence of a perceivable interface.

With the interface position initialized, attention is turned to the next time instance. The correlation between the previous velocity profile and the new one is assessed. If it exceeds 0.95%, the interface

position value is deemed unchanged. Alternatively, a position lag is introduced to identify if this shift produces the desired correlation. If so, the interface position is taken according to the shift, and the correlation of the next entry is verified. When the correlation criterion is not met, a new manual input is necessary to confirm that the peak velocity profile gradient indicates the interface. In the plot used for this purpose the velocity profile line from the previous visual selection and the latest with sufficient correlation are included in addition to the components of the initialization plot used. This allows to reflect upon the appropriateness of the used approach.

The produced interface position time series is visually checked by overlaying it on the complete dataset of along channel velocity profiles. Any abrupt changes are removed that are considered outliers from the overall interface variations. To address the times when there is an absence of a perceivable interface, a cubic interpolation strategy is used to estimate the interface position based upon those identified. The result is smoothed using a six point moving average and each value is subsequently rounded to correspond with the positions expected to be sampled by the ADCP. Further for the times when there is no accumulated salt water, it is ensured that the interface position reflects this. From the overall time series of the interface position, the occasions of major interface lowering are identified and taken as the main flushing events of interest.

Depth averaged flow characteristics

Because the datasets retrieved from ADCPs are multivariate with both a temporal and spatial dimension, it is relevant to first focus upon the dominant patterns to obtain an understanding of the underlying structure that exists within the dataset. Depth averaging draws attention to the changing conditions with time. To acknowledge the difference in conditions below and above an interface, averaging is done separately on either side when there is a prevalent density stratification. Thereby the 5 cells centered at the delineated interface are not considered to avoid the influence of the transition affecting the average because the interfacial processes are considered in Section 5.2 and 5.3.

The flow parameters to which depth averaging is applied are the resultant horizontal velocity orientation and magnitude for all ADCPs alongside the vertical velocity and the TKE specifically for the five beam Signature instruments. To estimate the turbulence characterizing TKE with equation 13, the normal Reynolds covariances are calculated with equations 8 to 10. No negative values are expected but are possible from the formulation of the equations for $\overline{u'u'}$and $\overline{v'v'}$ that features a factor of -1.64 that is multiplied with $\overline{b_e'^2}$ in the addition with the along beam variances of the pair of slanted beams for an instrument axis orientation. Any obtained negatives are substituted with a placeholding entry.

While the spatial averaging offers and an overview perspective, it remains relevant to be aware of how well the depth average characterizes the vertical profiles of the parameters. Therefore, the standard deviations along the water column are computed in association to the mean. Further, removing the mean from the original dataset gives insight into the spatial distribution of the remaining variations.

To compare the depth averaged time series in amongst the Signature ADCPs, for the overflowing as well as the below interface conditions, and relative to the data from the RDI ADCPs, the differences arising over time can be considered while the correlation coefficient is insightful as a general measure of covariation. Further, attention is on the how the conditions at times of major interface lowering compare to the rest of the data when the interface is developing, stable or not existing. Indeed, the time series are useful to identify the flow conditions at the hollow that can be associated to the lowering of the interface.

5.2. Density interface evolution during flushing events

To understand how the observed incoming and interface overflowing currents induce flushing at the two hollows, the processes at the interface during the times of main interface lowering are studied. Attention is specifically upon the in Section 2.2 reported process of interface tilting and turbulent entrainment while the large scales involved invite to give specific attention to along water column patterns in flow velocity.

Higher resolution delineated interface position comparison

Over the sections with identified prolonged interface lowering, the interface is delineated again but with more manual input by using a correlation threshold of 0.99. The main target is to reduce any interpolation necessary alongside limiting the length of the portions over which the delineated interface can take a single value by just featuring correlated profile shapes. The difference between the interface positions delineated for both Signature ADCPs indicates if the interface tilts. Such observations can be put in context by a direct comparison between the velocity profiles. The specific profiles of horizontal velocity orientation and magnitude are relevant to understand the situation that goes paired with the lowering of the interface. The ratio of the along channel to lateral component prevalence is also considered.

Interaction of shear Reynolds covariance with the gradient of the horizontal velocity profiles

To reflect the influence that the horizontal velocities have on the interface, the TKE is considered. Indeed, the maximum and minimum TKE within the 5 cells centered around the interface provide an indication of the importance of turbulent entrainment from the interface by reflecting what prevails from production and damping. To better understand the role of the interface in the observed turbulence the TKE production rate is calculated according to equation 14, giving specific attention of the contribution of each of the three components. The shear Reynolds covariances are found according to equations 11 and 12 while the velocity gradients for each instrument axis are computed with the same approach used when obtaining this metric from the along channel velocities for the interface delineation described in Section 5.1.

5.3. The stability of the density interface

From the presence of turbulence and its production, attention is further turned to the stability of the interface. This is approached by studying the balance between the buoyant damping and interfacial shear with the Richardson number. Further attention is specifically on the oscillating periodicity of interface instabilities through the use of the high resolution echosounder data.

Gradient Richardson number estimate

Because of the absence of a continuous time series of density profiles the estimation of the density gradient along the water column hampers the direct use of the gradient Richardson number equation 2. Therefore, it is chosen to apply the definition of the shear Richardson number presented in equation 5. In its application, the velocity profiles are used to estimate the shear layer thickness around the interface.

In applying equation 5 the mean and variance of the along channel velocity profile portions on either side of the interface are used to retrieve R_s. Thereby, the above and below depth averaged time series allows to identify c directly by calculating the velocity difference. The standard deviation over depth below and above the interface is further employed in the derivation of i. This is done by finding the two depth positions for which the along channel velocity is observed that is once the value of the standard deviation closer to the interface than the depth average velocity value of the above and below interface layers respectively. The range between these two positions is used as an estimate of i. If the velocities in the

layer above and below the interface, over which the average and variance are calculation, would be normally distributed it would follow that 84% of the velocity values are on the side away from the interfacial layer. The calculation of R_s is only possible when the bounds of the interfacial layer remain in between the CTDs that collect the time series employed to retrieve r. Indeed, the density values should be representative of those prevalent in the layers around the interfacial one.

Sensitivity of the Richardson number estimate

Because of the unknown uncertainty associated to the values used as input for the three variables present in the equation for R_s, it is useful to consider three bivariate sensitivity analyses on the rate of change of R_s relative to each of the individual inputs. Indeed, differentiating R_s with respect to r and i allows to obtain two expressions in terms of the two other variables not differentiated to. However, because all three variables remain in $\delta R_s/\delta c$, the use of the $(1-r)i$ integrally as the second variable next to c appears suitable because the influence of r and i is already separately considered in combination with c within the other two scenarios. The range of values considered as input for the variables is chosen from those actually observed during the calculation of the Richardson number.

Alternative to the Richardson number estimate

To obtain a second, more temporally complete, time series of the Richardson number a second approach is also applied. This consists of calculating the gradient Richardson number as presented in equation 2 but taking in S only the along channel velocity component. For this, the temporarily varying u_{ch} profile gradient value at the delineated interface is used. However, such data is unavailable for the density gradient required for N. Therefore, a solution is to use a fixed density gradient value derived from CTD profiles. Kranenburg et al. (2023) confidently apply this at the Haringvliet to calculate the Richardson number over a time frame of 50 days during which the interface present in a vertically stratified hollow is gradually lowered as the salt water is flushed. Their choice is partly justifiable because repeated CTD profiles confirm the constant nature of the density gradient. However, with the present dataset only single CTD profiles are available at the start of each monitoring period. Therefore, this alternative method to find the Richardson number is only applied to those of the monitoring periods that start with a hollow where there is accumulated salt.

Using the frequency spectrum to recognize oscillating interface instabilities

The high vertical resolution of the echosounder data lends itself to try to identify cyclic patterns in interfacial instabilities. However, a prerequisite is that the interface position is detected by the echosounder. The dataset, separated in bands with an 8 hour span, is used to plot time series of profiles using the decibel scale with the 0.25 second sampling resolution. For the 8 hours during which an interface is visible, the band of along depth cells in which it is contained is recorded alongside with the cell at which the maximum echosounder value occurs in this band.

The used strategy is employed to reduce reliance on the time series of maximum echo intensity positions along the water column in the interface region. Indeed, as observed when using the echo data to delineate the clearly identifiable water surface interface, the along water column variability tends to be high such that a maximum echo position time series is itself not insightful over prolonged periods. Therefore, to focusing upon the portions where the maximum echosounder value time series does not fluctuate to the extent of not clearly supporting the position of the interface, approximated by using a 10 minute moving

average that contains 2400 data points, segments are extracted for which the smoothened interface position stays within a cell. For the segments containing more than 2400 points in time, the series at the interface is used in a spectral analysis.

To focus the periodogram on the cyclicity of interest, the time series is averaged to produce one with an interval that is smaller than the Buoyant frequency but is of its order of magnitude. Further, outliers are dealt with by omitting those values that deviate more than three standard deviations from the mean. The periodogram is estimated by applying the MATLAB Fast Fourier Transform to each time series of which the mean is removed and to which a taper applied. The cosine tapered window used affects 1/8 of the segment length at either extremity and should reduce spectral leakage caused by the series having a finite length. With the aim to identify peaks, the resulting periodogram is smoothed using bin averaging with a three point filter were 50 % of the weight is allocated to the central bin and 25 % to each of the respective adjacent ones.

To account for the possibility that the cyclic pattern is more prominently visible at the position above or below the estimated interface, the periodograms for the time series from these specific depths are also produced. When a clear peak in the spectrum can be identified, its value is recorded alongside the cell position and time range of the segment. The percentage of variance explained by the peak can be found by considering the area enclosed under the frequency bins that span its width.

5.4. Balance in turbulent kinetic energy

Next to the calculated TKE and TKE production rate, the ADCP data gives the opportunity to retrieve the TKE dissipation rate. For this, it is necessary to resort back to the original, non Reynolds averaged data of vertical along beam velocities and consult the TKE spectrum. If the TKE dissipation rate can be found, these could be compared to the TKE production rate and put in perspective of the rate of change of TKE.

Producing the spectra of the vertical velocities

For a depth position, the temporal data fragments upon which spectral analysis is applied are those used for the Reynolds decomposition but complemented on each end with half of the data from the adjacent 10 minute extents. The input series to the Fourier transform, that converts the time domain to the frequency domain, needs to be continuous. With the prospect of calculating the periodogram, values for missing entries, arising due to an insufficient along beam correlation and backscatter amplitude, are randomly drawn from the normal distribution associated with the statistical properties of the input series. This approach is chosen because the induced randomness will not result in a pattern in the periodogram while potentially attenuating one that would have been there if all data entries were available.

The periodogram is smoothed using segment averaging. This approach calculates multiple periodograms for shorter segments within the temporal range of interest to subsequently find the resulting mean. Segments are taken conform to Welsch's overlap method that allows the segments to overlap by half of their length. To balance both the length of the segments with the degree of TKE spectrum smoothing, it is chosen to use eleven 200 second segments over the 20 minute input series. As with the spectral analysis applied to the echosounder data, for each segment the mean is removed and the cosine taper used before applying the MATLAB Fast Fourier Transform.

Retrieving the dissipation rate

To solve for the TKE dissipation rate, when the inertial subrange is perceivable from the TKE spectrum, the logarithm is taken of both axis of the periodogram produced. Also taking the logarithm of equation 15 allows to rewrite it to the linear relation shown in equation 21 . This connects the dependent variable $\log_{10}(D|_f)$ of the vertical axis to the independent variable of $\log_{10}(f)$ through a -5/3 gradient. Considering the vertical axis intercept of $\log_{10}(D|_1)$ at $\log_{10}(f) = 0$ of the transformed periodogram allows to solve for the dissipation rate as shown in equation 22 when the along channel velocity is used for m.

$$\log_{10}(D|_f) = -\frac{5}{3}\log_{10}(f) + \log_{10}\left(\alpha\varepsilon^{\frac{2}{3}}\left(\frac{m}{2\pi}\right)^{\frac{2}{3}}\right) \tag{21}$$

$$\varepsilon = \frac{10^{\frac{3\log_{10}(D|_1)}{2}}}{\alpha^{3/2}\left(\frac{m}{2\pi}\right)} \tag{22}$$

To retrieve the vertical axis intercept it is required to fit a line with the -5/3 slope to the inertial subrange when it is present. In principle, it is necessary to identify over what frequency range the -5/3 slope applies and only over this portion apply a least squares regression fit to retrieve the most suited $\log_{10}(D|_1)$ value that is associated to the inertial subrange characterizing gradient. However, it is instead chosen to calculate the coefficient of determination for lines with a range of $\log_{10}(D|_1)$ inputs that are 0.1 units apart across a range of realistic values. The vertical axis intercept associated to the highest coefficient of determination can subsequently be selected. While this is first done using the full length of frequency bins in the periodogram, it is subsequently repeated but each time with a shorter subset obtained from removing the lower end of the frequencies. Accordingly, a series of coefficients of determination is produced that each have an associated $\log_{10}(D|_1)$. The final vertical axis intercept is selected based upon the highest coefficient of determination.

While the proposed search strategy could appear somewhat abstract, it is closely linked to the expected shape of the TKE spectrum as presented in Figure 10. The coefficient of determination is one minus the ratio of the sum of the squared residual from the fitted line to those from the mean. Therefore, with the longest subsets, the denominator portion of the ratio is large, producing the lower coefficients of determination. As the subset is shorted and starts to exclude the portion of the spectrum in the energy containing range, the fit of a line with the -5/3 slope is improved such that the numerator of the ratio decreases. This can induce higher coefficients of determination while the effect of the decreasing $\log_{10}(D|_f)$ range on reducing the deviations from the mean is limited. Indeed once the frequency subsets become so short they come to the end of the inertial sub range portion and focus on the more horizontal noise related part of the periodogram, the coefficient of determination theoretically should have the tendency to decreases again because the residuals from the mean are lower such that the mean provides an as good estimation as the fitted line.

TKE rate of change

Using the TKE time series its rate of change is calculated. The approach chosen relies on identifying for each 10 minute instance the rate of change with respect to the value before and after it to subsequently take the average of the two. When only one of them is available this is used on its own. To compare the changes in TKE, the dissipation rate estimate needs to be retrieved for a series of 10 minute times at the various cell positions along the water column. Because the focus on a restricted period of profiles is

sufficient to allow a comparison between the values that dissipation and production rate take in the context of the observed change in TKE, it is chosen to hold on to a visual verification of the quality of the fit of the -5/3 sloped line that results from the selection of the vertical axis intercept. This simultaneously allows to mark those spectrums that do not feature an inertial subrange.

6. Results

Using the prepared data, the methods described to answer each of the sub research questions allow to present the findings accordingly. While the direct results are commented on, observations made when performing the analysis also invite to add some complementary insights that justify, adjust or clarify the presented approach and content. These sections are presented as indented from the main text.

6.1. The interrelation between the density stratification and flow conditions

Before using the density interface delineated along the full period of available data in the study of the depth averaged velocities and TKE to understand the general flow conditions at the hollow that can be associated to flushing, the observation of the interface is itself given some attention.

The density interface

The delineated interface corresponds with the expectations from the CTD time series

At the start of the first monitoring period, shown in Figure 15, the water in the hollow at location 1 has a salinity conform to the river background concentration. The gate operation regime is identified from the Kier Data Tool of Rijkswaterstaat (n.d.-a). When the gates allow partial saline water inflow the conditions to carry the salt water to the hollow, that is based upon its center about 2.9 km from the gates, need to be favorable because the inland directed velocities observed at the hollow are relatively weak. Overall, during period 1, the flow velocities are low when compared to those achieved in periods 2 and 3 where especially the towards the sea directed positive velocities are larger.

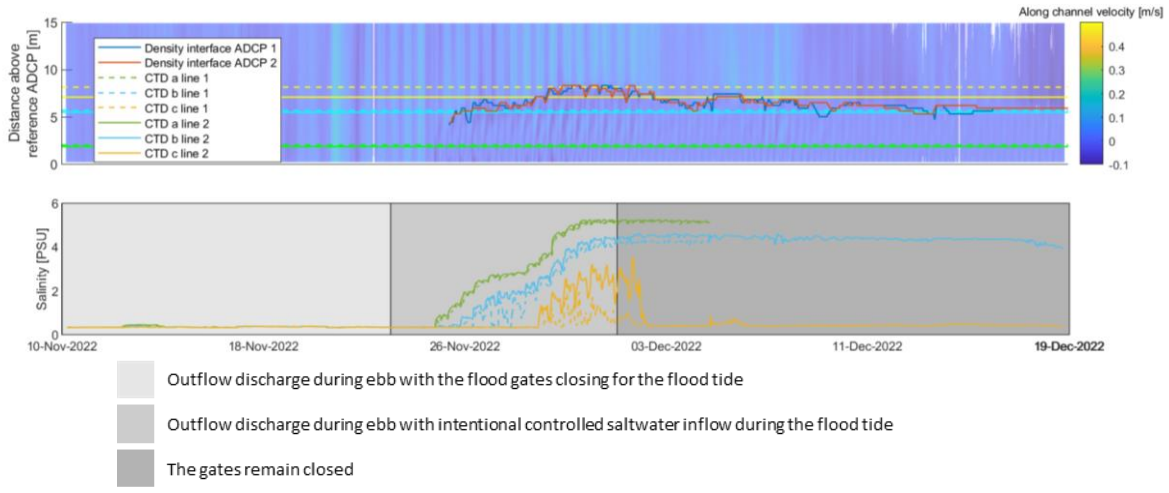

Figure 15: The density interface present during the first monitoring period alongside the along channel velocity and the salinity time series put in perspective by the flood gate operating regime indicated by the gate opening times and the discharges.

The deepest positioned CTD-a indicates that the hollow is filled with the denser fluid when a landward directed current reaches the hollow. An interface becomes distinctly visible from the along channel velocity profiles as the flow direction is reversed. During the filling period, that lasts until the beginning of December, salt is sequentially detected more upward along the water column by the CTDs as the interface level is increased. This suggests that the salt water, inclined due its density to occupy the lower water layers, enters the hollow from along the bed while not being present throughout the entire water column. With each flood event some additional salt accumulates and causes the density interface level to rise. When the interface level is still around that of a CTD it is possible that over the ebb time the positive

directed overflowing velocity reduces the salinity observed at the CTD while the effect on the delineated interface directly is less clear. As the flood gate operating regime is changed to the gates remaining closed, the level of salinity at CTD-c is not sustained. This is because it is too much under the influence of the main flows that exist outside the hollow. Accordingly the salt is taken up into the surrounding flow while the interface does remain rather stable above and around CTD-b, suggesting that this is the level up until which the hollow remains filled if the overflowing current does not get sufficiently strong to trigger a flushing event. It is further noticeable that a vertical salinity gradient remains below the interface with the values of CTD-a continuously exceeding those of CTD-b.

For the period that the gates are kept closed, the stratification remains steady. The interface delineated from the velocity profiles appears to properly follow the overall expected interface even during this low flow period that exists under the closed gates regime. However, for the second monitoring period at the same location the fit is more questionable. Indeed, Figure 16 shows that around the 24th of December the interface delineated exceeds CTD-c while no higher salinity is observed by that CTD. However this low flow period is not of prime concern, and during the higher flow velocity conditions it does apply that each time the interface is drawn up to CTD-c the instrument also picks up the presence of the salinity.

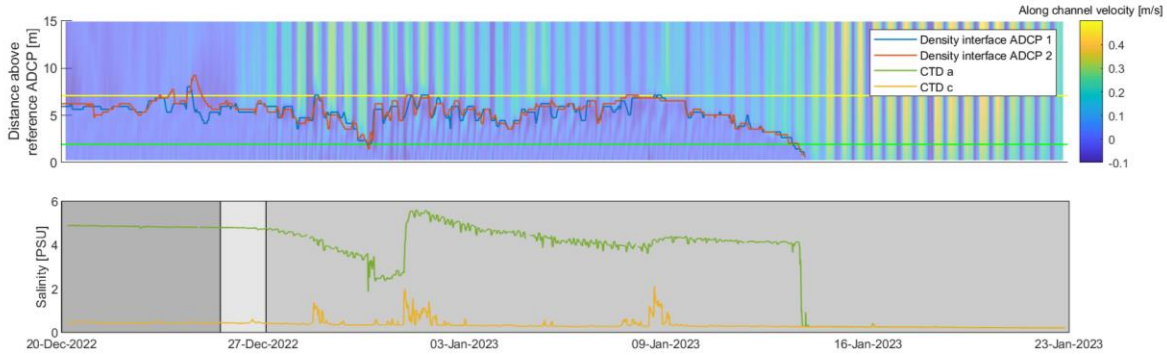

Figure 16: The density interface present during the second monitoring period alongside the along channel velocity and the salinity time series put in perspective by the flood gate operating regime for which the legend of Figure 15 applies.

Figure 17 shows that the salinity at location 2 during the third monitoring period does not reach the levels observed previously for location 1. However, the density gradient remains sufficient to induce differences in the velocity regime such that an interface is delineated. Again, the times that higher salinity records at the CTDs are observed coincide with those that the delineated interface is around or above that position.

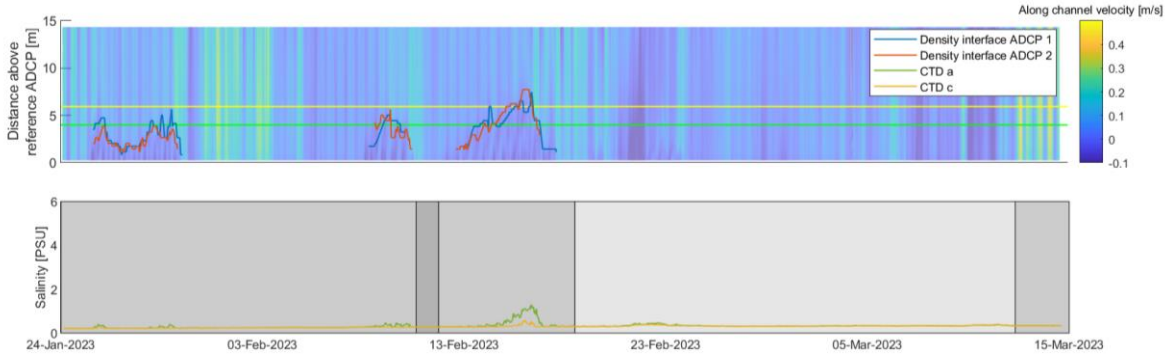

Figure 17: The density interface present during the third monitoring period alongside the along channel velocity and the salinity time series put in perspective by the flood gate operating regime for which the legend of Figure 15 applies.

Three complete flushing events or times of major interface lowering are identified for each hollow

During monitoring period 2, the delineated interfaces allow to distinguish three occasions of consistent interface lowering at location 1 as indicated in Table 1. Under very different conditions for the more landward situated hollow, it occurs three times that salt water becomes accumulated in the lower part of the channel and is subsequently flushed. The flushing events chosen to focus upon appear to be triggered by along channel velocities in the layer overflowing the interface. These currents are expected to follow from the allowed discharge through the flood gate because the flow velocities are much lower when the flood gates are kept closed.

Table 1: Time ranges of the major interface lowering events for both locations.

Event nr.	Start time	End time
Second monitoring period (Location 1)		
1	28-Dec-2022 20:15	30-Dec-2022 19:15
2	03-Jan-2023 22:05	04-Jan-2023 21:25
3	10-Jan-2023 13:25	14-Jan-2023 17:35
Third monitoring period (Location 2)		
1	29-Jan-2023 21:45	30-Jan-2023 14:25
2	09-Feb-2023 17:45	11-Feb-2023 03:05
3	16-Feb-2023 18:05	17-Feb-2023 20:45

The available CTD profiles allow to illustrate the choices made to delineate the density interface

To give an indication of how the metrics of interest can vary with depth prior to addressing the depth average velocities in the next section, the CTD profiles are considered alongside those available from Signature ADCPs as each monitoring period is initiated. At the start of the first and third monitoring period, there is no salt water in the hollow which is reflected in Figure 18 by a linear density profile. At each period, the density profiles near the ADCPs are close to identical because the depth average temperatures and salinities also correspond. However, at the start of the third monitoring period, the density exceeds that at the start of the first monitoring period despite that the salinity is lower. Therefore, it is a reduced temperature that allows the higher density value to be achieved.

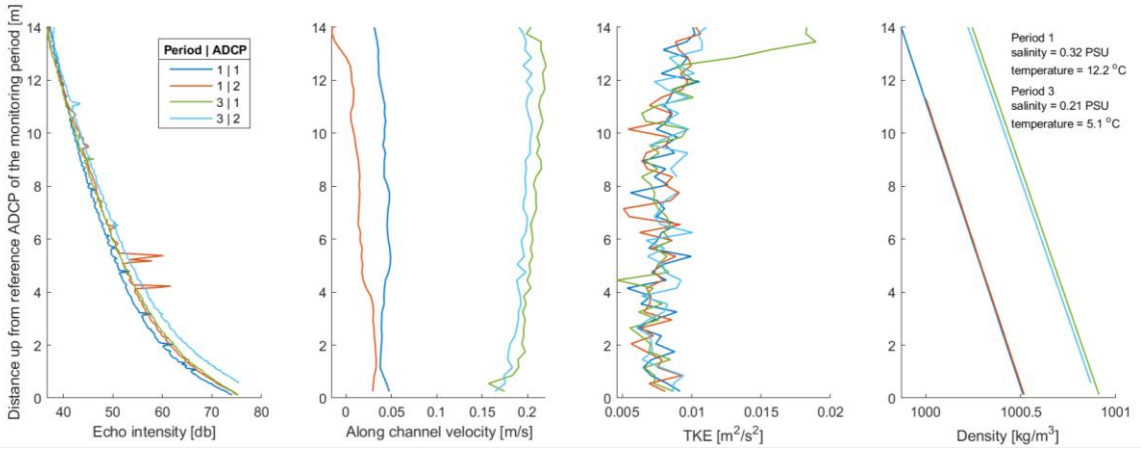

Figure 18: The Signature ADCP derived echo, velocity and TKE profiles that correspond the closest to the time of the available CTD based density profile. Profiles from both ADCPs related to the initiation of the first and third monitoring period are included and referred to using the monitoring period to ADCP number combination. The correspondence of the profile times is commented on in Section 4.3 and the exact dates are provided in Table 3 of Appendix 2.

The observed velocities are almost stagnant at the start of the first monitoring period. During the higher velocities, observed at the initiation of the third monitoring period, the classical shape of a near constant value that decreases near the bed is apparent. Despite the difference in velocity magnitude and hollow geometry, the TKE profiles of all are within the same range of values and only slightly increase towards the surface, indicating that surface waves can still affect the top part

of the considered water column. For profiles associated to period 1, the small local peaks in the echo, especially the most prominent ones between 4 to 6 m up from the reference Signature ADCP for the monitoring period, could be mistaken to indicate an interface of which no account is present in the subsequent plots.

Considering the CTD profiles of Figure 19, that coincide with the starting point of the second monitoring period, gives an illustration of the response of the ADCP derived variables to the presence of a density interface. The velocities are landward at this time where the flood gates remain closed and are thus driven by wind. The echo intensity presents a local peak as does the TKE while the along channel velocity demonstrates a transition between the higher velocity overflowing the established density interface to the near stagnant water below this boundary. Both TKE lines feature a missing entry that arises because either $\overline{u'u'}$ or $\overline{v'v'}$ has a negative value that is not a valid entry for a normal Reynolds covariance.

Building upon the already made observation in Section 5.1 about a clear along water column interface not consistently showing up in the echo data, it is here emphasized upon that the selection of the peak that pertains to the interface from the echo profile also becomes difficult due to high values that occur next to the peak of interest. In Figure 19 it appears that it is the first peak from the surface down that is of interest. However, for other profiles it occurs that there are disturbances above the interface too. If the interface could be located with the echosounder, it's position is most accurately determined. Based upon the example shown the interface from the echosounder is 0.25 m above that insinuated by the density profile. This is equivalent to five along depth data points in the echo data and is inferior to the cell resolution with which velocity and TKE are available. It is unclear if this small difference in interface position actually applies or if it stems from an error introduced by converting pressure to depth for the CTD profile.

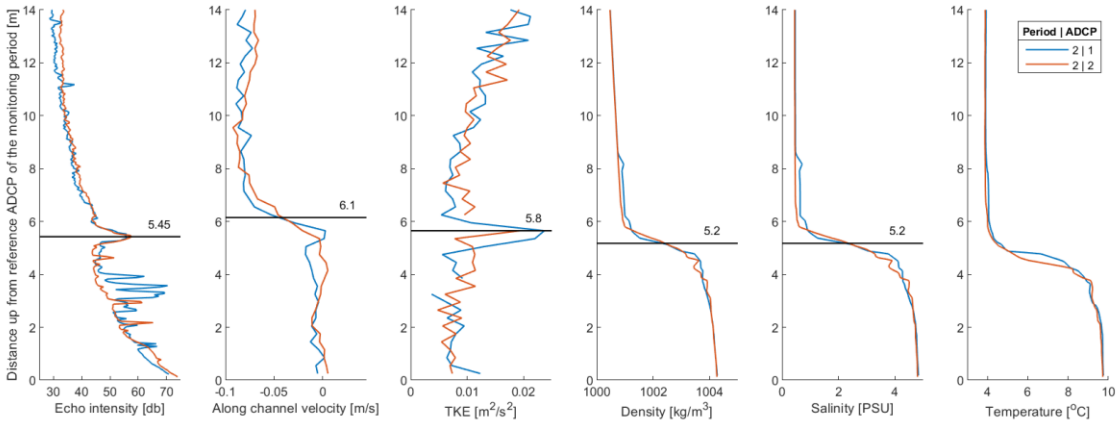

Figure 19: The Signature ADCP derived echo, velocity and TKE profiles, with characteristic interface positions, that correspond the closest to the time of the available CTD based density profile. Profiles from both ADCPs related to the initiation of the second monitoring period are included.

The used strategy to delineate the interface relies on the along channel velocity profiles. For the situation of Figure 19 this however gives an interface position that is furthest from that indicated by the density profile. It indeed appears that the low velocities are conserved up to the position indicated by the density interface and only subsequently accelerate above this level. The interface

position difference of 0.65 m spans more than two along depth data points of the velocity profile. However, from the available options the delineation of the interface through the velocity profile is the most consistently applicable thought the data collection period. Indeed, the transition between the different along channel velocity conditions above and below the interface can generally be observed while the density change does often not show in the echosounder data.

The used method to delineate the density interface from the velocity profiles, as describe in Section 5.1, followed from observing that the focus on the highest gradient point of the smoothed profile generates an interface position time series that does not perform well to indicate a smooth interface that is not affected by vertical shear elsewhere along the water column. Indeed, despite that around the interface there tends to be a velocity gradient peak, further along depth variability in flow conditions can induce other peaks while under low flow conditions the velocity transition at the interface becomes too subtle to notice. This issue is addressed with the option of the semi-automatic delineation despite that it remains problematic to indicate the interface position during the lowest flow conditions or when the direction of the current reverses. However, interpolation overall seems a reasonable solution to address this incompleteness that can more conveniently be dealt with than inappropriately selected values.

The depth averaged flow conditions

The overflowing velocities characterize the incoming currents driven by the external forcings

With the observation that the selected flushing events are triggered by towards the sea directed velocities prevalent at the hollow, it is relevant to understand their relation to those approaching the analyzed system of interest. This insight is provided by the comparison of the RDI ADCP's to the Signature instrument that is closest to it.

With the RDI ADCPs using the four slanted beams, the comparison remains restricted to the horizontal velocity magnitude and orientation. The depth average is used to focus on the temporal variations instead of the spatial variations that exist along the water column that are acknowledged by the standard deviations linked to the mean values. Five more cells near the top of the valid water column set in Appendix 2 for the Signature ADCP are removed after observing that the largest deviations from the mean dominate over that water column portion. Further, the orientation information is reduced to the degree of along channel direction alignment by taking the cosine of the angle that resultant velocity vectors make with respect to the set positive x axis. A value of 1 indicates that the flow is along channel and directed towards the sea such that the opposite direction is linked to -1 while 0 indicates across channel flow.

Considering the second monitoring period in Figure 20, the standard deviation computed across depth indicates that in the absence of strong forcing currents, such that the depth averaged velocity magnitude is comparable to its standard deviation, the debt average value of the orientation is not a good metric to summarize the variable resultant flow directions. However as soon as the larger velocities become involved, the directionality is distinct during the periods of flow towards the sea. That generally under low flow velocities the orientation is less clear is supported by Figure 21 for period 3 that emphasizes on this link between the higher flow velocity and the stable velocity orientation due to the successive presence of low and high flow periods.

For location 1, the correlation of the velocity magnitude between ADCP-3 and ADCP-2 is very strong with a 0.96 coefficient that is lower for the hollow at location 2 for which a value of 0.87 is found. In both cases

the difference between ADCP-3 and ADCP-2 does not seem constantly systematic. Further, there is also similarity in the velocity orientation between the ADCPs with the correlation coefficients being respectively 0.79 and 0.71 for both hollows. These correlation values are restricted by the times where a high standard deviation at the ADCP-3 applies. Because this comparison upholds based upon the data above the interface when a density stratification is present, while also when there is a homogeneous water column, this illustrates that despite the depth increase the velocity magnitude or orientation is not strongly affected by the hollow itself.

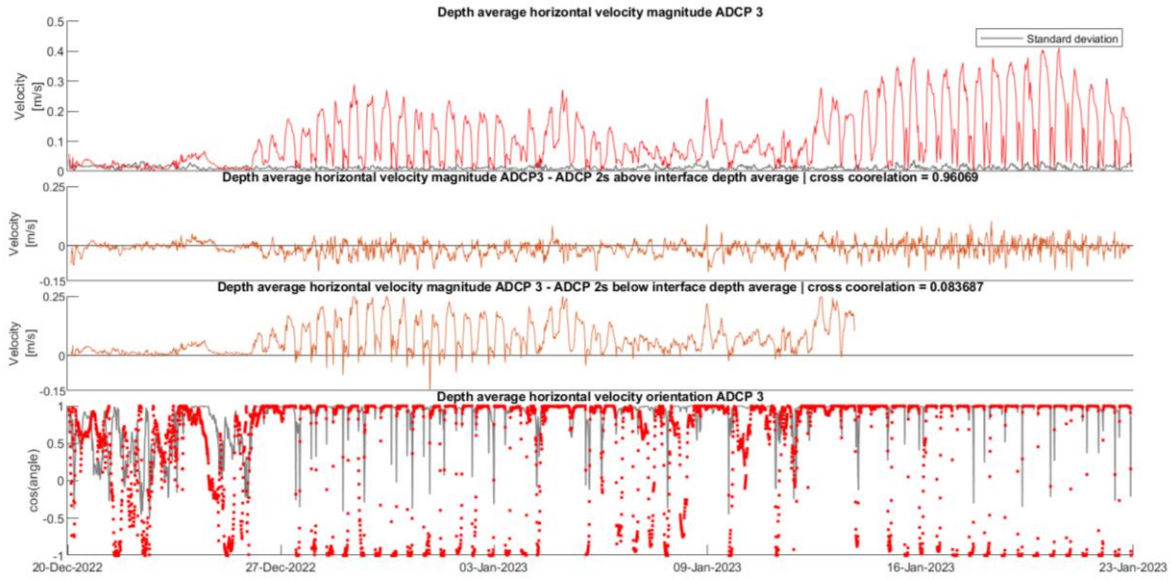

Figure 20: The depth averaged velocity orientation and magnitude of ADCP-3 compared to the velocity magnitudes above and below the density interface at ADCP-2 during the second monitoring period.

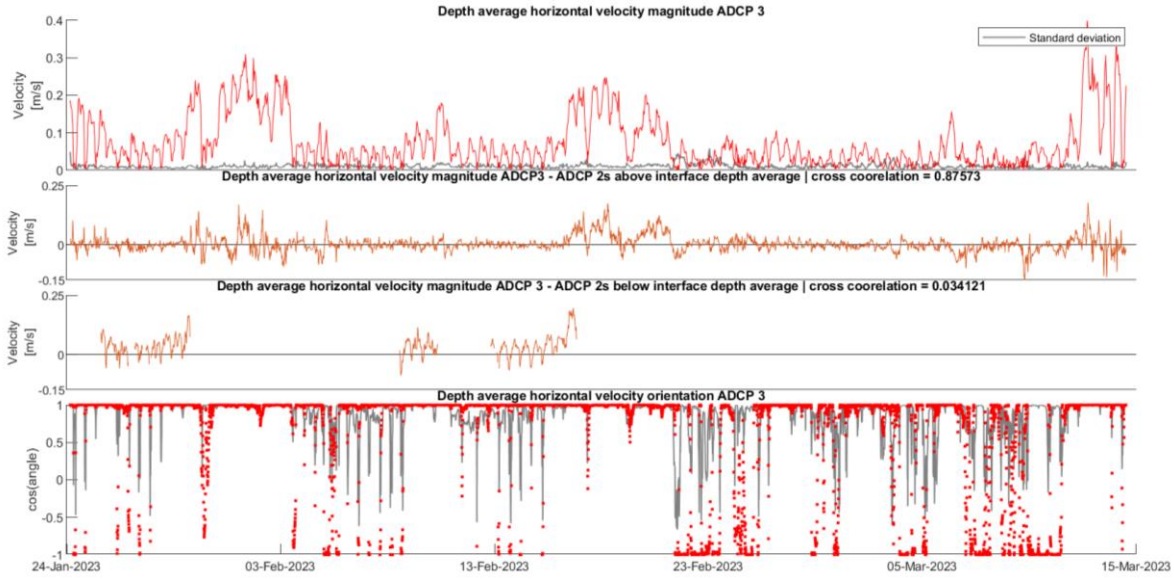

Figure 21: The depth averaged velocity orientation and magnitude of ADCP-3 compared to the velocity magnitudes above and below the density interface at ADCP-2 during the third monitoring period.

The below interface depth average velocity magnitude conditions are poorly correlated to those at the ADCP-3 featuring values of 0.08 and 0.03 across the last two monitoring periods. Indeed, considering the plot of the difference in velocity magnitude between the ADCPs, the deviation closely corresponds to the velocity at ADCP-3, insinuating that below the interface at ADCP-2 the flow is about stagnant. Orientation wise, the below interface depth average velocity is very variably different from that of ADCP-3 indicating that no consistent directionality is upkept within the hollow under the lower flow magnitudes.

Regarding ADCP-4, the velocity magnitude and orientation have correlation coefficients of 0.70 and 0.54 with respect to the above interface conditions at ADCP-1. The magnitude differences are expected to be explained by the noticeable differences in orientation. For example, the high flow period between the 15th and 20th of January observed at ADCP-3 does not show at ADCP-4 that instead of the positively oriented velocity profile has an unclear pattern of orientations for which the depth average does not provide a representative value. Because of its position in the wider portion of the Haringvliet, relative to the restricted channel where ADCP-3 is during the third monitoring period, it is expected that more complex estuarine circulation processes influence the observations at ADCP-4. The instrument thus does not necessarily directly reflect the currents exiting the channel.

The role of wind in estuary circulation processes can be prominent and accordingly potentially influence the observed velocities. Indeed, it can be noted for the second half of the third monitoring period that the prevalent inland directed velocities must be forced by the wind. Therefore, the possibility of wind induced flushing as described by Kranenburg et al. (2023) for the Haringvliet is indeed relevant to acknowledge.

The wind conditions do not dominate the currents during the flushing events

To be aware of possible wind extremes associated to the flow velocities observed during the flushing events, the time series of the wind orientation and speed are consulted in Figure 22. Although there are direct wind time series available as a historic download from the Waterinfo page of Rijkswaterstaat (n.d.-a), it does not feature records over the range of interest. Therefore, two long term weather station datasets available from KNMI (2024) are used.

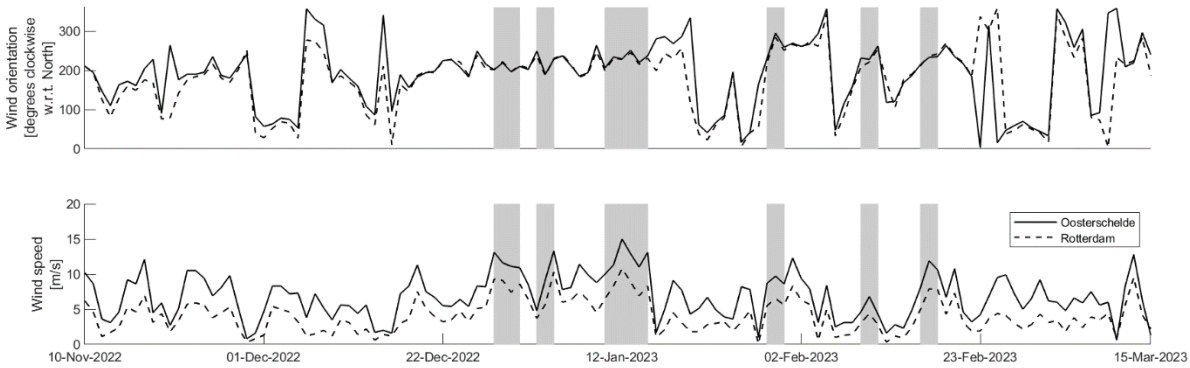

Figure 22: The identified flushing events, shown as grey bands, in the context of the wind orientation and speed of the resultant vector mean retrieved for the Oosterschelde and Rotterdam from KNMI (2024).

The strong agreement between the two stations, of which one is located approximately 50 km south and the other about the same distance north of the Haringvliet, allows to state with confidence that the wind blows from the south west during each of the marked flushing event. This orientation is indicated by Kranenburg et al. (2023) to be the most dominant for the

Haringvliet estuary. Further, although the wind velocity magnitude is less comparable between the two weather stations, and thus the value applicable to the Haringvliet less clear, the strength of the wind during the flushing events is amongst the stronger values observed over the winter considered while not in turn exceptionally standing out. Therefore based upon the low velocity magnitudes observed in the dataset when the flood gates remain closed, allowing the wind to freely induce currents, it is expected that the wind can only adjust prevailing discharge currents.

It is not the interface overflowing velocity that appears to especially stand out during the flushing events

Figure 23 shows the identified periods of major interface lowering on the time series of the depth average velocity magnitude observed above and below the interface. The range of velocities over which the interface lowering occurs at location 1 is variable. Especially the third flushing event features velocity magnitude values that are amongst the lowest observed during the period that the flood gates allow outflow with controlled inflow. Further there is no systematic difference between the observations at the two ADCPs in the hollow, returning a near perfect correlation coefficient of 0.99.

Regarding the below interface velocities, despite these having much lower values that are of the same order of magnitude as the standard deviation, several peaks are present. For these the standard deviation is not clearly higher, indicating that these do arise from a more unanimous but short lasting pattern in the below interface velocities. Their timing coincides with the reestablishment of higher velocity magnitudes at the end of the low flow period. Comparing these observations from the two ADCPs, indicates that the peaks are different at ADCP-2.

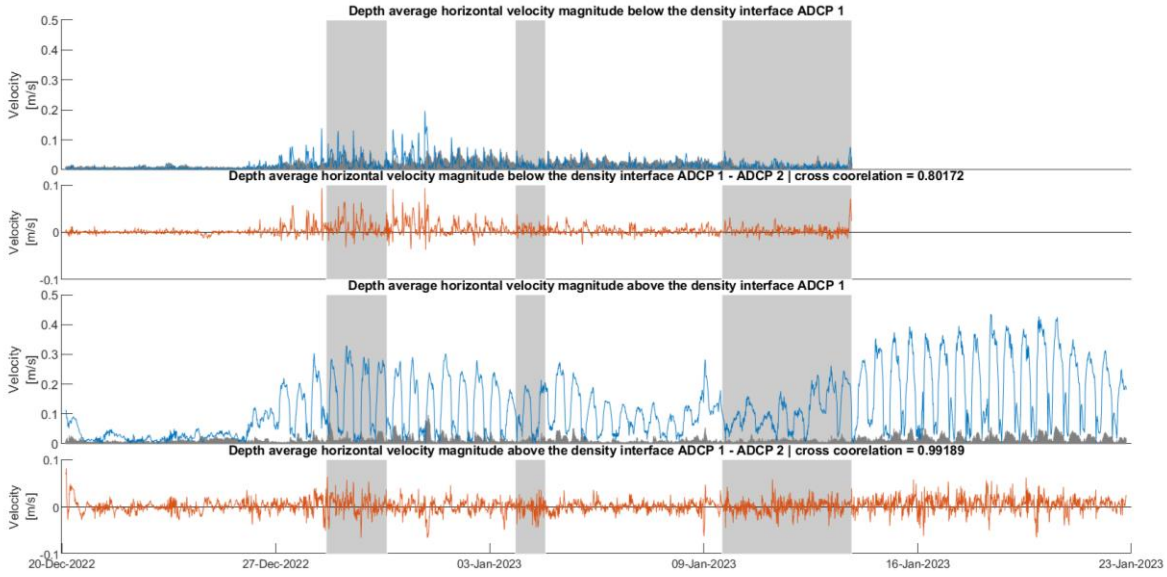

Figure 23: Comparing the depth averaged velocity magnitude of ADCP-1 to ADCP-2 during the second monitoring period. The grey bands represent the times of major interface lowering while the bars indicate the standard deviation.

Considering location 2 monitored during period 3, the correlation between the two ADCPs is weaker but still above 0.9 as is shown in Figure 24. There appears some systematic pattern in the difference between the two ADCPs when considering the times of higher flow velocity magnitude. At the peak value observed at ADCP-1 the corresponding ADCP-2 value is lower, but as the velocity at ADCP-1 decreases from this highest point then ADCP-2 exceeds that at ADCP-1. However, this is not confirmed when recalculating the correlation coefficient with a phase shift between the two time series.

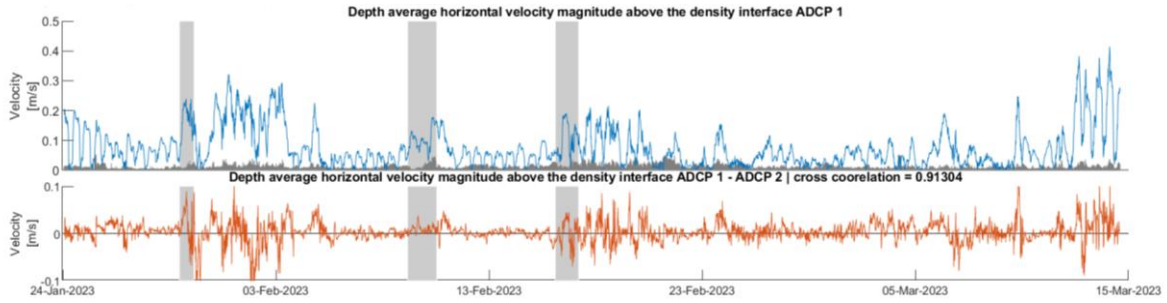

Figure 24: Comparing the depth averaged velocity magnitude of ADCP-1 to ADCP-2 during the third monitoring period. The grey bands represent the times of major interface lowering while the bars indicate the standard deviation.

During the third monitoring period the hollow is overall free of salt water and the salinity only increases on three occasions. For each of these, the hollow becomes rapidly flushed as the overflowing velocity increases relative the lower magnitude period over which the salt water accumulated in the hollow. The still relatively low velocities exceeding 0.1 m/s already appears sufficient when looking at the second flushing event.

The towards the sea directed currents dominate during flushing but tidally driven inland currents are prominently present as well during one event

For the times that interface level lowering is observed in Figure 25, positively oriented flow dominates and is associated to the highest velocity magnitudes. However, as illustrated best during the first event, also inland velocities occur during the periods marked with grey bands. This is observed with each tidal cycle during the first flushing event but only occasionally and partially during the third flushing event that removes all salt from the hollow. Throughout the complete second monitoring period, several instances of inland directed velocity are observed that can allow for new salt water to be brought to the hollow. Nevertheless, this often does not occur as can be seen based upon the last portion of the time series during which no saltwater accumulation is observed despite the reoccurring inland oriented currents.

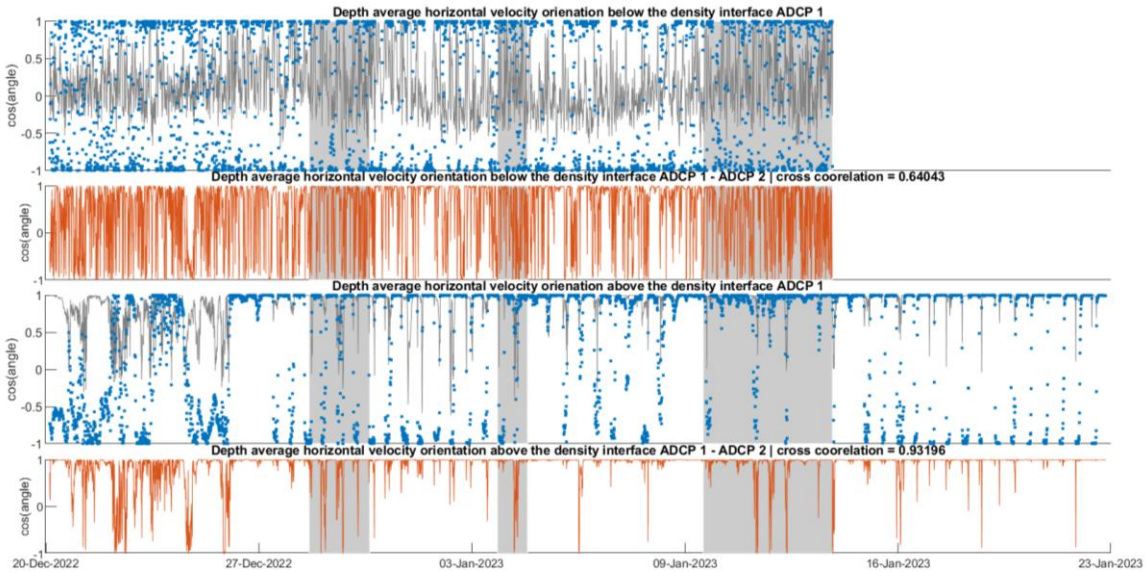

Figure 25: Comparing the depth averaged velocity orientation of ADCP-1 to ADCP-2 during the second monitoring period. The cosine of the orientation angle, that applies with respect to the along channel aligned axis system, is shown to illustrate the degree of along channel alignment of the flow orientation.

When ADCP-2 is compared to ADCP-1, a 1 indicates correspondence and a -1 opposition of the flow direction observed amongst the ADCPs in Figure 25. Above the density interface the correlation between the flow direction observed at both ADCPs is strong with a coefficient value of 0.93. Noting that most deviation occurs during the period that the gates are kept closed, a stronger correlation value would result when not considering this period. Despite the much greater flow variability through time and along depth below the density interface, the correlation coefficient is still 0.64. It appears that the correspondence of orientation between the ADCPs mostly occurs under the negative below interface depth average orientation.

For the hollow at location 2, Figure 26 shows that the dominance of the positive flow directionality is strong over the period that the three flushing events are identified. During flushing, velocities are continuously positive despite that towards the end of the third event the directionality of approach is slightly sidewards from the along channel direction.

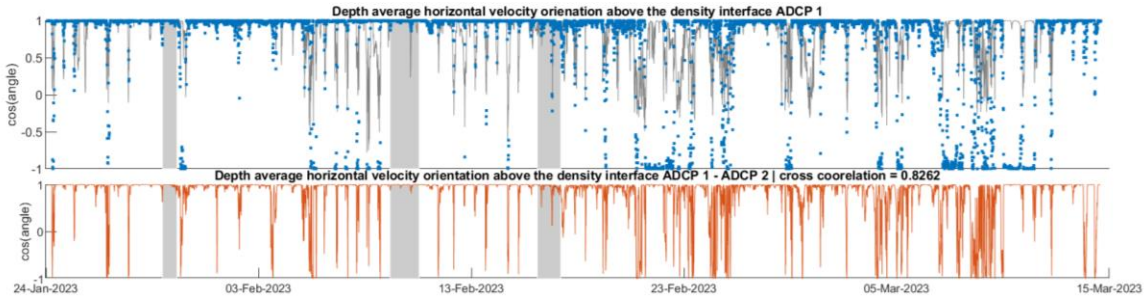

Figure 26: Comparing the depth averaged velocity orientation of ADCP-1 to ADCP-2 during the third monitoring period.

When there is no salt water accumulated and the stronger velocity magnitudes are observed, the orientation of the flow follows the found along channel direction well for both hollows with little along depth variability. Therefore, it appears the hollow itself does not alter the directionality along the water column such that the above and below interface orientation differences arise because of the stratification.

The TKE above and below the interface are taking constant values though time during flushing events

When considering the time series of the depth average TKE, shown in Figure 27, it fluctuates in a narrow band around a constant value while the along water column variability from this value is restricted. The over depth averaging of the TKE, that is itself like a sample average of velocity variances from the different along axis components, is used to reflect the variance value that tends to apply along the water column. In turn the standard deviation of the TKE indicates the variation in prevailing velocity variance. The constant level TKE seems equal on either side of the interface where it is noticeable that the at ADCP-2 observed TKE is systematically slightly higher than at ADCP-1. This is most prominent above the interface but also visible below it. Also, during the third monitoring period only occasional TKE values are observed above this apparent continuous minimum value that is around 0.0075 m^2/s^2. Because of its constant nature it could possibly be related to the minimum threshold of variance that can be detected by the instrument that is restricted by the effect of the Doppler noise.

During the first part of the second monitoring period, the TKE above the interface exceeds that below it. Further there is more variation in TKE along the water column portions averaged over. This is explained by how, with the lower velocity magnitudes that occur, the orientation along the water column does not take a set directionality as is indicated by the high standard deviation in the depth average velocity orientation.

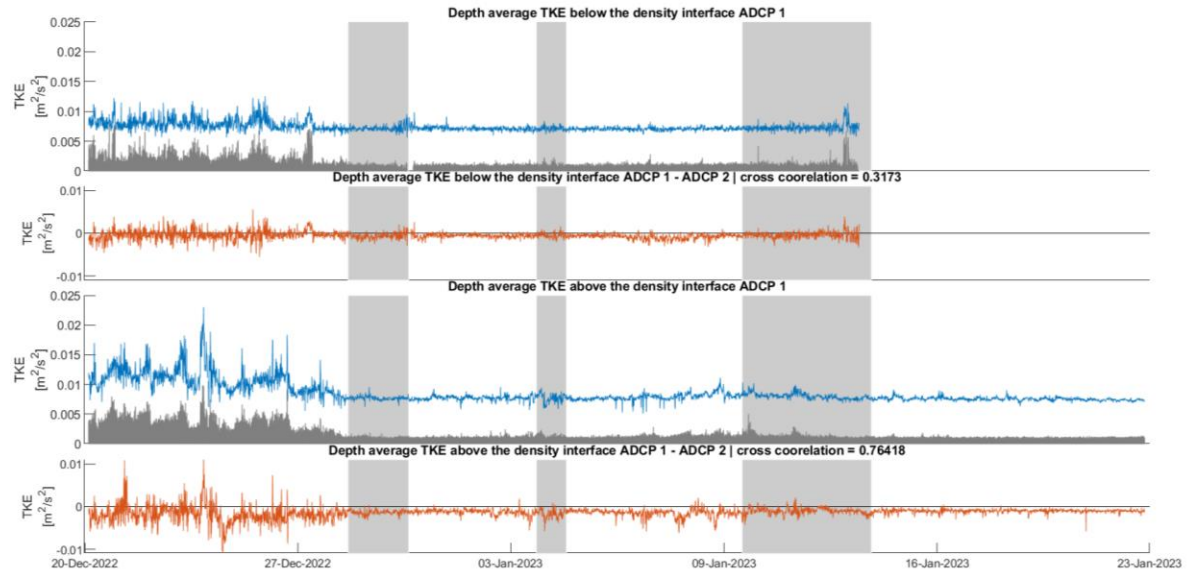

Figure 27: Comparing the TKE of ADCP-1 to ADCP-2 during the second monitoring period.

Of the ADCP pair, the more upstream one observes upwards vertical velocities while milder downward ones occur at the downstream positioned instrument

In contrast to the observations from the hollow at location 2 or from below the interface at location 1, the vertical velocities observed above or without the density interface during the second monitoring period have the distinct pattern shown in Figure 28. The peaks in vertical velocities are observed at the same time as the horizontal ones. Further, when a downward oriented velocity is observed at ADCP-1, a larger upwards velocity is observed at ADCP-2. Regarding remaining variations from the mean along the water column portion these tend to be small with the standard deviation consistently taking values around 0.03 for both ADCPs.

Consulting the horizontal flow orientation, it can be observed that for the times of seaward flow the vertical velocity at the upstream ADCP-2 is upwards while it is downwards ADCP-1. At times of inland directed flows, the opposite occurs although less noticeable because of the lower velocities that tend to be involved. The pattern persists throughout the time series where the flow directionality is aligned with the along channel orientation. Thereby the first part of the monitoring period is ruled out while the phenomenon is observed under conditions with and without accumulated salt in the hollow.

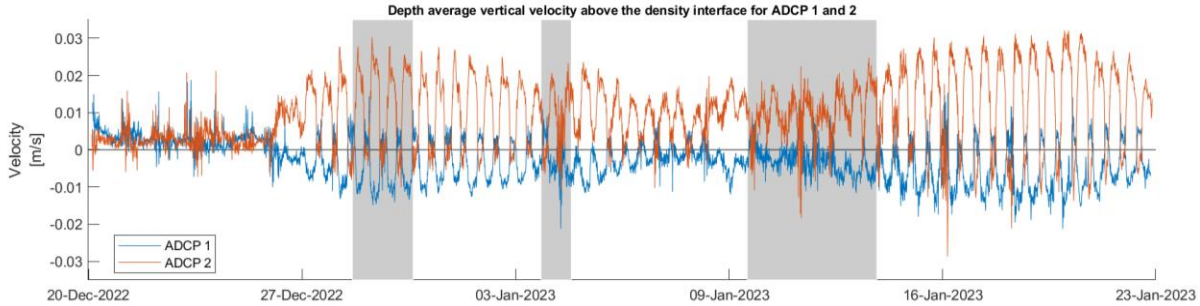

Figure 28: The vertical along beam velocities observed during the second monitoring period at location 1.

Recalling the in Section 2.4 described flow dynamics over a hollow, the here observed vertical velocity pattern appears to link to the by Roos et al. (2008) described phenomenon of a longitudinal pressure gradient building up over the hollow as a manifestation from two dimensional Continuity and Bernoulli principles. A schematic illustration of how the vertical velocities are interpreted is included in Figure 29. However the by the hollow induced dynamics could contribute to the way accumulated salt water is flushed from the hollow which is a topic further considered in Section 6.2.

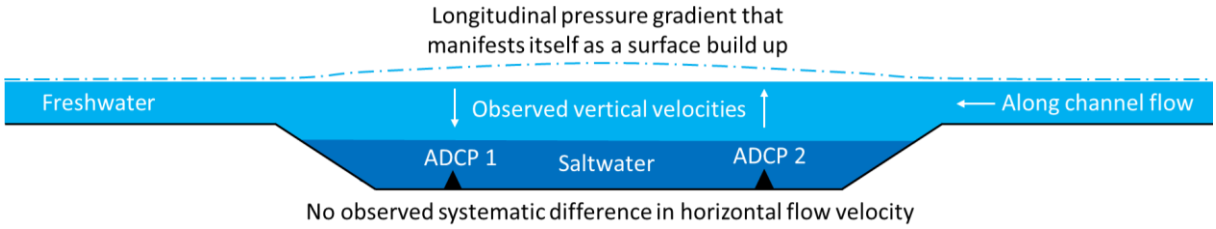

Figure 29: Schematic illustration of the interpretation of the observed vertical velocities for an incoming positively directed along channel current. The observation upholds with or without accumulated salt water.

The localized bed depression at location 1 appears to lend itself more to in hollow dynamics than the elongated deep channel section at location 2

The pattern in vertical velocities observed at location 1 invites to clarify the observed influence of the bed depression itself on the incoming flow. The comparison of the RDI to Signature ADCPs already revealed that the external forcing currents are closely matching those observe in the empty hollow or those above the density interface if a stratification is established. While for both hollows the differences are overall not systematic, there are some portions along the time series of Figure 20 and Figure 21 that could be interpreted as showing flow acceleration or deceleration. Indeed, for the second monitoring period throughout January up until the point that the hollow is completely flushed of salt water, it does appear that as the velocity magnitude peaks the value at ADCP-2 exceeds that at ADCP-3 suggesting flow acceleration. However, during the period where there is no salt water in the hollow or in December no such subtle pattern prevails. In turn during the third monitoring period there is the stronger velocity period between the 15 and 21st of February where the velocities at ADCP-3 seem systematically higher than those at ADCP-1 suggesting that the current decelerates when entering the hollow at location 2. However again there is no general support for this pattern. Further, the ADCPs aligned along the central axis of the hollow are not expected to pick up observations from lateral flows associated to recirculation cells. In any case, the patterns indicate that it could be possible that there is some flow acceleration at location 1 while some flow deceleration at location 2 but the pattern actually observed depends on more than the hollow geometry alone and there is no direct explanation prevalent from the observed velocity orientations.

Because there is no dedicated deceleration of the flow entering the hollow at location 1 as would be expected from two dimensional continuity, it appears possible that the longitudinal pressure gradient, mentioned in Figure 29, contributes to a lateral one that powers recirculation cells to maintain the flow velocity around the level that enters it. Indeed, the discussion in Section 2.4 indicates that alteration of the flow velocity along the main axis of the hollow is highly situation specific. The observation of this suggests that in hollow dynamics can be more important for location 1 than for the elongated channel at location 2.

The observation of logarithmic velocity profiles outside and in the hollows indicates that the observations are not disturbed by flow separation

The positive vertical velocity component at ADCP-2 indicates that the resulting stream lines are drawn slightly upwards. However for such cases based upon a sudden increase in flow depth, Terekhov et al. (2022) show that the wake vortex can influence a longer along flow length than if the streamlines would be drawn downwards directly to follow the bed at the upstream side. Therefore, it is relevant to consider if the observations at ADCP-2 are affected by flow separation.

Considering the fit of the observed profiles to the expected logarithmic based shape described by equation 1 allows to improve the understanding of how the hollow itself affects the velocity profile and give some justification to the usefulness of depth averaging. Indeed, fitting this regression to the profiles shown in Figure 18 for location 2 produces a coefficient of determination of 0.9 for both, ensuring a good fit as would be expected for the hollow that has a gently sloping bed. Indeed if vortex effects can occur and influence the velocity profile in the absence of a vertical stratification, then these would be more likely for location 1 when referring to the longitudinal transect comparison of Figure 14. Therefore Figure 30 shows the profiles from the ADCPs at a time when there is accumulated salt water and when the hollow does not feature a vertical stratification. When there is no density stratification, the fit of a logarithmic profile has a 0.94 coefficient of determination for both Signature ADCPs with a slightly higher value of 0.98 for ADCP-3. Therefore, the logarithmic profile observed upstream develops into the profile observed in the hollow such that the along water column profile behavior seen at the 29th of December plot completely stems from the stratification and is not influenced by bed geometry.

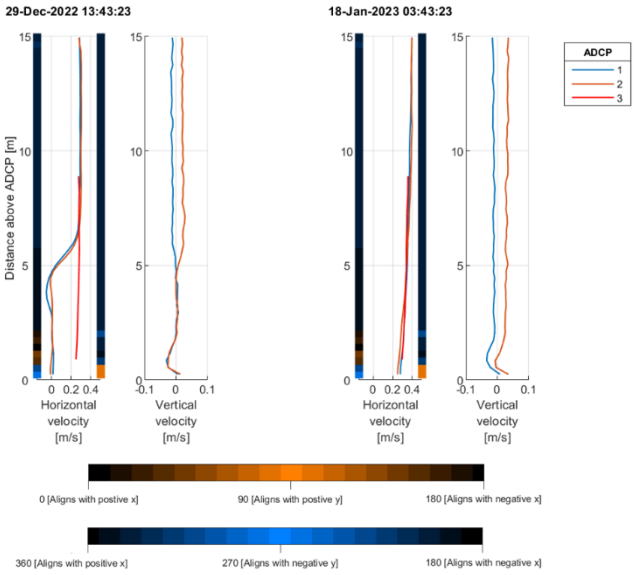

Figure 30: Profiles of horizontal velocity magnitude for ADCP-3 and the ADCP-1-2 instrument pair, for which the orientation is also included, at a time with and without salt water accumulated in the hollow of location 1 for times of peak vertical velocities.

Both times reported in Figure 30 are taken when the vertical velocity at the Signature ADCPs peaks under the influence of a towards the sea directed current. This is to illustrate the constant along depth nature of the vertical velocities with or without salt water accumulated in the hollow. When there is a density stratification the vertical velocities below the interface are near zero. Further it emphasizes upon how the upwards velocities at ADCP-2 are noticeably larger than the downwards one at ADCP-1.

6.2. Density interface evolution during flushing events

To understand the processes that contribute to the flushing of the accumulated salt water, the observations from the individual events are presented separately for the two hollows. Indeed, the local geometry differences between the locations are expected to affect the flushing mechanisms that prevail.

Location 1, the most seawards hollow

The density interface remains horizontal during flushing events

Figure 31 and Figure 32 show the interface delineated at a higher resolution on the along channel velocity component for the first and third flushing events. Retrieving the position of the highest velocity gradient remains uncertain during the periods of flow reversal, leading to deviations from the overall interface pattern that are left in the figure to illustrate the limitations of a maximum gradient based approach. However the portions with a positive velocity, where the interface is distinct and during which the interface could theoretically tilt, suggest that the interface remains horizontal. The same applies to the second flushing event that is not shown based upon the resemblance to the conditions at the start of the third event.

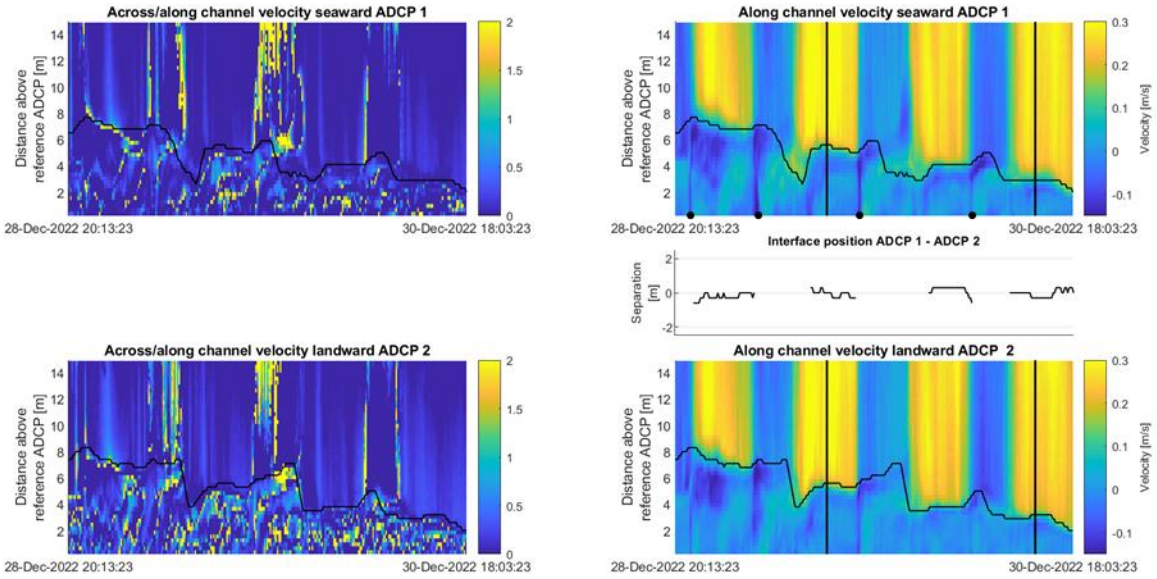

Figure 31: Along and ratio of across to along channel velocity profiles with delineated density interface for the first flushing event during the second monitoring period.

The velocity conditions during the two shown events are very different as already noted previously based upon Figure 23. The first event shows strong along channel positive velocities when the flood gates discharge water to the sea. Negative currents of a lower magnitude are possible when the gates allow saltwater inflow. Noteworthy is that if any salt is brought to the hollow at those times of negative flow, it must be directly flushed away as the positive velocities reestablish because the interface overall follows a pattern of lowering over time. Instead, the third flushing event predominantly has positive velocities that, while initially still low, attain higher values towards the end as the flood gates allow larger discharges.

The ratio of across to along channel velocity is included to illustrate its relative importance, which when set in perspective of the alongside shown along channel velocity also indicates the magnitude of the lateral component. As the along channel velocity features values further away from zero the ratio decreases. This suggests that the resultant velocity vector indeed follows the channel with the lateral component merely contributing a slight reorientation. The pattern shown by the along channel component dominates and thereby confirms the observation of Kranenburg et al. (2023) for the Haringvliet that the lateral flow across the hollow is only small compared to the primary direction of the current through it. Further for the few

times that the across channel velocity dominates above the density interface, it does not feature the along depth consistency that is present amongst the times that the along channel orientation dominates. Below the interface the values of the ratio tend to variably take values across the shown range, confirming the lack of directionality of the lower flow velocity magnitudes observed in the hollow as discussed with Figure 25. However when the along channel flow velocity in the hollow increases, as is observed at certain times during the first flushing event, then the ratio consistently is lowered over the affected spatial-temporal portion of the image, indicating that a more systematic water movement is present below the interface that does align with the main channel direction.

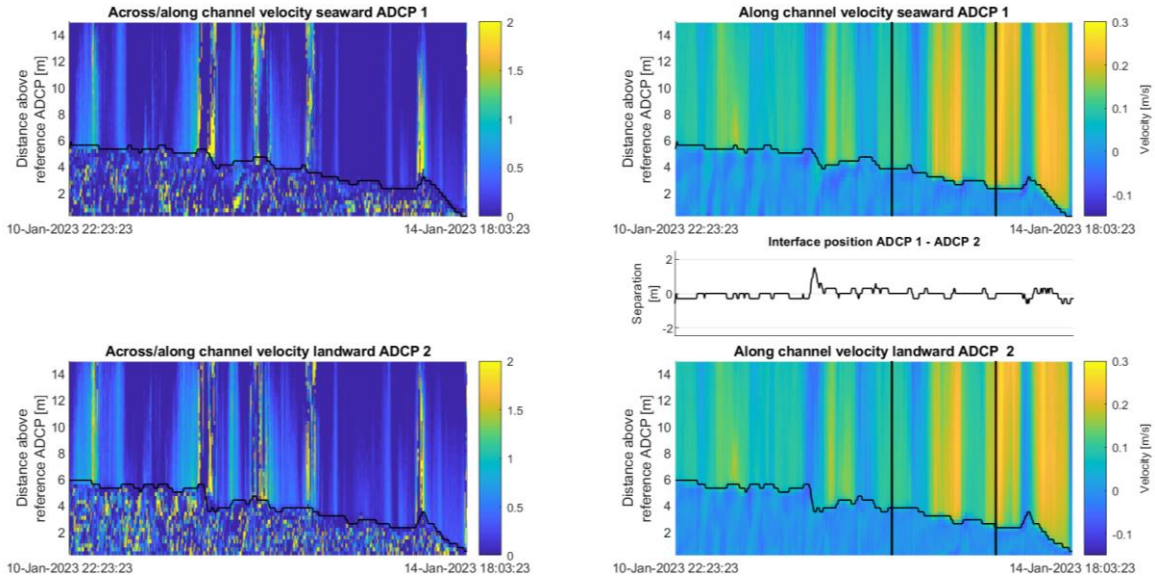

Figure 32: Along and ratio of across to along channel velocity profiles with delineated density interface for the third flushing event during the second monitoring period.

For the first flushing event the flow patterns in the hollow are more complex than during the third event. Indeed, in Figure 31 ADCP-1 most clearly shows how during the strong positive overflowing velocities an opposite current below the interface develops that, as the overflowing velocity slackens, momentarily can occupy the complete water column portion below the interface, exceeding the velocity above the interface. These times, indicated in Figure 31 with the on the axis positioned back dots, correspond to the peaks shown in the below interface ADCP-1 velocity magnitude depth averaged time series of Figure 23. With the weaker negative overflowing velocities, a positive current develops below the interface that near the interface boundary smoothly transitions into the newly enforced positively directed overflowing movement that, as it becomes established, makes the interface distinctively visible again.

The velocity profiles confirm the similarity of the flow conditions at the ADCPs during positive overflow

Considering the equally spaced profiles over a day in between the vertical bounds demarcated in Figure 31 and Figure 32 gives Figure 33 and Figure 34. These illustrate that indeed the interface remains horizontal under the influence of the strong overflowing velocities. The profiles also confirm the along depth consistency of the above interface velocities that align with the set along channel axis system from which the orientation deviations tend to prevailing under the low velocity magnitudes. Figure 33 also hints at the more complex patterns that can exist around the interface. First, the 18:43 plot suggests a slight seaward directed current below the density interface that is induced by the inland oriented interface overflowing

current. Secondly, the 02:13 plot shows the opposite for an inland directed forcing where the below interface current is thus seawards. Additionally, this also features an ever so slight return flow just near the bed, hinting at the possibility of below interface circulations. Finaly, the 07:13 profile at ADCP-1 shows a landward directed below interface velocity magnitude peak that just follows the moment marked with the last black dot in Figure 31. The below interface, towards the inland directed, flow becomes reversed as the inland oriented overflowing current starts to exert its influence. It therefore is relevant to further investigate the flow orientation pattern in the low velocity environment below the density interface. There is no pattern in the below interface velocity magnitudes. The largest values are obtained as the inland directed overflowing current starts to establish while the rest of the velocity magnitudes tends to fade in a range of comparable low values and does not show a link to the systematic pattern of orientations.

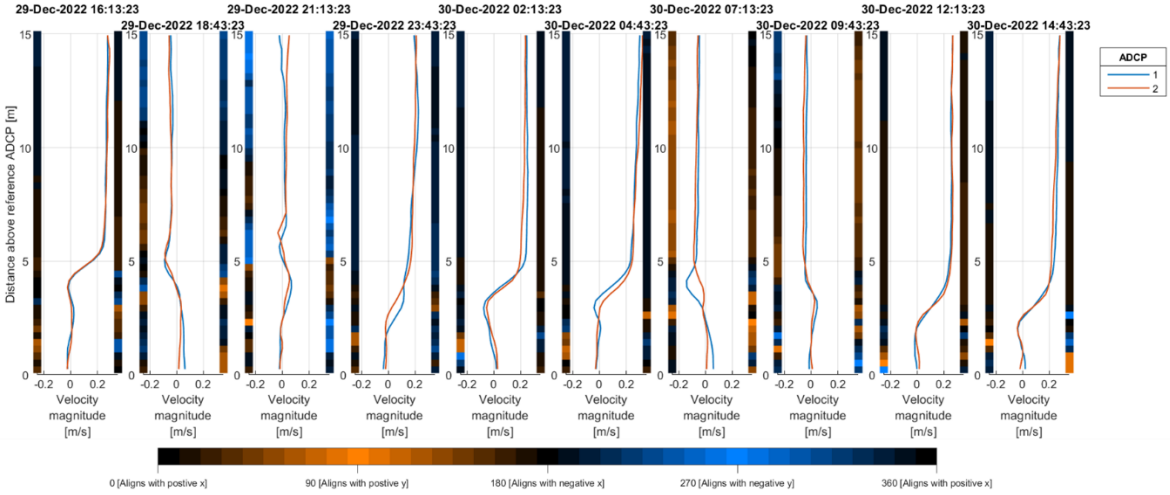

Figure 33: Profiles of velocity magnitude taken from the segment of the first flushing event of the second monitoring period that is shown in between the black vertical lines in Figure 31. The orientation of the horizontal resultant vector is indicated by the color bars on the axes, for which the most left one is for ADCP-1 such that the second bar applies to ADCP-2, that use an added sign to the velocity magnitude depending upon its along x axis orientation.

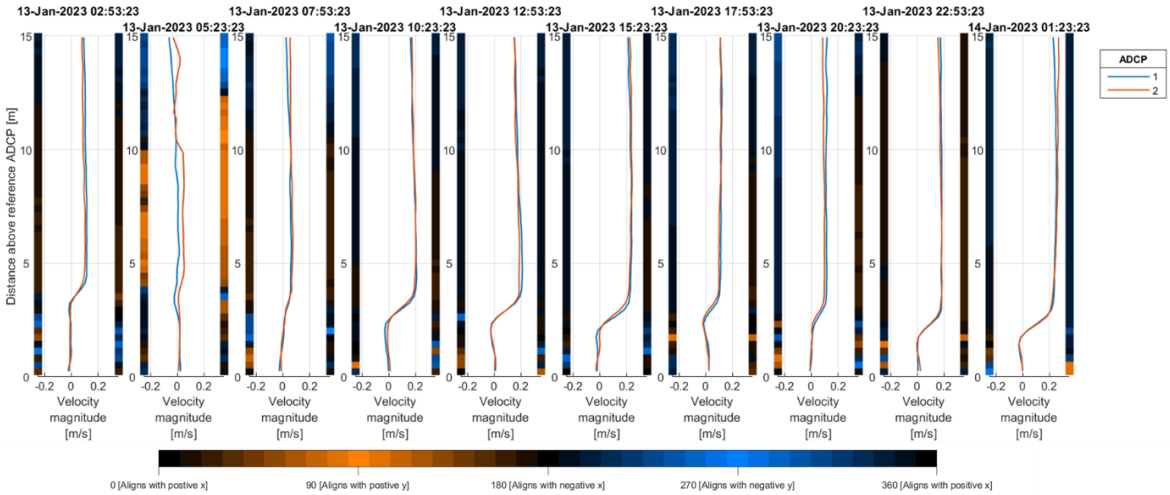

Figure 34: Profiles of velocity magnitude taken from the segment of the third flushing event of the second monitoring period that is shown in between the black vertical lines in Figure 32. The orientation of the horizontal resultant vector is indicated by the color bars on the axes for which the most left one is for ADCP-1 such that the second bar applies to ADCP-2, that use an added sign to the velocity magnitude depending upon its along x axis orientation.

The flow directionality below the density interface sets the first flushing event apart from the other times when the interface is not lowered with the above interface flood and ebb tidal cycle

Figure 35 and Figure 36 present the orientation of the horizontal velocities for the third and first event. To not provide a biased perspective through the temporal period shown in the figures, the third flushing event is divided in two portions of equal length that coincide with the temporal range of the first event. Because the color scheme stays around the extremes of 1 and -1, this indicates that the velocity resultant vectors tend to respectively align with the positive and negative along channel direction.

During the third flushing event when the positive velocity holds on from a long time above the interface, a cycle of alternating positive and negative velocities is perceivable below the interface. It thus appears that the water in the hollow moves back and forth without the interface undulating. The below interface water is first forced by the overflowing fluid in one direction to ultimately flow back as the interface stays horizontal. This notion of flow is nearly negligeable in magnitude, as can be seen in Figure 34, and probably hampers a seiche, indicated by Debler and Armfield (1997) for hollows with a lower length to depth ratio, to establish. As the depth below the interface decreases any directional patterns become more random.

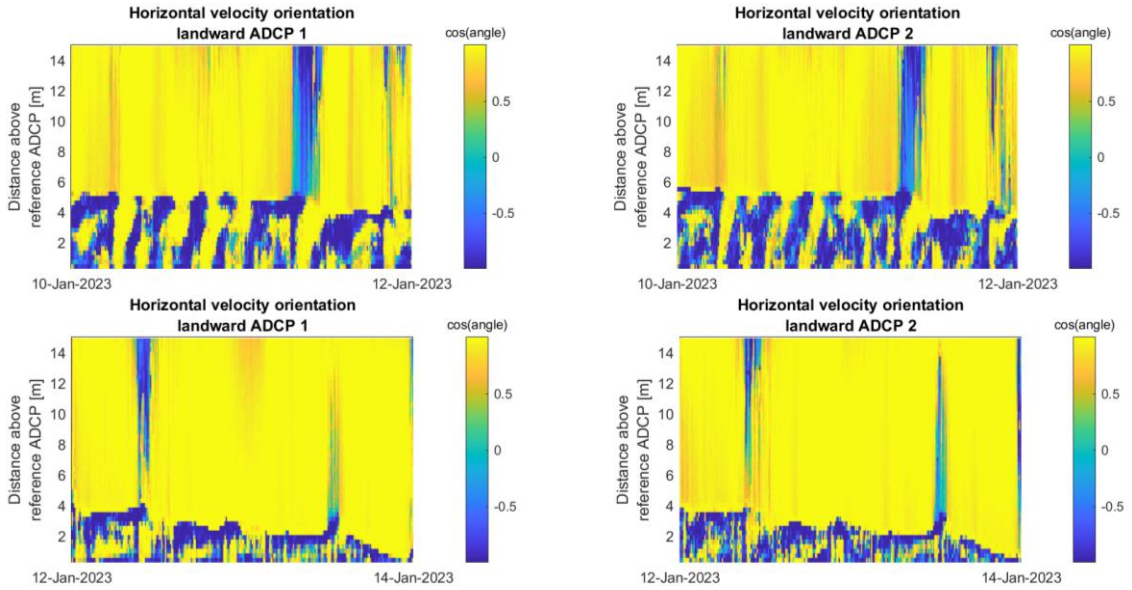

Figure 35: Horizontal velocity orientation for the third flushing event during the second monitoring period. The lower pair directly follows after the top pair of plots. The use of the cosine of the angle of the resultant velocity orientation with respect to the x axis indicates the degree of along channel alignment with a 0 insinuating lateral flow while 1 and -1 respectively indicate seaward and landward along channel flow.

The interface lowering observed during the second event is also paired with a period of towards the sea directed currents that extend beyond that what could be attributed to a single ebb event in the river influenced estuary. The same observations as made for the third event apply. However, for the remaining times in the second monitoring period, the alternating positive and negative overflowing velocities prevail with the cycles of ebb and flood. Thereby in the estuary environment the times of positively directed flow last a bit longer than the negatives at location 1. To understand why the first event stands out, the observed flow orientations are presented in Figure 36 and compared to Figure 37 that is taken from the period just after that the hollow is filled up again subsequent to the first flushing event. The overflowing velocity magnitudes for both temporal segments are strongly comparable as can be verified by considering the above depth average time series of Figure 23.

Amongst the four times of positive flows during the initial flushing event, the first one is just associated to the overflowing water flushing out the salt that is in the water column portion upward from the about 6 m level above the ADCPs for which salt water does not tend to remain accumulated for this location. Thereby the interface level becomes similar as to that shown in Figure 37 where the interface does not change over time while in Figure 36 there is the clear decrease. Comparing the two figures the one in which the interface remains constantly at 6 m, shows more systematic below interface patterns than the one reporting the first interface lowering event. Figure 36 shows especially for ADCP-1 some notion of the same systematic pattern of Figure 37 but the orientation impression is overall more confused.

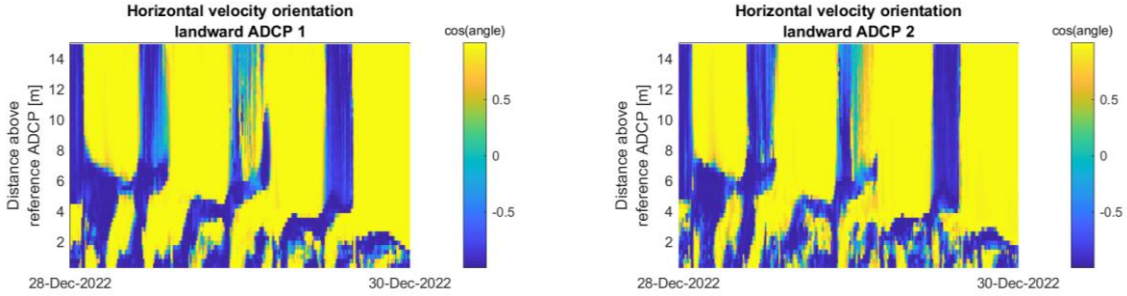

Figure 36: Horizontal velocity orientation for the first flushing event during the second monitoring period.

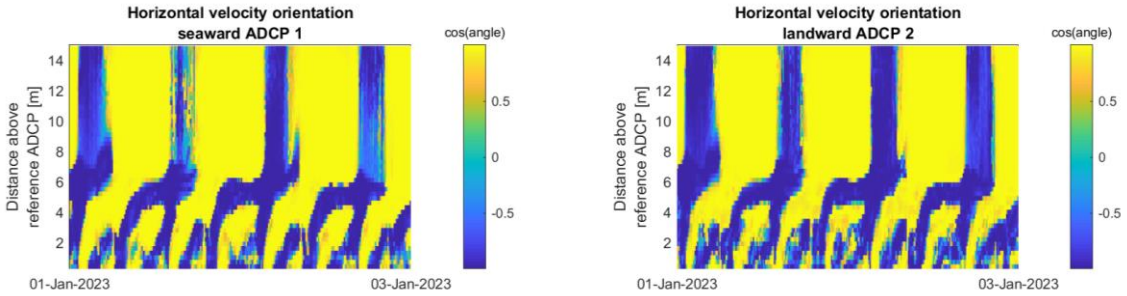

Figure 37: Horizontal velocity orientation under similar overflowing velocity conditions as the first flushing event but without interface lowering.

Below the density interface the dynamic pattern associated with the flow orientation seems to be possible when the interface is sufficiently high. While the overflowing water has an orientation that is consistent along the water column as induced by the acting forcing, the below interface pattern is more complex. Recalling the description provided in Section 2.2 regarding a wind generated circulation it can be interpreted from the velocity orientations that the water overflowing the interface induces an opposing current below the interface. However, because no interfacial tilt is observed it is unclear from where the pressure gradient would develop that allows to establish this current.

The systematic pattern observed in Figure 37 is summarized in Figure 38 as interpreted from the observed flow orientations. The only apparent difference that the dataset reveals between the interface lowering of the first event and the other times in the second monitoring period, with similar overflowing conditions, is the observed less equilibrated below interface pattern that hints at the instability of the situation. When there is flushing, it appears that the induced negative below interface current upon the establishment of the positive overflow is less pronounced such that its return flow is too. This makes pattern look less equilibrated with the positive velocities, induced by the inland directed interface overflowing forcing,

persisting more prominently as the negative ones seek to become established under the influence of the towards the sea directed current. This could be beneficial for entrainment through direct shear from the interface because the current below the density transition layer is less inclined to move the salt water in the opposite direction. However, it is all very subtle which is why in Figure 38 it is referred to as the below interface circulation becoming less clear for the positive overflowing current relative to the situation where there is no interface lowering. While it is thus speculated upon the mechanism of flushing, the dataset does not reveal what is so specific about the forcings currents at the first flushing event.

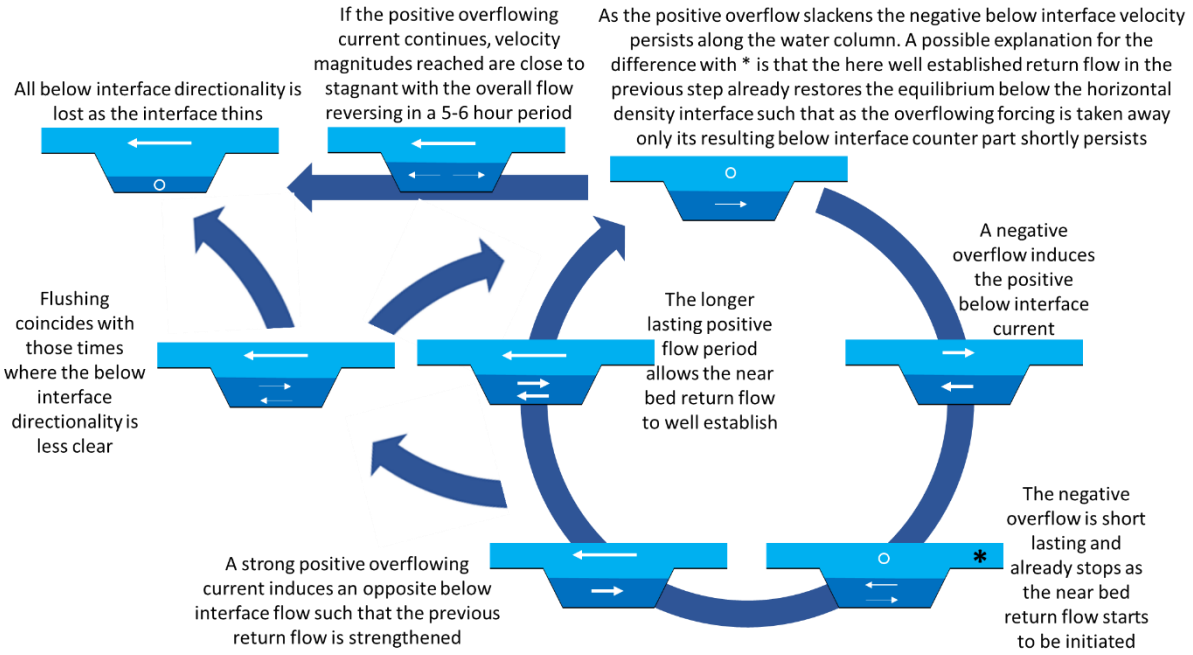

Figure 38: Idealized interpretation of the observations reported in Figure 37 regarding the cyclic patterns of below interface currents associated with the alternating above interface ebb and flood flow. The white circles indicate near stagnant water at transitioning regimes while the arrows represent the flow of the current. The only flow magnitude distinction made with the arrow length applies to how the positive overflowing currents tend to substantially exceed all others. The arow boldness suggest the prominence of how clearly the orientation flow pattern is present.

During flushing TKE is either observed at the density interface, the level that the surrounding bed starts to slope into the hollow, or not at all

In the absence of interface tilt, turbulence is the flushing mechanism discussed in Section 2.2. It is observed that turbulent mixing at the interface indeed induces the lowering of the interface level during the second and third event where the towards the sea directed velocities prevail over a period exceeding a single ebb event. To support this, Figure 39 and Figure 40 indicate different TKE conditions during the first and third flushing event. Noteworthy is that for the third flushing event there are many cases where either $\overline{u'u'}$ or $\overline{v'v'}$ is negative near the interface such that the TKE value calculated is invalid. This follows from instances where the variance in velocity along the vertical beam is relatively large compared to that along the slanted beams when considering the formulation of equations 8 and 9 that apply a factor of $-2cos^2(\theta)$ to $\overline{w'w'}$. There is still a clear peak in TKE at the interface that becomes less prominent, to fully disappear, as the interface level is lowered. When only a thin layer of salt water remains in the hollow at the end of the third event, it appears that the interface is lowered with the positive overflowing current directly and thus without turbulence. The velocity magnitudes are not in excess of those a few hours

earlier where TKE does peak at the interface. For the second flushing event, where the interface is not lowered to such levels, the TKE peak at the interface remains present. Accordingly, this event is not specifically shown due to the similarity in the conditions.

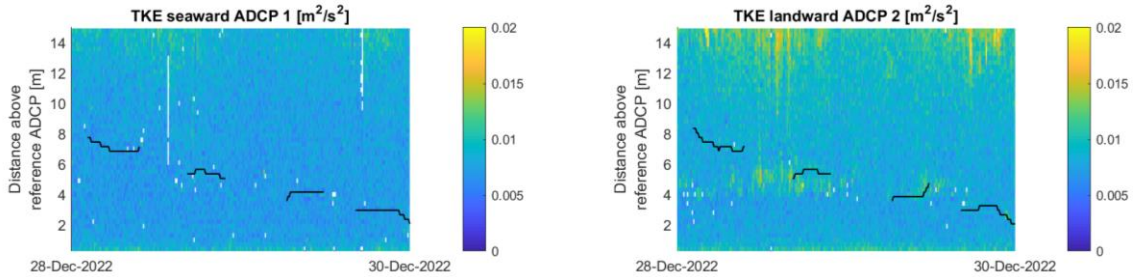

Figure 39: TKE during the first flushing event of the second monitoring period. The interface is shown with the black line and only shows those parts where it is clearly identifiable from the along channel velocity profiles.

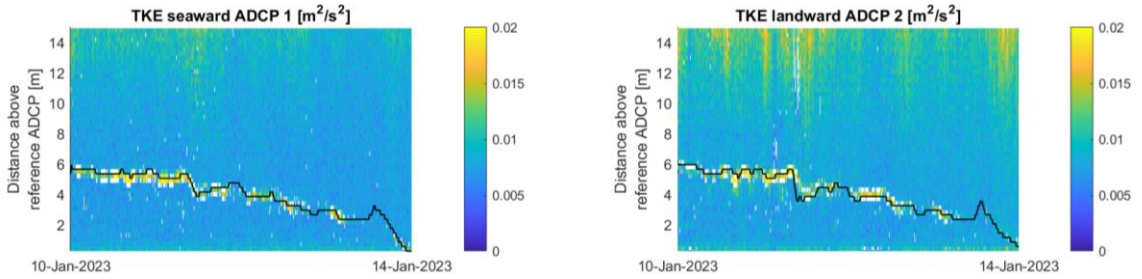

Figure 40: TKE during the third flushing event of the second monitoring period.

During the first flushing event the TKE profiles do not reveal the presence of a density interface but for ADCP-2, higher TKE values are present over a wider band in proximity to the interface delineated from the along channel velocities. The level at which this occurs does approximately stay around 5 m above the ADCP which therefore is about 1 m below the depth of the hollow relative to the surrounding bed. However, the TKE observed becomes less prominent as the interface is lowered into the hollow. As such this could link to the by Debler and Armfield (1997) stated observation that at the upstream side of the hollow a formed vortex is weakened as the interface is lowered. Thereby the vortex and interface are linked, explaining why when there is no salt water in the hollow there is also no deviation from the logarithmic velocity profile as discussed in Section 6.1. Indeed, under no condition at the end of the second monitoring period, where there is no salt accumulated, the TKE observed in Figure 39 reoccurs.

Based upon the time series of TKE profiles, the only time frame where similar TKE observations reoccur as for the first flushing event is from January the 6th at 17:00 to the 9th at 3:00. At this time there is also a density interface present as the hollow is completely filled with salt water. However the interface over this period is not lowered and accordingly is in line with the idea that this TKE does not contribute to the flushing of salt water. The in Figure 23 presented velocity conditions indicate that the associated depth average overflowing flow velocity magnitude is just about less than half those peaks observed during the first flushing event. While this could thus potentially indicate why no flushing occurs on the January 6th it does leave to question the forcing that induces the observed turbulence as there appears no direct overflowing velocity magnitude and orientation connection. Indeed for many velocity conditions, in between those prevalent at the first flush event and around January 6th, the observed turbulence around the 5 m depth is not present when there is salt water accumulated in the hollow.

Peaks in TKE at the density interface accompany gradual flushing

The gradual lowering of the density interface observed throughout most of the third flushing event links well to the times that a TKE peak is present at the density interface that reflects the turbulence that can induce mixing as resulting from the shear production and buoyant damping balance. The same applies to the second flushing event where also only gradual interface lowering is observed. Instead, at times of more rapid flushing, the TKE peak is absent as observed throughout the first event but also during the third event when the interface level gets close to a completely flushed state.

To give an overview of the times for which high TKE values are observed around the interface throughout the second monitoring period, Figure 41 is included. It shows, alongside the already made observation of higher TKE values during the second flushing event and before to throughout the start of the indicated third event, a prolonged period of high turbulence at the beginning of the monitoring period. Over this segment there is high along water column variability in velocity orientation with low velocity magnitudes. While the TKE is high throughout the water column, the TKE at the interface at the three peaks is still amongst the highest observed considering that Figure 27 only has a vertical axis up to 0.025 m^2/s^2. Thereby these, alongside the two flushing events, all coincide with periods for which the flow orientation is temporally stable. Further, the absence of interfacial lowering while the gates remain closed suggest that the prevailing velocities below 0.1 m/s are too low to entrain salt water away from the hollow while those juts exceeding this value do appear sufficient for the third flushing event.

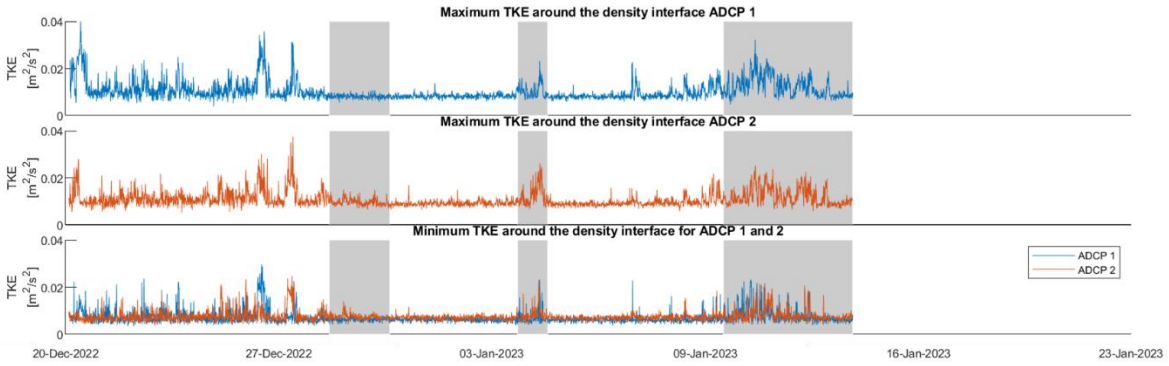

Figure 41: The maximum and minimum TKE present in the 1.5 m thick band in which the interface delineated is centered for the second monitoring period.

Despite the variations between the maximum TKE time series between the two ADCPs, reflected by the correlation coefficient of 0.45, it does uphold that the differences are not systematic. Indeed the periods of higher TKE correspond in both series while supported by the time series of the minimum TKE around the interface that draws the attention to the same periods indicating that the interfacial layer is affected. However the peaks in the minimum time series stand out less distinctively, such that it does appear that there is a point near the interface for which the value of resulting TKE is strongest and that those around it have lower values to transition into the background TKE contained in the water column.

The vertical shear in the horizontal velocity and the higher along beam velocity variances support that TKE is produced

Based upon the instrument coordinate system the elements added within the production rate equation are individually shown in the top row of Figure 42. The sum of P1 and P2 is taken to include both shear based Reynolds components. Indeed comparing P3, that is founded on the vertical based normal Reynolds

covariance, to P1 and P2 allows to notice the much more spread out scattered pattern that is present throughout the water column.

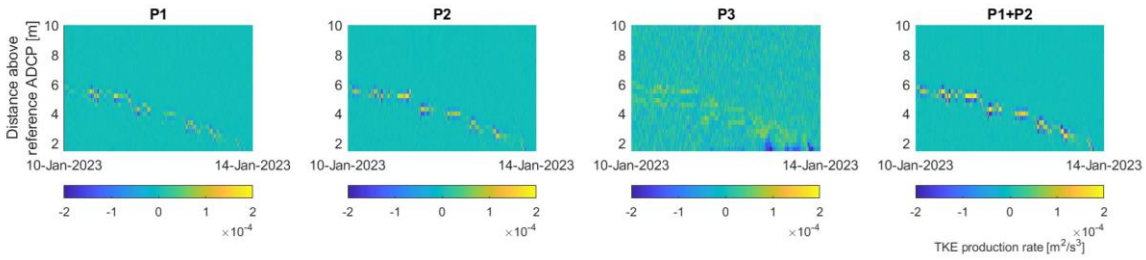

Figure 42: TKE production rate calculated at ADCP-1 during the third flushing event of the second monitoring period.

To further discuss the omission of P3 in the calculation of the TKE production rate, three profiles are selected based upon their diversity for illustrative purposes. The first is chosen for the sole dominant positive production rate peak while the second also has negatives. For the third, there is no peak in production rate. Figure 43 illustrates that $\overline{w'w'}$ is not centered around zero as are the shear Reynolds covariances. This appears to link to the already brought up idea that the apparent background variance is inherent to the acoustic sampling, referred to as the Doppler noise. Because in the calculation of the shear Reynolds covariances one along beam variance is subtracted from the associated other beam along the same instrument axis, it follows that if they both contain the same systematic error it is removed. The $\overline{w'w'}$ is instead solely based upon the vertical beam variance.

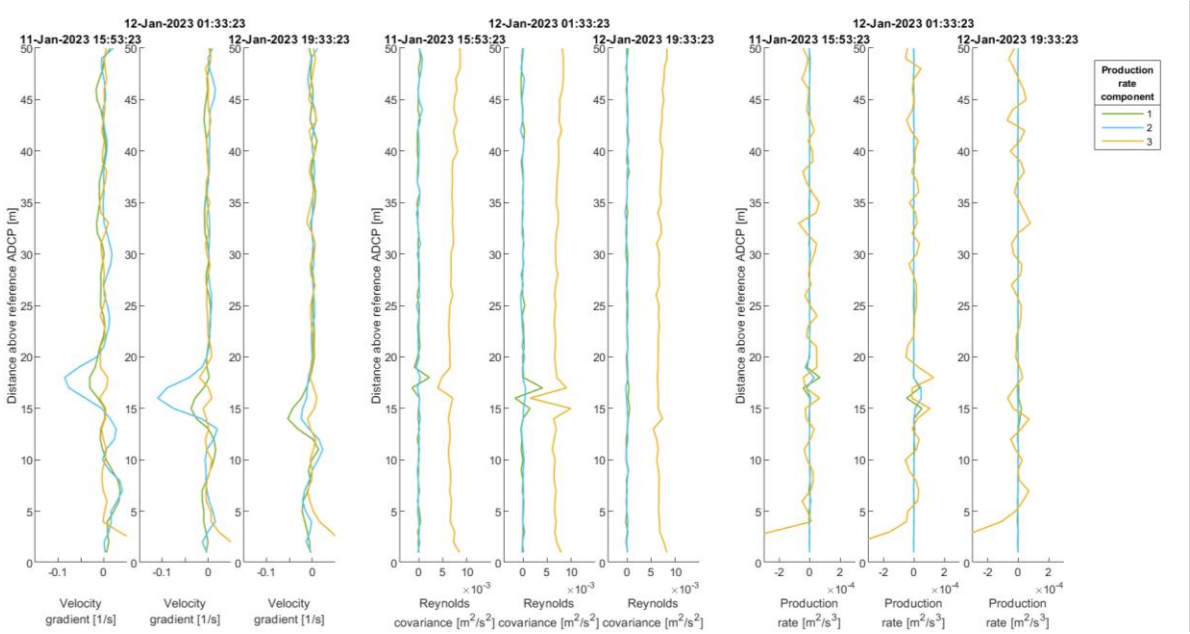

Figure 43: Selected velocity gradient, Reynolds covariance and TKE production rate profiles of the three components in the production rate formula.

Considering the product of the velocity profile gradient with the Reynolds covariance, the fluctuations of the P3 component are explained and an alternative option to handle P3 would be to remove the apparent background velocity variance. However this is not done to find the TKE production associated with vertical

shear, to which the along depth horizontal velocity gradients lend themselves, because the formulations of Stacey et al., (1998) and Simpson et al. (2004) do not mention P3 either. Indeed for P1 and P2, the higher velocity gradient at the interface, in combination with the observed variance around this level, suggests that TKE is produced. However, the production rate pattern at the time of 01:33 is questionable with the included negative values.

The TKE production rate estimate is hampered by the lack of directionality in the Reynolds covariances

The calculated negative production values do not actually resort from turbulence feeding the mean flow. Indeed, as is further discussed in Appendix 1, the concept of using the observed variance of the two opposing beams to dictate the sign of the Reynolds covariance should be put in perspective of the direction of the flow. Turbulence is produced as along the flow orientation the variance observed increases. Therefore, taking the TKE production rate as positive for the situation that this applies allows to instead produce adjusted results shown in Figure 44. The values are removed for which the variance decreases with the flow, leading to a large scatter of omitted values. It is expected that this is attributed to the relatively low flow conditions. Indeed Stacey et al. (1998) alongside Guerra and Thomson (2017) have the dominant portion of their data above 0.5 m/s, a value never reached in the depth average processed Haringvliet dataset.

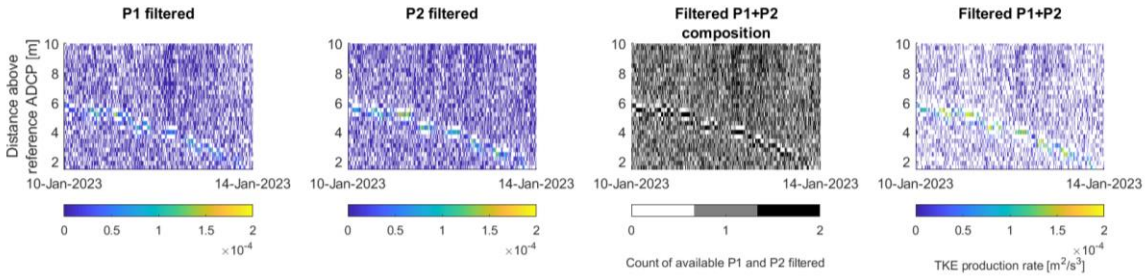

Figure 44: Adjusted production calculated at ADCP-1 during the third flushing event of the second monitoring period.

For the addition of the filtered P1 and P2, it tends to apply that only one of the two values remains available. However, because only the pair can provide the indication of the magnitude of the production rate, the combined plot of the sum is more sparsely filled. Indeed, because it is chosen to not realign the Reynolds covariances with respect to the along channel direction, it is important to look at the sum of P1 and P2 components to compare observations between ADCPs.

The higher production rates near the interface that arise for the third flushing event are also present during the not shown second event. During the first flushing event, there are also some higher production rates around the interface although less distinct. This only stems from the higher velocity gradients at those positions along the water column because the Reynolds covariances of $\overline{u'w'}$ and $\overline{v'w'}$do not feature larger values at this time where also TKE does not peak at the interface. A similar observation applies to the end of the third flushing event where the value of the Reynolds covariance is reduced around the interface while the TKE production rate is not due to the increased overflowing velocity that in turn induces a more prominent velocity gradient. This is shown in Figure 45 where further emphasis is put on the scattered directionality of the Reynolds covariance. There is a distinct pattern with the orientation as the cell centered at the interface has a sign that opposes the direction of the adjacent cells.

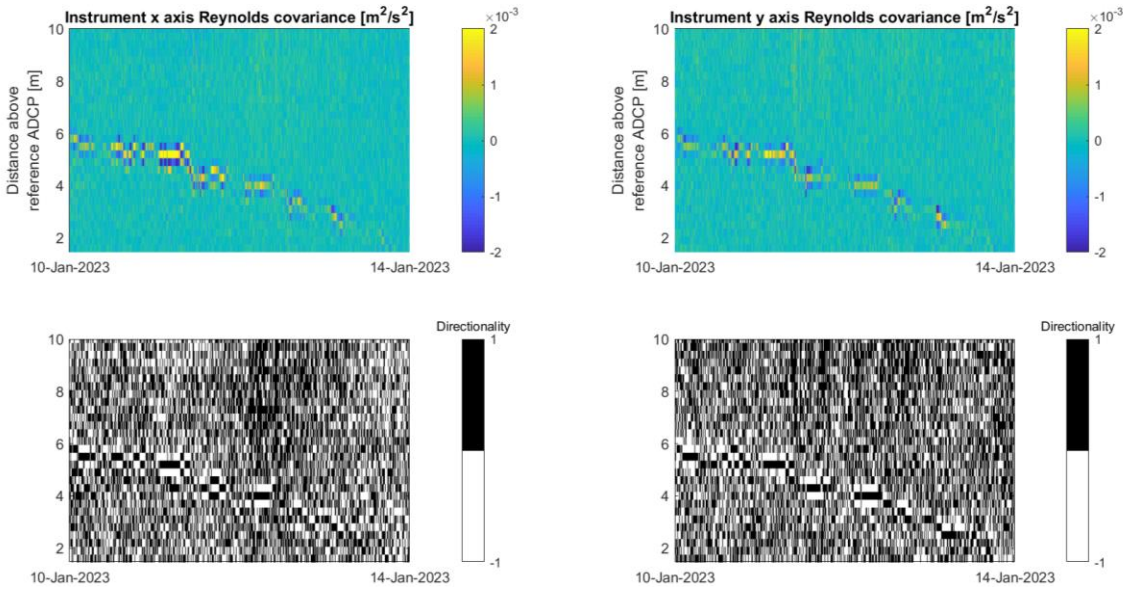

Figure 45: Shear Reynolds covariances based upon ADCP-1 for the third flushing event during the second monitoring period.

To give an illustration of the omission choices and the obtained positive production rate, Figure 46 is provided for the same profiles presented before. At the first time, around the interface there is the required opposition between the velocity and Reynolds covariance sign to produce the positive production. However, the negative Reynolds covariance based upon the instrument x component does not fit the velocity observed during the 01:33 time such that this is omitted.

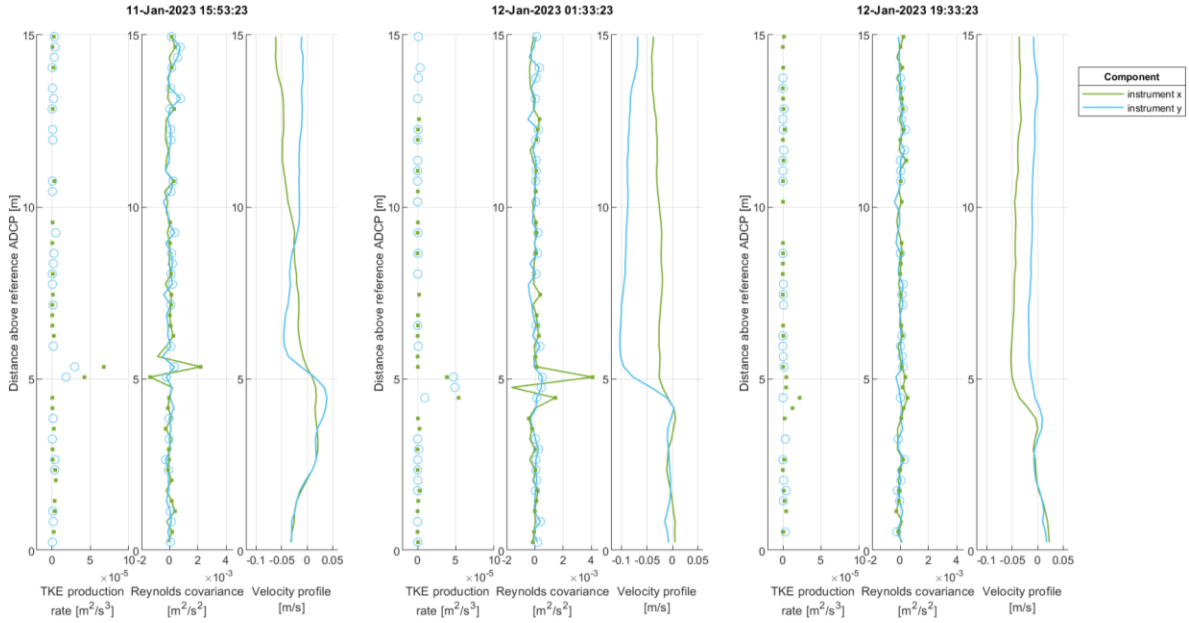

Figure 46: Shear based production rate components obtained based upon filtering out those that are unexpected from a Reynolds covariance to velocity profile relation. The instrument x component refers to the inputs for P1 while the y component to those used for P2.

Location 2, the most landwards hollow

Interface tilting accompanies the current that flushes the accumulated salt water out of the hollow

The along channel velocities are shown in Figure 47 with the delineated interface. From the difference in the interface position, it is apparent that interface lowering at the more seawards ADCP-1 only occurs with a lag to ADCP-2 such that the interface across the hollow length is expected to be tilted. The same principle applies to the not shown second flushing event that is less clearly marked because of the lower interface position and velocities. While at the quite minor first flushing event it is difficult to certify that the interface at both ADCPs started off at the same level, the interface is originally horizontal for the more major accumulation of salt water associated with the third event. Despite that the distance between the ADCPs is slightly longer than with the set up for location 1, this is not expected sufficient to lend itself better to detecting an interface tilt.

It is considered if the observed interface incline is triggered from the downstream rim of the hollow as described in Section 2.2. The outside bed starts to come into effect about 1 km seaward from ADCP-1. Using the spacing between the ADCPs of 255 m, the observed interface level difference at the two ADCPs is used to obtain an estimate of the gradient that prevails. Assuming a linear interface allows to estimate its level at the hollow rim. For the first and third event it is observed that just before the major lowering times at ADCP-1, that each event has twice as shown in Figure 47, the extrapolated position of the interface at the rim amply exceeds the surrounding bed level. The impression of an outflow surge, instead of a more steady theoretical outflow stream, is obtained. For the remaining time the extrapolated position is below the rim. The results suggest that the tilt is not necessarily induced from the downstream end but more by a movement of water in the downstream direction forced by direct shear. More exact interface positioning would be good for confirmation.

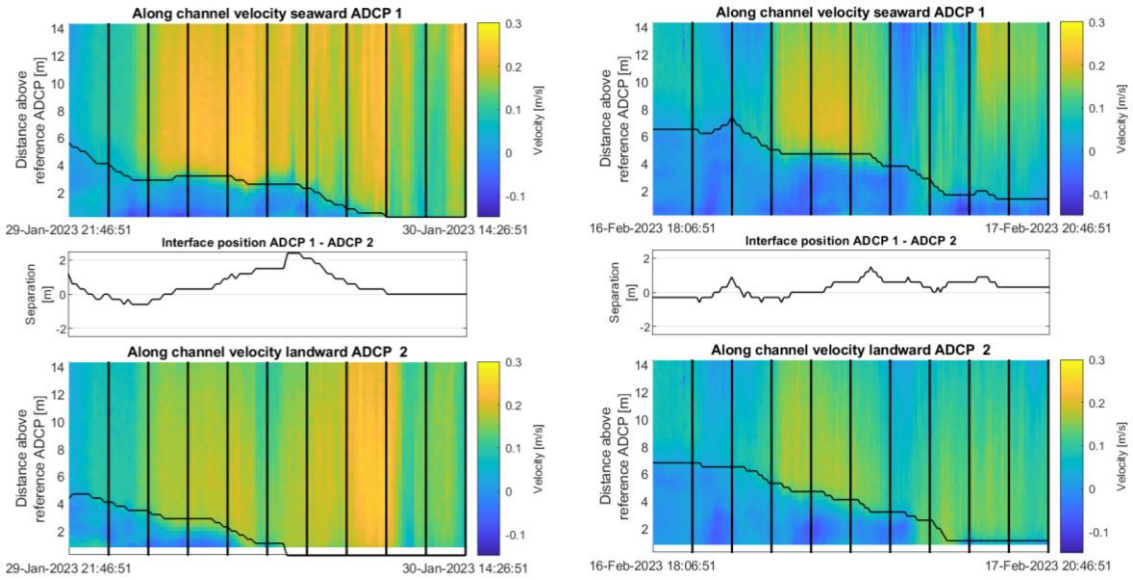

Figure 47: Along channel velocity profiles with delineated density interface for the first (shown left) and third (right) flushing event during the third monitoring period.

The observation that the interface level observed at the more landwards positioned ADCP-2 starts to drop more rapidly than at ADCP-1 is expected to follow from that this hollow is more like a channel with direct

shear just moving the salt water along in the downstream direction where its exit is to some extent restrained by the upward slopping bed out of the hollow. Further the very low accumulated salinity content in the hollow can be important as well. Indeed, the buoyancy resistance to entrainment from direct shear thereby remains relatively low and can be a major influence on the observed flushing such that differences in behavior could arise for higher salinity concentrations.

The velocity profiles confirm the observation on interfacial tilting

Of the three times that there is salt water accumulated in the hollow, the third one is used for the velocity profiles reported in Figure 48 according to the black transect lines of Figure 47. This is the event in the third monitoring period for which most salt is accumulated, leading to the highest observed interface position along the water column. It should be noted that, with ADCP-2 being positioned higher than ADCP-1, not applying a depth correction would for a horizontal interface systematically suggesting at tilt. Therefore, any claims made about the interface tilting critically depend upon the applied depth alignment strategy. There is however no indication that the depth alignment applied needs to be questioned because for the third period the depth placement retrieved independently from either the water surface level or the pressure is equivalent.

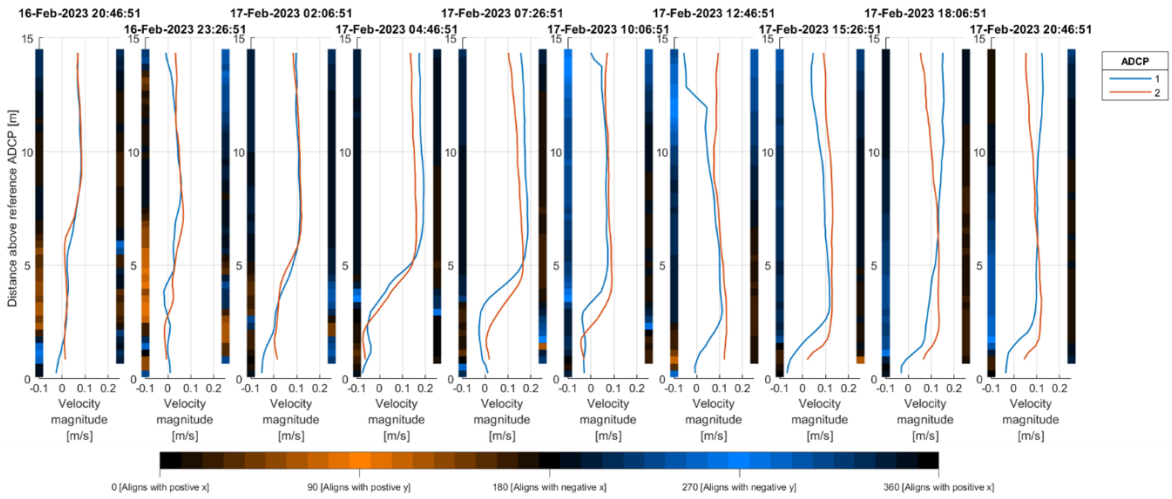

Figure 48: Profiles of velocity magnitude taken at the times, during the third flushing event of the third monitoring period, shown with the black vertical lines in Figure 47. The orientation of the horizontal resultant vector is indicated by the color bars on the axes, for which the most left one is for ADCP-1 such that the second bar applies to ADCP-2, that use an added sign to the velocity magnitude depending upon its along x axis orientation.

Noteworthy is that, as best illustrated by the 02:06 plot, a below interface current in the opposite direction as that above the interface can also develop at location 2. The interface thins quickly such that the below interface dynamics can not persist. Further, making claims about the differences in the velocity between the ADCPs is uncertain because of the non-consistency of the patterns. This was already seen when discussing the above interface velocities according to Figure 24. Indeed here again, the last two subplots of Figure 48 appear to show distinctively different profile shapes at both ADCPs under flushed conditions. However, this just applies to this single occasion where the resultant orientation of the flow approaching is slightly deviating from the along channel axis.

It is confirmed that no temporal variations in turbulence are distinguishable during flushing events

At the same times as for which the along depth velocity profiles are shown, those of the TKE are reported in Figure 49. It holds for all three flushing events that there is no noticeable increase in TKE near the interface. Indeed the about constant TKE value along depth is only increased slightly along the top part of the water column. The over time and along depth consistency emphasizes that for the vast majority of the cells the background TKE dominates the turbulence present in the flow. The depth averages of these profiles range from 0.0077 to 0.0095 m^2/s^2.

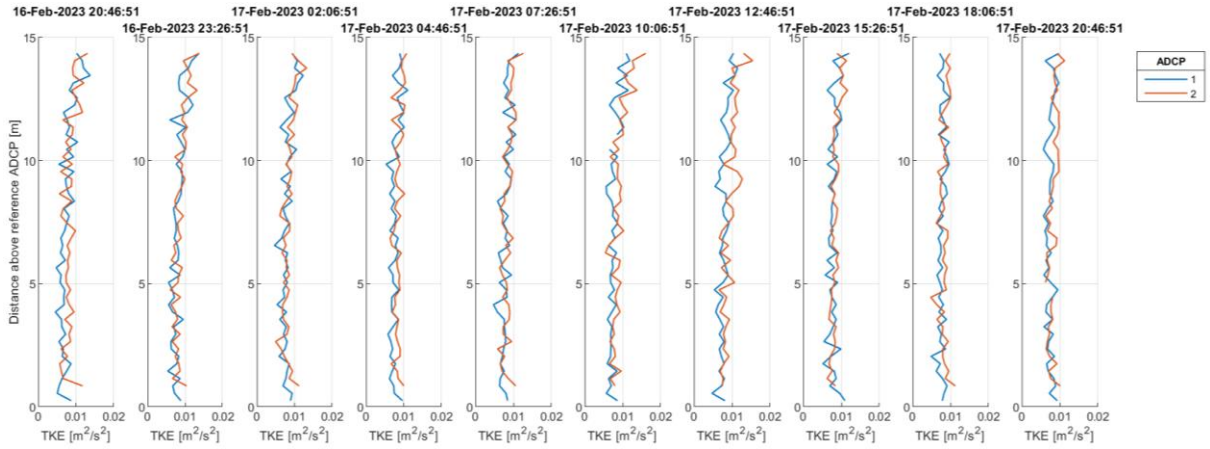

Figure 49: TKE profiles of both ADCPs during monitoring period 3 for the third flushing event

Based upon the calculation of the TKE production rate for location 1, its calculation for the flushing events in the third monitoring period is irrelevant. Considering the progression of shear Reynolds covariances shown in Figure 50, these are noticeably less distinct than those reported previously in Figure 45 that uses the same order of magnitude on the colorbar. Therefore any resulting magnitude of the production value will resort from the increased velocity gradient at the interface itself. The prevalence of vertical shear but not velocity variations, emphasizes on the direct shear inducing the observed flushing.

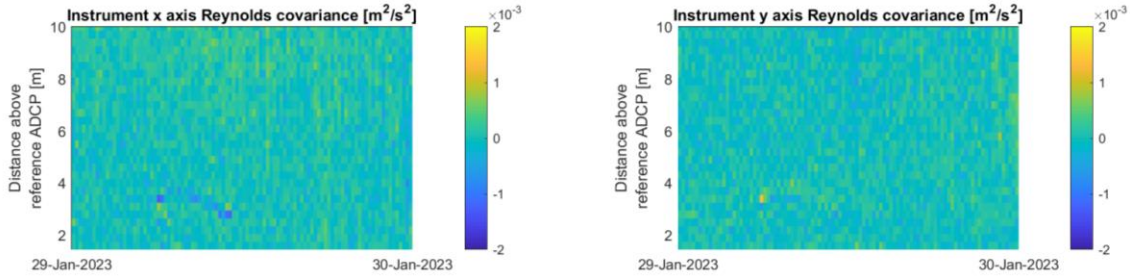

Figure 50: Shear Reynolds covariances based upon ADCP-1 for the third flushing event during the third monitoring period.

6.3. The stability of the density interface

Having identified and studied the main flushing events attention further goes out to the stability of the interface. Thereby it is of interest to focus on the full monitoring periods again to identify the times where a critical Richardson number indicates that the velocity produced shear is not resisted by the buoyancy, suggesting a potentially unstable stratification. The subsequent consideration of if interfacial waves are observed leads to the discussion if they carry into such turbulent mixing at the interface.

Richardson number

The most rapid flushing is linked to low Richardson numbers but not to turbulent interfacial layers

Figure 51 shows the critical shear Richardson numbers calculated during the second monitoring period. Noteworthy is that the critical values are not linked to the times where the TKE peak is observed at the interface. Although the in section 2.3 described theory starts off from a stable interface that becomes unstable from vertical shear in the horizontal velocities, the estuary conditions can also induce after an incoming flood tide an unsettled density stratification as indicated in Section 2.1. Thereby, both situations offer, in their own way, a gradual density transition from which salt water can be entrained such that the distinction made in Figure 52 applies that clarifies some of the terminology already used in in Section 6.2.

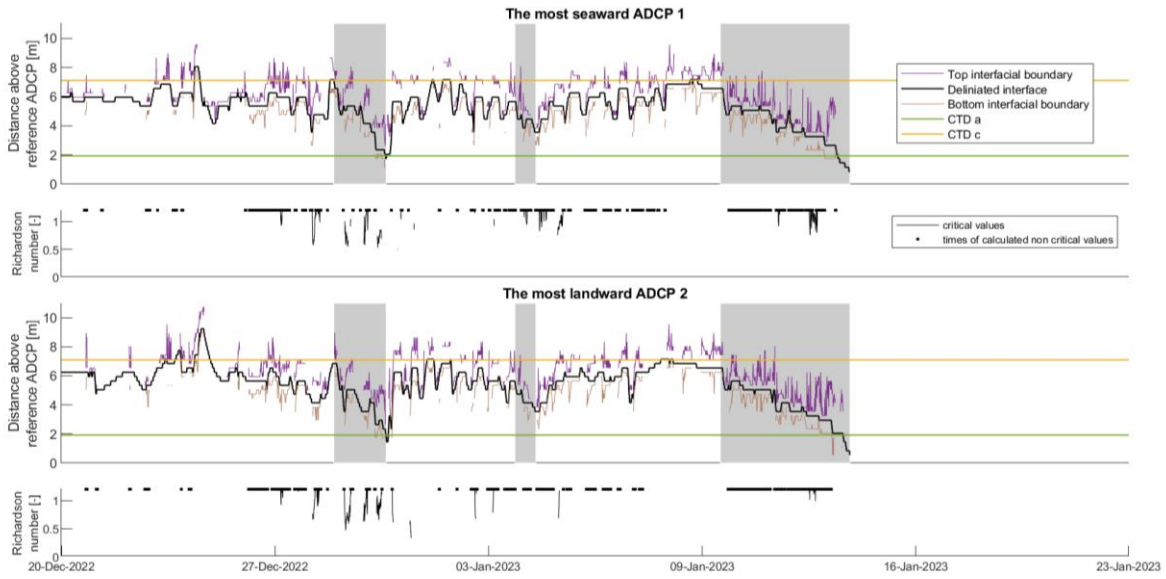

Figure 51: Estimating the Richardson number during the second monitoring period from the along channel velocities and the CTD based density time series.

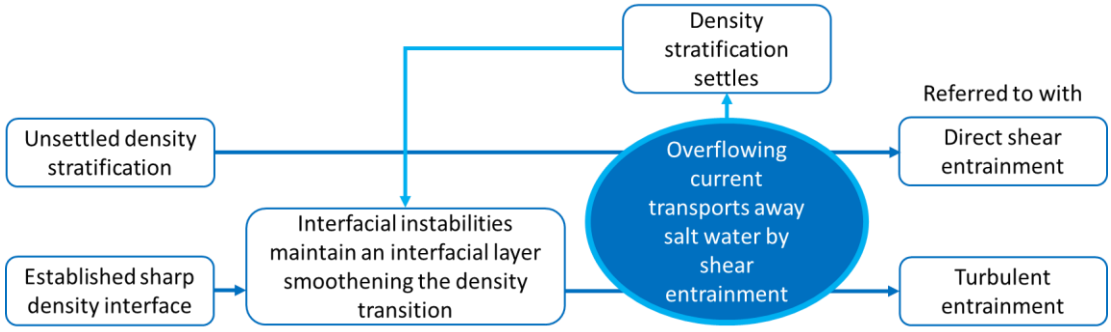

Figure 52: Distinguishing between direct shear and turbulent entrainment by considering the influence that makes the stratification unstable according to the Richardson number.

The unsettled density stratification for the first flushing event compared to a more established interfacial layer at the other two events is expected because of the much wider distance between the top and bottom interfacial boundary delineated in Figure 51. As such it follows from the shape of the velocity profiles that

the interface is more settled under the prolonged unidirectional overflow while this is not yet so for a single ebb. Thereby the calculated Richardson numbers are ineffective at illustrating the instabilities that must exist with the observed TKE peak that sustains the interfacial layer associated with the gradual flushing observed during the second and third flushing event. It is further important to note that while Figure 51 specifically shows critical Richardson numbers for the first flushing event, this does not set it apart from the other similar flow condition because just no Richardson number can be calculated for those due to the position of the CTD line relative to the interfacial boundary extent. Therefore no follow up can be given to the below interface flow orientation comments, incorporated in Section 6.2, that seek to explain why specifically the interface lowers with this first event.

The dataset provides restricted opportunities to estimate the shear Richardson number

For the first monitoring period, once the hollow is filled with saline water, the identified position of the interface lies above or around the level of the highest, along the water column positioned CTD-c. This does not allow to apply the method described in Section 5.3. When, during the period that the gates are kept closed, the interface is distinctively present between two CTDs it is the absence of sufficiently high velocities that hampers the proper demarcation of the interface shear layer thickness bounds. This is also what hinders the calculation of the Richardson number at the start of the second monitoring period. However under such low velocity gradient conditions high Richardson numbers would be expected and thus these times are not of particular interest. Indeed, it is only with the higher overflowing velocities that larger velocity gradients occur for the established density gradient.

During the third period, the time that the delineated density interface exceeds the level of the deepest positioned CTD is restricted as previously indicated in Figure 17. Further, when the interface is between the CTDs, the occurrences that not one of the interfacial bounds exceeds the only 1.95m extent between the two CTDs are even smaller. Nevertheless, it would have been interesting to compare the interface stability for this more landward hollow with that of the more seaward one. Theoretically, the lower salinity values observed during monitoring period 3 would suggest that the interface can more easily become unstable than in period 2 if exposed to the same velocity conditions. However, Section 6.2 already discussed that no apparent increased turbulence is perceived around the interface during the third monitoring period. Therefore with the observed rapid flushing that can occur at the hollow of location 2 the concept of Figure 52 appears to support the importance of the direct shear entrainment allowing to further highlight the role of the low accumulated salt concentrations to potentially facilitate the required gradual density transition even under a continuously sustained towards the sea directed current.

There is similarity in the by the salinity indicated interface thickness and that derived from the velocity profiles

Related to Figure 51, Figure 53 clarifies how the interfacial boundaries are found, comparing these to those suggested by the method of Krvavica et al. (2016) from the salinity profile. For both ADCPs the depth average velocity values are shown as straight lines in the same color as the velocity profile. These are subsequently shifted towards the interface by one time the velocity variance that applies. This allows for variable adjustment opportunities and provides a reasonable indication of what would be the portion where the velocity transitions.

Despite the noticeable difference of the delineated interface position that would be indicated by the velocity or salinity profiles, the interface width results remain in a comparable range. Based upon the strategy used by Krvavica et al. (2016) on the salinity profiles this produces for ADCP-1 and 2 respectively a width of 1.6 and 1.8 m. Instead with the here used velocity based strategy 1.2 and 1.6 m are found. It is thus respected that the value for ADCP-1 is inferior to that of ADCP-2. For the latter the difference is also smaller than the 0.3m cell size while for ADCP-1 the deviation of 0.4 m is still reasonable. However, due to the lack of verification opportunities of the applied strategy, it is relevant to conduct a sensitivity analysis on the three parameters of the formula used to estimate the Richadson number.

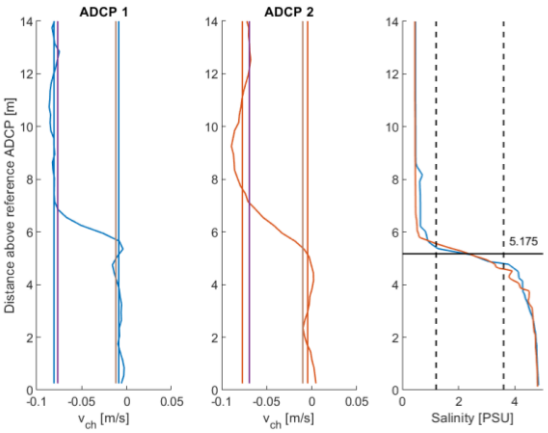

Figure 53: Comparing the shear layer width from the salinity profile taken at the start of the second monitoring period to the velocity profiles of the along channel component approximately 10 minutes after. The dashed lines in the third plot indicate the i that would be retrieved using the method of Krvavica et al. (2016). The other interfacial boundaries are colored as in Figure 51 while the above and below interface depth averages are in the color of the velocity profiles.

The Richardson number calculated is most sensitive to the velocity input but expected to be more affected by the interface thickness and density values

Following the described strategy of considering the rate of change of the shear Richardson number with respect to the inputs within the range of observed values, Figure 54 is obtained. A box drawn on the image to demarcate the range in which any observed critical values of the Richardson number occur. In comparing the rates of change of R_s with respect to each of its inputs, it is noted that the order of magnitude by which these inputs take different values is strongly divergent. Indeed, the extent of the range over which i, r and c are observed to vary are respectively 3.65 m, 0.0041 and 0.2262 m/s. Accordingly, $\frac{dR_s}{dr}$ is divided by 1000 and $\frac{dR_s}{dc}$ by 10 to obtain comparable visualizations based upon the extent over which the inputs range.

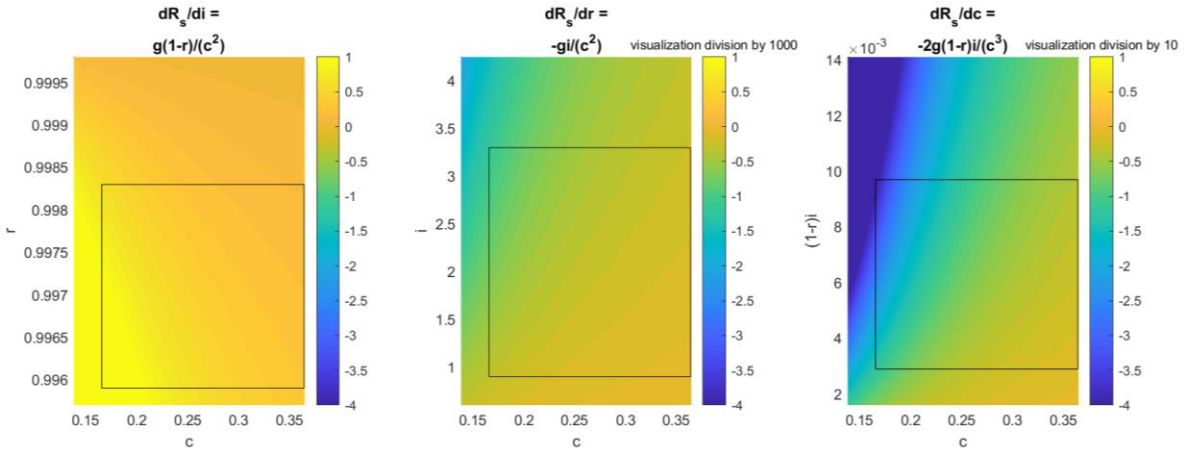

Figure 54: Rate of change of the shear Richardson number with respect to i, r and c within the frame of observed input ranges. Those values that lead to observed critical values of R_s are within the boxed region.

The variable i is the only one for which an increase leads to a higher R_s value and its result is most sensitive to changes in i for low velocity and high density gradients. The sensitivity of R_s to i appears similar to that to r which logically follows from their equivalent position in the equation. The sensitivity of R_s to r increases for higher interface thicknesses and lower velocity gradients. Similarly, the sensitivity of R_s to c increases as the stabilizing component in the numerator increases and while the velocity gradient decreases. Despite that the relative sensitivity of R_s to c tends to exceed that of the other inputs, it is expected that with the ADCP data this is also the component that can most reliably be determined.

The estimation of the gradient Richardson number following the alternative method of Kranenburg et al. (2023) acknowledges temporal changes less due to the use of a single density gradient value. However this does appear justifiable because, as illustrated by Figure 55 under the larger velocity gradients that are of interest for interface stability, the value of the density gradient input has less of an effect on the outcome. This especially for the lower density gradients. Critical Richardson numbers are also most easily attained within this range of high velocity and low density gradients, suggesting that it is likely that a proper representation of those critical values of R_g can be given with the method.

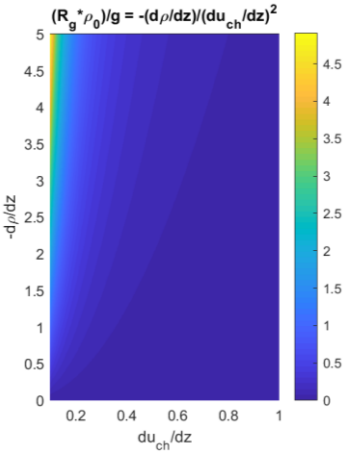

Figure 55: Sensitivity of the gradient Richardson number with respect to the density and velocity gradients.

Based upon the CTD profile taken at the start of the second monitoring period, the density gradient is approximately 2.17 kg/m^4. Based upon the time average of the two CTDs the ρ_0 of 1002 kg/m^3 is used. However, it is unclear how sharp the interface remains because based upon the echo data there is variability in the interface distinctiveness. Indeed over prolonged time periods there is not such a distinctive echo peak that comes with the strong density transition as observed with the CTD profile shown in Figure 53. Because such an echo peak is present at the time of the CTD profiles, as illustrated in Figure 19, it is expected that the density gradient values over the monitoring period are often smaller than the used input. Consulting Figure 55, this could thus for those times lead to an overestimation of the value of R_g that is further more likely because the maximum observed velocity gradients take values around 0.25 m/s^2. The degree of possible overestimation appears sufficiently large to affect if the R_g value falls within the critical range or not.

In Figure 56 the two calculated Richardson numbers are shown. The constant density gradient based Richardson number is available at each time point, with the high values found for the start of the monitoring period just not being included on the shown axis scale. It much more consistently indicates critical values than R_s. Indeed, low values of R_g are obtained each time a positively directed overflowing current establishes a strong velocity gradient. This is interpreted as suggesting the direct shear entrainment of varying quantities of salt water from the unsettled density stratification, that follows the tidal flood. It further seems relevant that Kranenburg et al. (2023) uses a critical threshold of 1 instead of the 1.2 employed by Krvavica et al. (2016) because indeed the shear Richardson number does appear to be an overestimation of the gradient one. A prominent difference with Kranenburg et al. (2023) is that their density gradient is steeper which makes it more difficult to get a critical Richardson number.

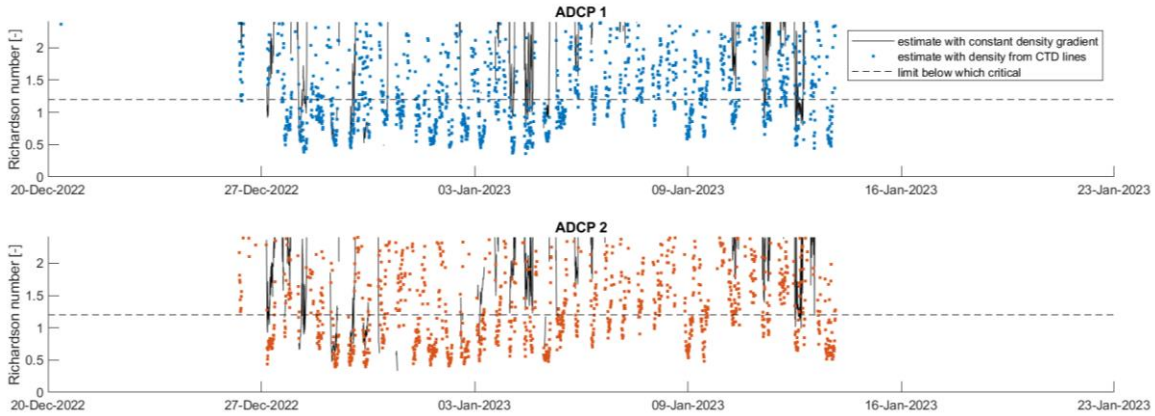

Figure 56: Comparing the calculated shear and gradient Richardson number during the second monitoring period for both ADCPs

Interfacial waves

The echo time series suggests the presence of interface instabilities with a cyclic pattern for the sharper density gradients present in the dataset

Based upon the density gradient indicated by the CTD profile collected at the start of the second monitoring period, the buoyant frequency would be 0.16 Hz which amounts to a period of 6 seconds. Therefore because the patterns of interest should exceed this periodicity, as indicated in Section 2.3, the echo data is through averaging resampled to having a value every single second to smoothen the input time series for the periodogram.

Throughout the second monitoring, period numerous short segments are identifiable over which the periodogram indicates a cyclic pattern of observed echo strength that could be linked to undulating interface behavior. Before indicating the full scale of observed times of such occurrences, two examples of processed echosounder data segments are given in Figure 57 and Figure 58 to indicate the nature of the observations made.

The first example occurs during the time that the gates are closed and where turbulence dominates the entire water column. Indeed, the depth average overflowing velocity is just 0.015 m/s. Despite that the flow orientation is quite consistently maintained over time it is unclear if such a low velocity should be expected to induce waves through shear at this time that interfacial turbulence does peak above that of the turbulent surrounding water column. The echosounder time series taken at 6.05 m above the ADCP shows, from a base echo reference, a sequence of peaks. Because the echosounder reflects the strength of a density transition it follows that it is sharper at these peaks. Because a single depth is thus considered it is only possible to look at the periodicity of this density transition sharpness returning to the specific along water column position, taking that it else is at a position above or below the one looked at. The periodogram indicates a strong peak for an oscillation with a period of 1.24 minutes. The percentage of variance associated to this sharp peak is 26.65% which is deemed an accurate representation regarding that the height and width of the main peak are used to determine this number.

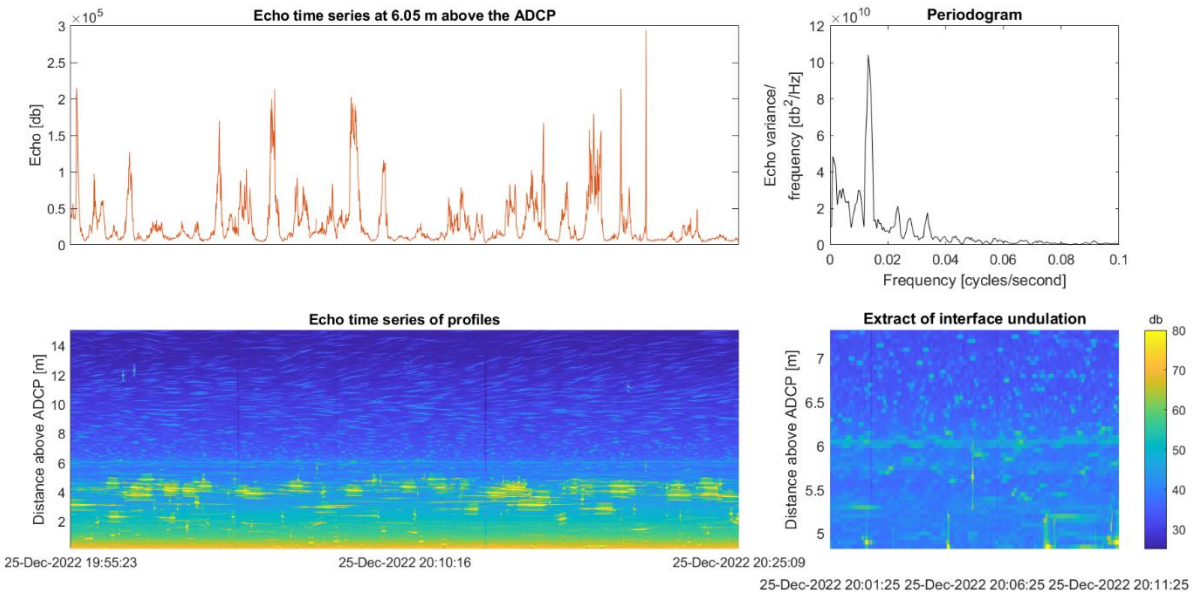

Figure 57: Example 1 of periodicity in the echosounder data of ADCP-2 during the second monitoring period

Considering the time series of echo data along depth, the interface is visible and zooming into a section confirms that the point of the peak echo around the interface does move slightly but without anything distinctively noticeable. Periodicity is not that properly visible in the echo data where around interface a scatter of larger echo values is present as throughout the water column. Instead, the pattern observed in Figure 58 is more clear. It shows one of the times with an actual undulation of the interface. The segment is taken at the time that precedes the third flushing event under a positively oriented velocity with magnitude of 0.07 m/s. This is still low, but with higher velocities it tends to be that there is no interface observable from the echo data, suggesting that the interfacial layer has a too gradual density transition induced by turbulence. Alternatively, it is also possible that the interface is not yet fully established after a tidal flood such that the absence of a sharp peak in the echo profile depends upon the context.

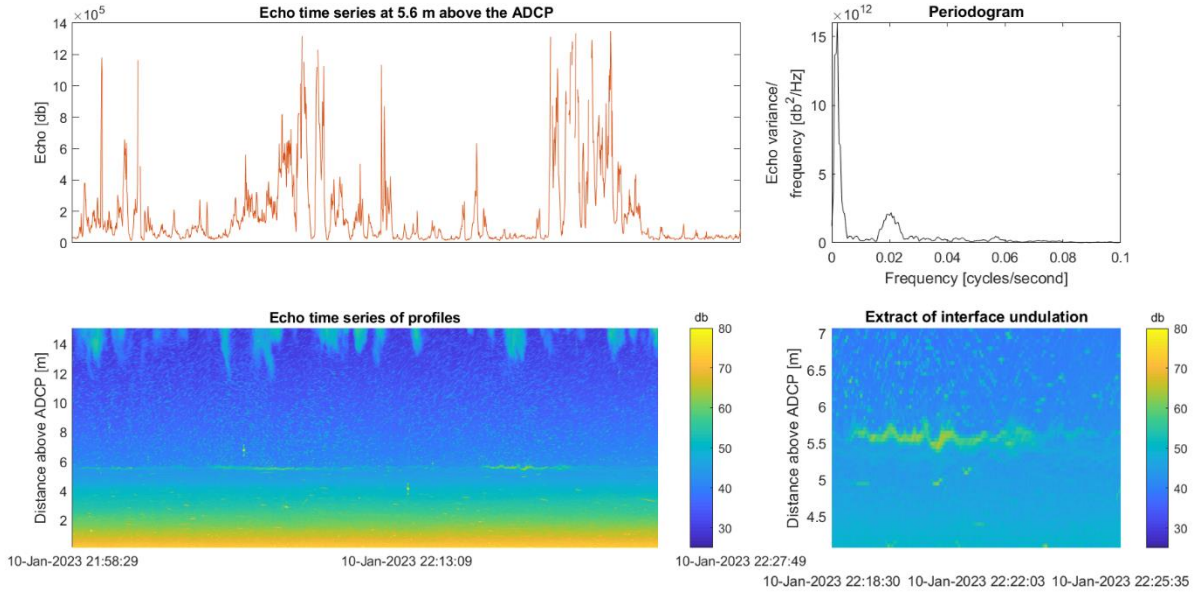

Figure 58: Example 2 of periodicity in the echosounder data of ADCP-2 during the second monitoring period

For the situation shown in Figure 58, where it appears that the overflowing velocity destabilizes the interface, the zoomed in extract shows an undulation pattern of the interface that transitions into the interface losing its distinctiveness as the density transition is smoothed. The full time series shown is composed of three such periods of which the last one, conform to the presented extract, is most clear. The highest peak suggested by the periodogram is linked to the three occurrences. The lower but still distinct wider peak is the one of interest for the interface instability. This peak suggests an oscillation period of 48 s, which is indeed the separation of the two highest points shown in the zoomed in extract around the lowest interface position observed. There is never a full symmetrically repetitive undulation or clear wave crests breaking. This thus does suggest that the instability progresses and it could be perceived as growing in size to transition into turbulence as would a Kelvin Helmholtz instability.

The periodicity obtained is confirmed by the time series of the by the echosounder indicated interface position

The more ideal way to proceed with interfacial waves analysis is to directly study the time series of the interface position. However, the application practicality of this is hampered because it would require to identify the wave containing sections very specifically. Indeed using the peak echosounder along depth position values, over the full segment length shown in Figure 58, in spectral analysis does not uncover the shown periodicity. However, specifically focusing upon the extract of the interface undulation does allow to confirm the presence of the interfacial instability. Figure 59 reveals a 46 second cyclicity which is a good match to the 48 seconds found before. The studied maximum echo intensity position time series shown is also produced by using averaging to resample the data to a 1 second temporal resolution. Accordingly the method described in Section 5.3 appears justifiable from a practicality perspective while expected to produce the periodicities of interest.

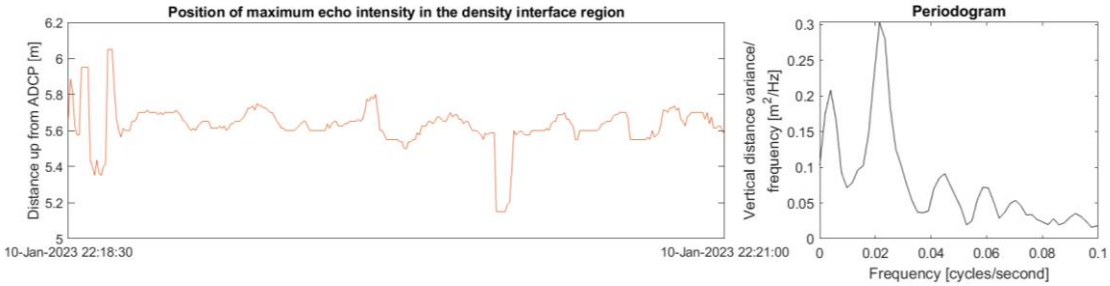

Figure 59: Produced periodogram for the time series of the maximum echosounder intensity in the region of the density interface for the extract of the interface undulation shown in Figure 58.

Interface instabilities with a cyclic pattern occurs with a distinct range of frequencies

Throughout the second monitoring period over a select portion of the occasions that the interface is distinctly visible in the echo profile time series, the applied spectral analysis allows to retrieve interface instabilities with a cyclic pattern. The timing of these observations is indicated in Figure 60 were also the periodic cycle from the spectral analysis is presented alongside the percentage of variance explained by that peak of the periodogram. Regarding the reporting of this variance, it should be noted that the longer segments tend to have a higher variance and thus are more inclined to feature a lower variance explained percentage. While comparability is therefore restricted, the variance explained is included as a rough indication to give context to the peaks that are judged to distinctively show up from the background spectrum.

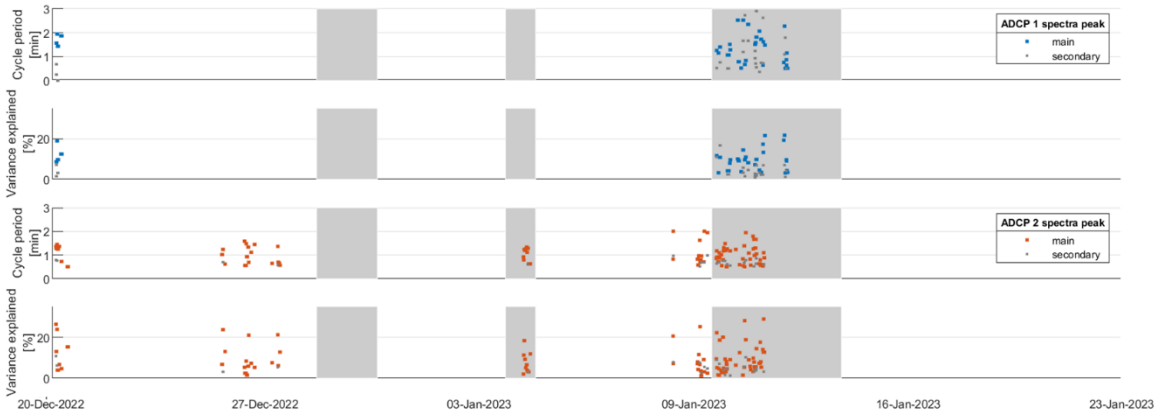

Figure 60: The period and variance explained by the dominant cyclic patterns in echo backscatter for the second monitoring period at both ADCPs.

The range of the period of the cyclicity is comparable between the clusters while not showing a systematic pattern. Indeed, For ADCP-1, the periods of the cyclicity range from 0.5 to 3 minutes while for ADCP-2 the upper limit is around 2 minutes. Despite that multiple segments are used to account for interface movement and for times that temporarily the interface becomes less clearly perceivable, the periods at which the interface instabilities with a cyclic pattern are observed are regrouped in several clusters. More are observed at ADCP-2 than ADCP-1. The velocity conditions under which these occur are variable when compared to the velocity time series of Figure 23. However, comparing Figure 60 to Figure 25, within each cluster the directionality of the flow is constant and with little variance along the water column. The actual direction of the flow does not seem relevant. Indeed, while the orientation follows the positive along channel direction for all cases, it applies for the first cluster of points after December 20th that the flow is directed inland and about 45 degrees from the main channel axis.

The theoretically expected progression from wave breaking to turbulences applies

Regarding the timing of the TKE peaks at the interface, shown in Figure 41, it can be noted that these appear to coincide with the times around which interface instabilities with a cyclic pattern are observed at ADCP-2. This holds for those near the second and third flushing event but also for the highest TKE peaks over the first portion of the monitoring period during which overall turbulence along the water column is higher. Indeed, from the theory elaborated in Section 2.3 it follows that interfacial instabilities develop towards turbulence. This applies to Figure 58 where the echo intensity less clearly peaks at the interface, to indicate its position, after the interface undulation grows and induces turbulence that smoothens the density transition. However the used method has some issues with systematically attributing all observed interfacial turbulence to interfacial waves. Indeed, during the second flushing event there are some higher TKE values at the interface prior to the observation of the interfacial waves upon which then follow still higher TKE peaks. Similarly, for the third flushing event while already a prolonged period of higher TKE values precedes the observation of interface instabilities with a cyclic pattern the highest values are only attained as these are observed.

While no further statement can be based upon the single negative oriented velocity situation associated to the interface instabilities with a cyclic pattern observed at either ADCP around the 20th of December, attention can still be directed to those observed under the positive velocities. Because around the time that the third flushing event is initiated, the interface instabilities with a cyclic pattern are first observed at the upstream ADCP-2 and then later at ADCP-1, it appears relevant to make the comment that Western et al. (1998) describe the interfacial waves forming near the upstream to propagate to the downstream while grow in size. If the waves would break and transition to turbulence this could possibly explain the more frequent observation of interface instabilities with a cyclic pattern at ADCP-2 compared to ADCP1.

The indication of the strength of the density transition by the echosounder confirms the link of the density transition with the distinction between turbulent and direct shear entrainment

The echosounder is the only indication available of the stratification degree over the full monitoring period. A peak in the echosounder data at the density interface allows to study instabilities with a cyclic pattern as shown in Figure 61. Whenever a TKE peak is present at the interface the echosounder indicates the interface position. Therefore, the interfacial layer associated with the turbulent entrainment must have a density transition still sharp enough for the echosounder to detect. Such an interface condition is only obtained after prolonged interface overflowing events with a directionality persisting beyond a single ebb event.

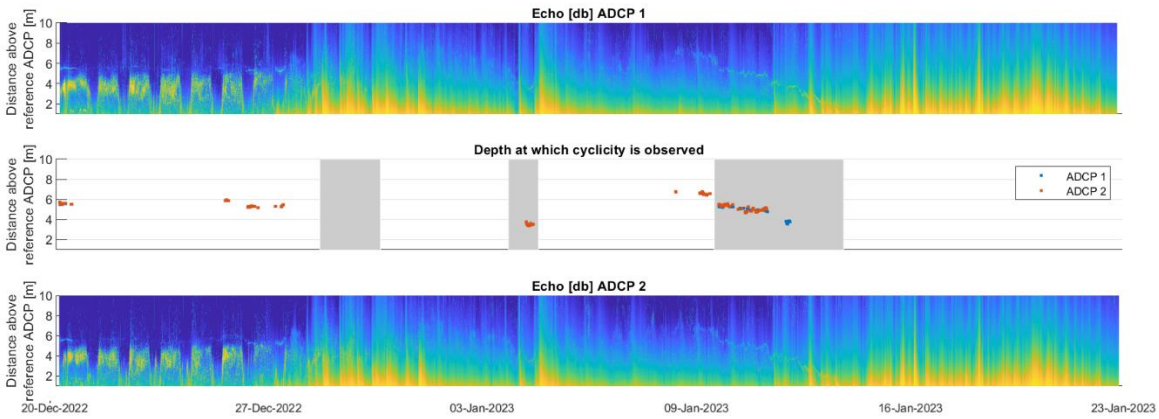

Figure 61: Time series of echo profiles for the second monitoring period with the times for which a cyclic pattern was retrieved from the spectral analysis. In the echosounder data the higher local along water column values indicate the interface position.

Figure 62 uses the stratification degree to make the distinction between turbulent and direct shear entrainment to indicate the importance of the sustained flow direction for the established interface instabilities. Accordingly, this confirms the interpretation derived from the Richardson number analyzed in Figure 52. For the salinity accumulated at location 1, the single ebb direct shear entrainment is small. To this the first flushing event is an exception because the flushing occurs without any TKE standing out around the interface that is not detectable by the echosounder. However it remains likely, connected to the understanding of the less equilibrated below interface flow commented on in Section 6.2, that it is not plain direct shear entrainment that induces the flushing associated to this unique event in the dataset.

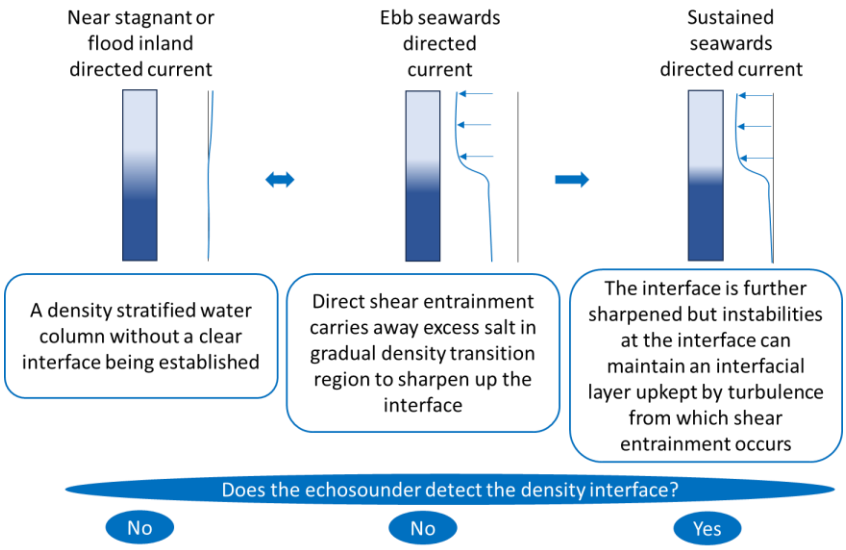

Figure 62: Interpretation of the observation of the density interface in the echosounder dataset to obtain an interface from which turbulent entrainment can occur as triggered by interfacial instabilities.

For low accumulated salinity conditions, it could apply that the initial direct shear entrainment does not sharpen up the interface but continues to act

Using the insights obtained from location 1, it is possible to propose a clarification for location 2 of which the echo dataset does not lend itself to the study of interfacial instabilities. Indeed, the lack of an observed density interface in the echo data for the third monitoring period connects to how for location 2 flushing occurs without the turbulent interfacial layer establishing under the sustained seawards flow. Because the flow velocities observed in this third monitoring period are not lower than the ones for which a TKE peak is present at the interface for monitoring period 2, at location 1, the in section 6.2 formulated possibility of the importance of the accumulated salinity to the observed flushing is emphasized and addressed in Figure 63.

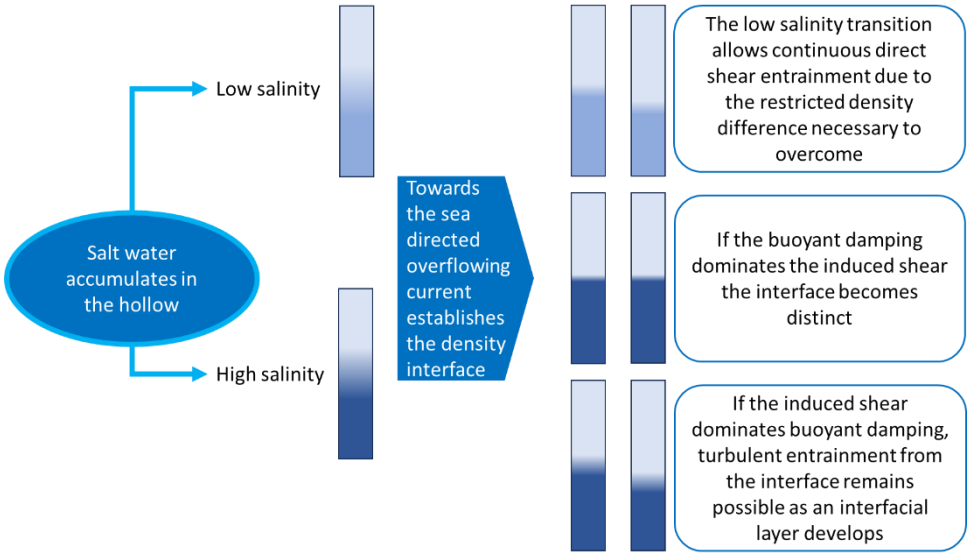

Figure 63: Interpretation of the establishment of the density interface under low and high accumulated salinity concentrations.

For an unsettled density stratification Figure 62 illustrates the initial response to an overflowing unidirectional establishing current. However, to facilitate the continued action of flushing through direct shear entrainment for location 2, it should then not sharpen the interface. The absence of a high accumulated salinity could make it possible that the stratification transition remains gradual such that the subsequent layer is just free to be affected by direct shear as well. Therefore instead of the overflowing current initially sharpening the density stratification, such that an interface is created that as it becomes unstable can be lowered through turbulent entrainment, direct shear entertainment continues to act.

6.4. Balance in turbulent kinetic energy

While the TKE production rate is calculated through a direct formula, Section 6.2 demonstrates that estimates are unreliable. This results from how the directionality of the shear between flow layers is insufficiently resolved, at the observed velocities, by the two opposing beams sampling at a certain distance apart. The estimation of TKE dissipation rate exploits only the vertical beam but in turn uses the indirect method related to the observation of the inertial subrange in the frequency spectrum of the vertical velocities. Indeed, the computation of the TKE dissipation rate relates to the vertical velocity variations $\overline{w'w'}$ which is the only of the Reynolds covariances that appears fully reliable because it is directly estimated from the along beam velocities.

TKE dissipation rate

Under high TKE at the density interface, an inertial sub range can be perceived below the interface

For the hollow at location 1, around the 11th of January 14:20, a strong TKE peak is present at the interface that is at 5.05 m above the ADCP. At this level, the calculated TKE spectrum does not feature an inertial sub range. Only when considering points further down the water column it becomes possible to observe this repartitioning of differently sized eddies along the frequency scale. A clear example is shown in Figure 64. Based upon the sampling frequency of 4 Hz, the highest frequency for which the ADCP data is reliable is the Nyquist frequency of 2 Hz. This is therefore the maximum of the periodogram that shows the inertial subrange incorporated between the 0.7 and 1.5 Hz frequency bins that about correspond with the by Guerra and Thomson (2017) reported 0.1 to 1 HZ range.

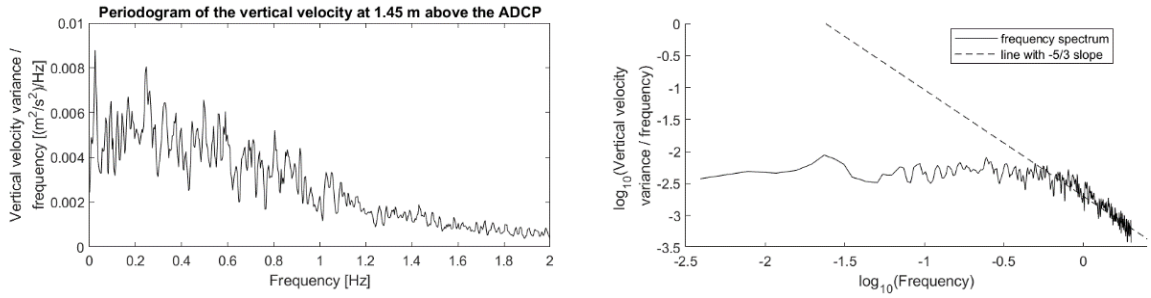

Figure 64: TKE spectrum obtained from ADCP-2 during the second monitoring period to estimate the dissipation at 14:20 on the 11th of January 2023.

Figure 65 shows the variations of the shape of the spectrum along the water column up to 5.05 m above the ADCP because those further upward along the water column do not provide additional insights. At the velocity based delineated interface and above, the turbulence is just sustained without eddies reducing in size. Indeed, it is only in the higher density water below the interface that the larger eddies, associated to

the lower frequencies, have higher variance while a lower variance value is attributed to the higher frequencies. This pattern allows to observe the inertial sub range and thus suggest that indeed turbulence energy is dissipated as eddies of different sizes are present.

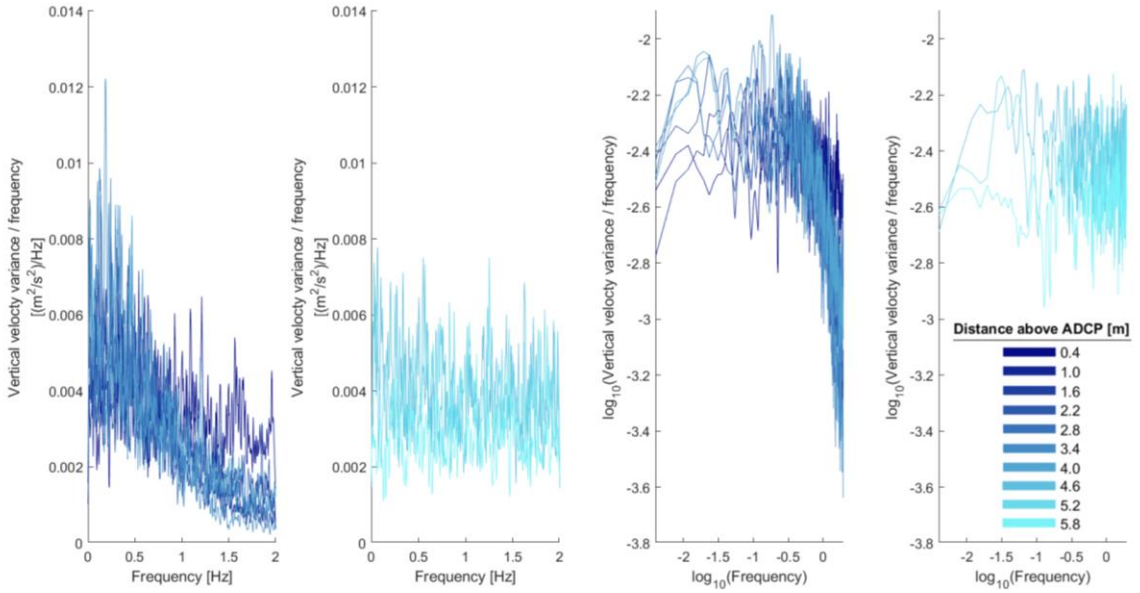

Figure 65: TKE spectrum obtained from ADCP-2 at different levels along the water column during the second monitoring period to estimate the dissipation at 14:20 on the 11th of January 2023. The spectrums obtained from the upper most reported three depth positions are shown separated from the ones for the deeper positions to emphasize upon the different shape of the spectrums.

At other times of more general high TKE, the dissipation rate can be estimated below the density interface

It is only when the time series of the TKE, shown in Figure 27 and Figure 41, suggest values above the background rate, that an estimate of the TKE dissipation rate is possible. Accordingly the period with high turbulence at the start of the second monitoring period, when the gates are kept closed, allows to calculate a dissipation rate estimate under conditions that differ from when the TKE peak is restricted to the interface.

Centered around the instance used to illustrate the interfacial instability in Figure 57, Figure 66 shows the estimated TKE dissipation rate values. These are again restricted to a region considerably below the interface, located at 6.4 m above the ADCP, despite that this time turbulence higher than the background does exist throughout the water column. Further, the TKE dissipation rate values calculated diverge from those realistic. Indeed, they take high values compared to those magnitudes previously reported for the production rate.

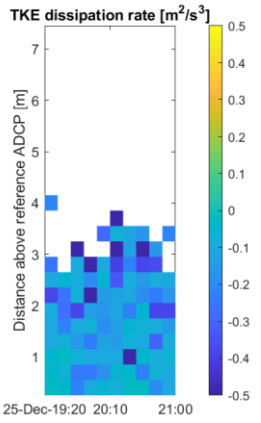

Figure 66: Estimated TKE dissipation rate at ADCP-2, shown as negative values.

In the application of the derivation of the vertical axis intercept of the log-log periodogram, as described in Section 5.4, not a single correction was required. This suggests that the method used appears to work, indicating that it can be worthwhile to deviate from this visual based verification. To do this, it would be possible to instead use a criteria of stationarity of the mean of the $\log_{10}(D|_f)$ across the frequencies to determine which spectrums are horizontal and do not feature the theoretical energy cascade.

TKE budget

The TKE production rate exceeds observed changes in the TKE

In the context of studying flushing, the balance of turbulence around times with a TKE peak at the interface are of interest. Further, the data does not offer insight into what is going on when the TKE does not stand out from its apparent background value. Therefore, Figure 67 shows a data portion centered around the instance used to illustrate the interfacial instability in Figure 58. The production rate exceeds the rate of change of observed TKE. Indeed, the turbulence at the interface is maintained around a constant level that is higher than the surroundings. This implies that for a balanced state, the TKE that is produced only partly is employed to sustain the turbulence at the interface. Because the interface persists throughout space, where similar production rates can be expected, the local balance will not be satisfied by advective horizontal transport. Indeed, the produced TKE that leaves the position is likely to also leave the position just upstream that thereby enters the position of interest. Taking that the horizontal transport of turbulence is in equilibrium it needs to be an along water column dispersion associated with a dissipation rate that allows to satisfy the TKE balance.

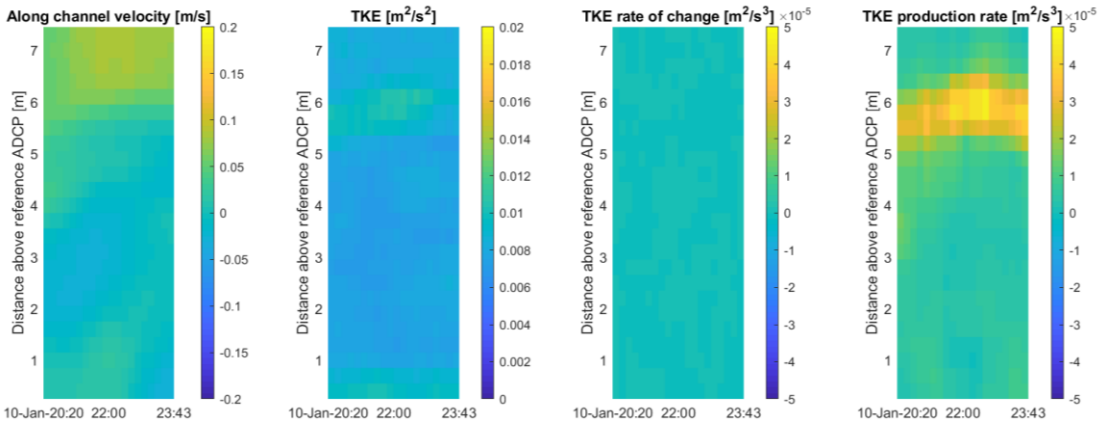

Figure 67: Comparing the TKE rate of change to the production rate over a segment of the data, with continuous TKE at the interface, from the second monitoring period when a TKE peak is present at the density interface of ADCP-2.

Figure 67 is produced by linearly interpolating over time and along depth the TKE and its production rate data to subsequently take the average from the two interpolation approaches. A 6 point moving average is applied over time for additional smoothing alongside a 3 point approach along depth. This is similar to the approach of Kranenburg et al. (2023). The TKE rate of change uses the same color scheme as the TKE production rate. Further reducing the magnitude of the colorbar range just reveals a random pattern of very small TKE changes. This however does not apply when repeating the process for the time centered around 13:50 on the 11th of January. Figure 68 shows a patch of TKE values around the interface instead of the consistently sustained turbulence present in Figure 67. Different color scheme scales, that skip between an order of magnitude, illustrate how the TKE production rate far exceeds the changes in observed TKE. The strong production rate values, as the TKE patch diminishes, are only explained by the larger velocity gradient that becomes established. The shear Reynolds covariances just show values more distant from zero along the by the velocity characterized interface compared to the surrounding. This without there being a systematic change in magnitude over time.

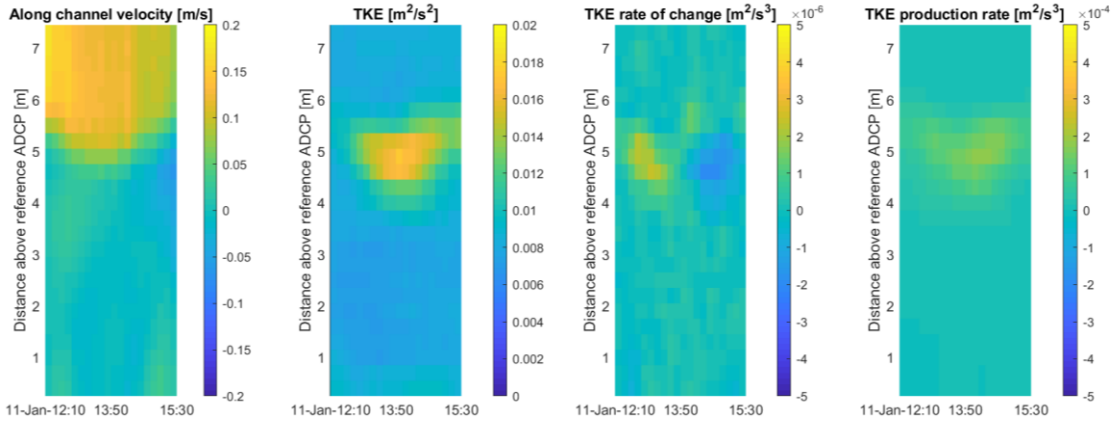

Figure 68: Comparing the TKE rate of change to the production rate over a segment of the data, with a patch of TKE at the interface, from the second monitoring period when a TKE peak is present at the density interface of ADCP-2.

Production and dissipation rates are not reliable for a TKE balance

The non interpolated production rates of a smaller segment of those presented in Figure 68 are shown in Figure 69 alongside the dissipation rates. The magnitude difference is extreme, ruling out that the dissipation rate estimates have any meaning. However also the sparsely populated, according to the logic elaborated in Section 6.3 and in Appendix 1, production rate dataset is questionable. It is more appropriate to keep a data derived analysis focused upon the direct results obtained from the ADCP. Indeed, the beam velocities and associated variances provide fundamental inputs for respectively the horizontal velocity components and TKE, without seeking to go more in depth than the instrument allows in the deployment conditions. Despite of this the already less directly obtained $\overline{u'u'}$ are $\overline{v'v'}$ are already slightly problematic for the TKE derivation near the interface due to several negatives resulting from their mathematical formulation. This does leave the along the vertical beam velocity fluctuations as the only reliable indication of turbulence. Indeed any of the made comments about the TKE in the sections 6.1-6.3 can be made based upon only using the $\overline{w'w'}$ component as well.

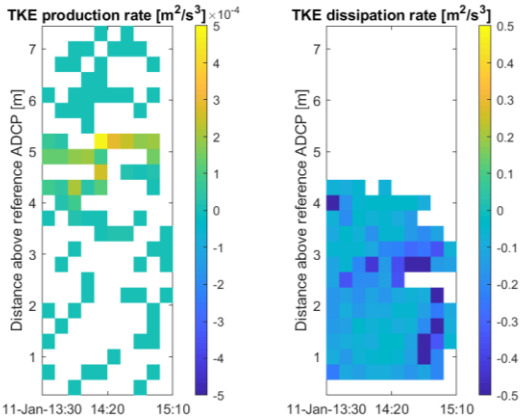

Figure 69: Estimated TKE dissipation rate, shown as negative values, and the filtered TKE production rate around 14:20 on the 11th of January 2023.

The unrealistic TKE dissipation rates stem from the high variance at low flow velocities

To explain the unrealistic dissipation values obtained it is relevant to consider with which inputs Guerra and Thomson (2017) get comparable magnitudes in their production and dissipation rates. Figure 70 shows the effect of the two variable inputs, the velocity and vertical axis intercept of the transformed spectrum, on the result of the calculated dissipation rate.

Guerra and Thomson (2017) report comparable production and dissipation rates within the range of which production is also observed for the Haringvliet dataset. This, with velocities that can reach up to 2 m/s in magnitude, with values above 1 m/s being very common. Considering that

the dissipation rate is sought to be calculated below the interface where the velocities are low it is not surprising that the maximum used velocity, in the calculation of any of the above dissipation rates, does not exceed 0.06 m/s. According to Figure 70 it is impossible to get realistic dissipation values under such conditions while the possibility increases for higher flow velocities. Guerra and Thomson (2017) observe that the inertial subrange is only visible for flow velocities exceeding 0.5 m/s. This limitation does not directly apply to the dataset of the Haringvliet because the inertial sub range is present in the spectrums. However, the velocity magnitude is still the limiting factor to find dissipation rate estimates.

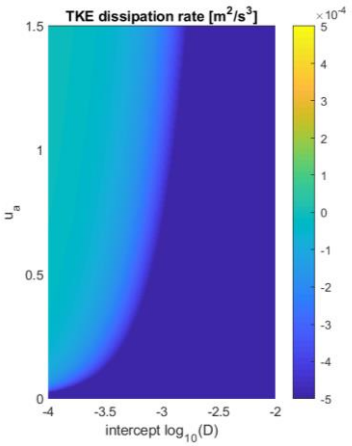

Figure 70: Sensitivity of the TKE dissipation rate to the velocity input and vertical axis intercept derived from the TKE spectrum.

Based upon the TKE spectrums reported by Guerra and Thomson (2017), it is estimated that their $\log_{10} D|_f$ intercept values range between -4 and -3. With such values it is indeed possible to obtain realistic dissipation rates in the order of magnitude between the range of 10^{-5} and 10^{-4}. From the Haringvliet dataset, the intercept values observed are in the range of -3 to -2.3. While the issue of unrealistic TKE dissipation rates thus follows from the low velocities the results from the spectrum also have a contribution. Indeed the -5/3 slope appears to be fitted to a portion of the spectrum with too high variances. Therefore it could be possible that the analyzed velocity variations are associated to too large eddies and that the portion to which the regression fit is applied does not characterize the eddies that are of similar sizes in amongst the different flows according to the Kolmogorov's hypothesis introduced in Section 2.5. Therefore potentially an increased sampling resolution, as is used by Guerra and Thomson (2017), of 8 Hz could allow to extend the periodograms. Indeed the spectrums in Figure 65 do not yet tend show the full expected spectrum that would include a more prominent trailing horizontal portion attributed to noise. Therefore an improved regression fit seems possible that produces a $\log_{10} D|_f$ intercept that is a bit lower than currently observed. However the low flow environment remains a forefront issue to estimate a realistic dissipation rate and therefore does not invite to alter a possible monitoring strategy.

7. Discussion

With the results presented and commented, an overall perspective is taken to discuss the implication of the findings alongside the limitations of the analysis.

Implications of the findings

The didactic findings on saltwater flushing can be synthesized and speculated upon with the prevalent links to established theoretical concepts

The observations derived from the available data give some insight into the way the hollow is flushed under the specific conditions monitored. How these uphold within a much larger number of flushing events with more variable conditions is to some extent indicated by what is observed.

Considering the observations obtained from location 1 in the context of the main literature based principles summarized in Figure 4, there is quite an overlap of topics. The flume experiments consider unidirectional currents. Under such conditions the data reveals, when the flood gates are kept closed, that even for low velocity magnitudes below 0.1 m/s the established interface can become unstable. As the velocity are increased close to 0.1 m/s turbulent entrainment nearly starts and indeed contributes to flushing with velocity exceeding this threshold. Further interfacial instabilities associated with turbulence are observed more at the most upstream, in hollow positioned, ADCP. Accordingly this does not contradict that instabilities grow along with the current direction if interpreted as that interfacial waves already have induced a turbulent layer at the more downstream ADCP. Further, based upon the absence of interfacial tilting, it is expected that the location 1 hollow would classify as one with steep slopes in the flume experiments. Therefore, if a saline outflow stream contributes to any flushing it could only do so when the horizontal interface is still close to the rim. Further some observations that could link with a vortex downstream of the upstream slope are apparent in the dataset when an interface is present and also support this classification as a steep sloped hollow.

With the summarized observed properties at location 1 it is from the flume experiments expected that stronger overflowing currents should increase the flushing rate observed while a salinity concentration increase can make it more difficult for interfacial instabilities to establish the layer from which the salt water can be entrained. Because with the settling of the interface direct shear is not observed to induce the interface to tilt, it is uncertain to express a hypothesis of the potential flushing of accumulated salt water with a low salinity at location 1. Without the interface tilting it could be possible that the direct shear entrainment just continuously caries away the top layer of salt water that presents itself to the overflowing water without the density gradient sharpening to stabilize the interface. Alternatively, a similar situation as observed at location 2 could apply. This is interpreted as the direct shear displacing the saltwater accumulated in the downstream direction where its exit is restrained by the upwards sloping bed. For location 1 the steeper slope would only more restrain the exit of the salt water.

There is also a split perspective on if, with higher salinity, the observed interface tilt at location 2 will persist. It could well be that the larger accumulated salinity concentration makes the observation of the interface with the echosounder possible such that the higher resolution delineation could indicate the tilt triggered from the downstream end, leading to a near model replication of Figure 4 when ignoring the vortexes of which the ADCP placements do not allow much to state about. Alternatively, it could be that the reduced influence of the direct shear upon the interface establishment also does not anymore induce the interface tilt with only turbulent entrainment becoming important.

The dataset does not allow to address the formulated speculations that are included with the purpose to emphasize upon the scope of understanding that is still out of reach after analyzing the dataset. To confirm the expected importance of turbulent entrainment for higher accumulated salt water in the hollow, the dataset of Kranenburg et al. (2023) could be useful. For location 2, it provides the sought after higher density case. Using the ADCP to estimate the TKE can indicate if interfacial turbulence is observed. However, their single ADCP set up does not allow to make statements on the interface tilt.

The salinity concentration in the hollow can be important to dictate the flow conditions that allow to flush out accumulated salt water

In the dataset it is observed that flushing at location 2 immediately occurs with the return of a sufficient overflowing current while the timing of flushing is more complex at location 1. As already commented on, despite that the hollow geometry is likely to have a dominant role, the salinity involved is expected to have an influence as well. The dataset itself does not allow to investigate the influence of different salinity values of the accumulated water in the hollow, however, returning to the observations reported by Kranenburg et al. (2023), it does apply that the flushing of the accumulated water at location 2 with a salinity of 17 to 22 PSU in 2019 is more difficult than the up to 1 PSU observed in 2023. Indeed, with the largest accumulated saltwater quantity in the available dataset, the flushing only takes 26 hours with velocities peaking between 0.1 and 0.2 m/s. Instead, Kranenburg et al. (2023) observe that about 30 days are required with near continuous towards the sea directed velocities that at each ebb flood gate discharge event peaks around 0.2 m/s to induce gradual flushing. There are even some more rapid interface lowering times when the velocity peaks up to 0.4 m/s. The apparently higher flow velocities required to induce the flushing appear to provide support for the speculation that indeed turbulence entrainment becomes an important flushing mechanism for the location as direct shear entrainment can only establish the density interface that is potentially tilted.

The effect of wind on flushing remains uncertain when considering the type of freshwater overflow that the observed flushing events require

The potential of flushing accumulated salt water out to the sea is highly dependent upon the upstream freshwater availability. It is observed that a sustained towards the sea directed velocity is necessary to obtain the turbulent entrainment at location 1 and direct shear entertainment coupled to the interface tilting at location 2. It is necessary to have incoming fresh water in the estuary that keeps the current somewhat going during the flood tide while during the ebb tide much fresh water is lost to the sea as the gates are opened. At location 1, it takes nearly 4 complete days with an average overflowing velocity of 0.11 m/s to flush the hollow filled with salt water that has a salinity starting just over 4 PSU. Instead, location 2 requires 27 hours with an average velocity of 0.10 m/s to flush the 1 PSU of accumulated salt through two salt water outflow surges of which the main is linked to velocities peaking at 0.18 m/s.

It is not only the sustained towards the sea directed currents that can require a considerable upstream freshwater water availability. Indeed, the estimated discharges to the sea during the first and third flushing event at location 1 are quite similar. This to flush, or at least nearly in the case of event 1, the between 4 and 5 PSU of salinity observed by the CTD positioned below the density interface. The turbulent entrainment that acts during the third event uses much lower velocities than the first event for which periods of inland directed velocity break up the ebb related strong velocities that peak around 0.3 m/s. In turn, the third event is twice as long as the first. It is estimated that for both the first and third flushing events about the same discharge to the sea applies.

While not having induced an observed lowering of the interface, it is still relevant to note that the effect from wind induced currents cannot be ruled out as also pointed out by Kranenburg et al. (2023). Indeed, during the period that the gates are kept closed, there is a single occasion where inland directed velocities nearly up to 0.1 m/s are reached in the layer above the interface. At that time, the salinity at the upper CTD position appears to be slightly disturbed, suggesting that turbulence is acting. This is confirmed by the calculated TKE. The timing coincides with the highest observed wind velocity peak that occurs during the period that the flood gates are kept closed. The possibility of turbulent entrainment to occur already at quite low, ebb induced, velocity peaks just in excess of the 0.1m/s during the third flushing event does suggest that wind driven currents could also prompt an interfacial layer to form from which salt water can be carried away. Kranenburg et al. (2023) doubt that wind driven currents can induce this interfacial turbulence and focus more on the interface incline that can follow from a wind driven circulation.

Some speculations set in the context of the observations and the claims of Kranenburg et al. (2023) are proposed despite that the data available to support them is not available. Regardless of the mechanism associated to wind induced flushing, it can be questioned to what degree the wind forcing can induce currents with a sufficiently consistent directionality over the duration necessary to cause complete flushing. Indeed considering that the between 5 and 10 m/s wind speed induces the mentioned near 0.1 m/s inland directed velocities, it is likely that around January 12th it would be possible for the 10 to 15 m/s wind speeds to induce the current values for which some entertainment is observed in the dataset. In the observations this is however masked by the dominance of the flood gate discharges on the observed currents. Nevertheless, if the wind forcing manages to just trigger flushing it can take considerable time to remove all accumulated salt water when considering the duration of the observed flushing events. In this time frame conditions are likely to change but some partial flushing could thus potentially occur.

The impact of by wind flushed out salt water in a low river discharge period like the summer needs to be considered too. Low accumulated salinities that are expected to be relatively easy to flush probably have little impact on the overall estuarine salinity. If indeed the required strength and duration of the forcing current increases with the concentration of accumulated salt water, it is suggested that the salt water reserves in the hollow that can affect the estuary salinity probably are unlikely to be flushed by wind.

For the 2023 year it is expected that were salt to remain accumulated at the end of the monitoring period, then the spring seasons still offers sufficient flushing potential

Each of the six observed occasions of major interface lowering are triggered by along channel currents. While the flood gate management regime dictates the magnitude of the currents, the limiting factor involved is the upstream freshwater availability. Because the fundamental reason to allow some saltwater inflow into the estuary is to favor the process of fish migration, not only the winter should be considered. Indeed, depending upon the fish species expected at the Haringvliet, the time of migration differs such that a vast part of the year is concerned (Reeze, 2016).

Consulting the flood gate discharge time series shown in Figure 71 it is revealed that several other inflow events were allowed by Rijkswaterstaat in April up into the middle of May for the 2023 year. Considering where the flushing is induced during the winter those later occurring periods would also be expected to allow to flush any accumulated salt water. However, no prolonged saltwater storage in the hollows is observed to develop beyond the monitoring period based upon the salinity time series of Rijkswaterstaat (n.d.-a) at the locations of the hollow around the available depths that are in the range studied.

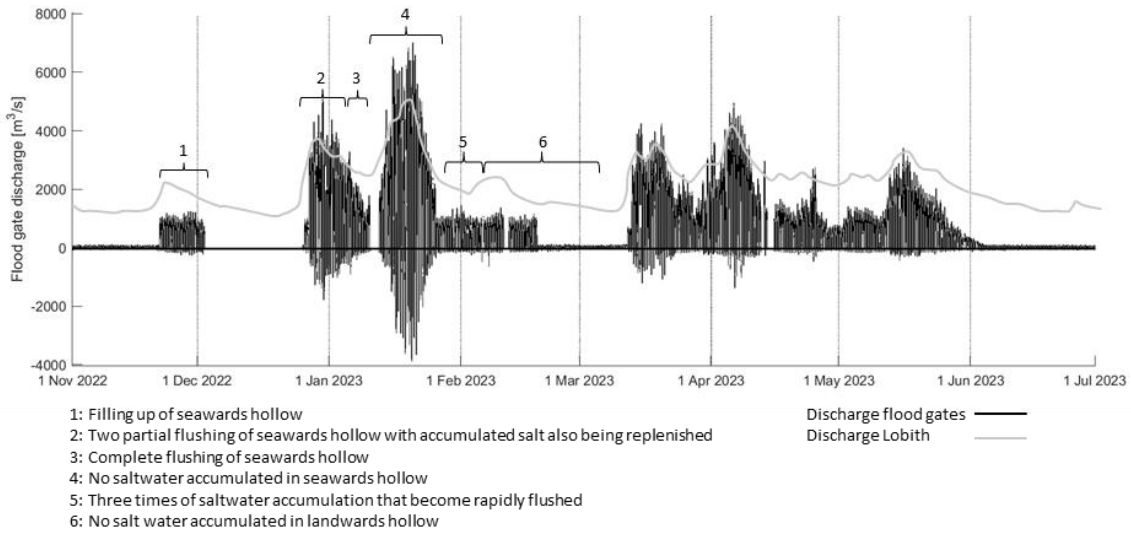

Figure 71: Discharge through the Haringvliet flood gate. Adapted from Rijkswaterstaat. (n.d.-a) and annotated based upon the observations available across the three monitoring periods.

Despite that the observed saltwater accumulations are not major anymore during the spring, it is expected that if they were it would be possible to have flushing before June starts. This is because of the similarity between the flood gate discharge from the middle of March to the 1st of April and the portion labeled with 2 and 3 in the studied period. For a similar reason the discharge past the middle of May are also expected to lend themselves to flushing. However, the observed discharges are only possible because of those available from the Rijn as indicated by the discharge values observed at Lobith.

There are flow regimes possible that prevent salt water from being accumulated

If an understanding of the flow conditions can be developed that avoid salt water to remain in hollows, this is valuable to dictate flood gate management choices. Despite that the data analysis is targeted at flushing mechanisms, some evident observations can be made about the saltwater accumulation to demonstrate the relevance of further addressing the topic.

Focus is on location 1 because the salinity values involved are greatest. The most striking example of no saltwater accumulating, despite the inland directed velocity during flood tide conditions, is obtained from segment 4 of Figure 71. Comparing this to segment 1, during which salt water does accumulate, is done in Figure 72. The first plot indicates that as the salt water starts to accumulate the dominant overflowing velocity is still positive while only near the bed there is a strong inland directed current. Instead in the bottom plot the stronger incoming discharge establishes a negative

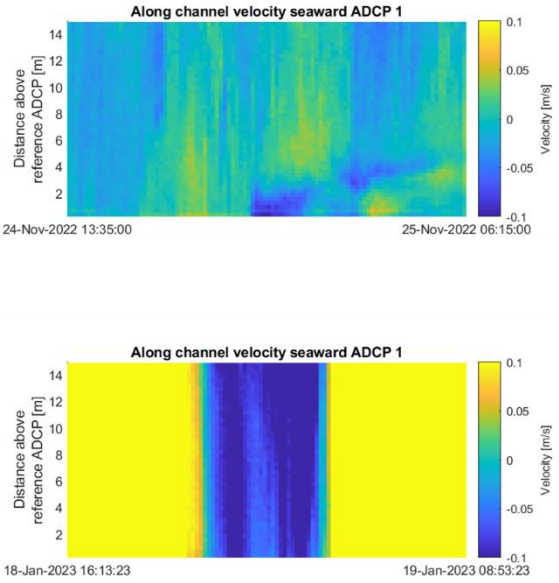

Figure 72: Along channel horizontal velocity component at location 1 from ADCP-1 during a time where saltwater starts to accumulate and where it does not.

along channel velocity throughout the water column while the salinity at the CTDs does not increase. When the filling of the hollow is initiated at segment 1 an initial low salinity increase is observed at the deepest CTD. Larger values only build up as multiple of the near bed negative flow streams are brought to the hollow. The salt that sinks down, due to its density, increases the concentration according to what the overflowing low velocity does not carry back to the sea.

The theory elaborated in Section 2.1 offers some insight to explain the observations. Indeed, during segment 1 of Figure 71, salt water is let in but with so low discharges that it is not expected that under the prevalent fresh water availability it moves itself upstream. However, combining the inflow with the possible action of a density current flow, schematically illustrated in Figure 3, could induce the near bed incoming current that conserves a part of its slightly higher, but also already diluted, salinity as presented in Section 6.1 with Figure 15. This interpretation founded explanation is somewhat analogous to the situation of a natural estuary during ebb, with the presence of salt water and the overflowing fresh water inducing the stratification. Instead during the stronger incoming saltwater discharges during segment 4, the current generated by the inflow is much larger, and the situation appears analogous to that of a flood. Mixing takes place, and with the overall fresh water being dominant there is no observed salinity increase along the water column at the hollow. Because of this, as the positively directed current takes the advantage again, no stratification is established.

Limitations of the analysis

The state of the echosounder records restricted attention for variation in stratification profile shape

The main research question mentions variation in the vertical stratification across the water column. According to the set sub research questions this takes the form of considering the interface position. Thereby focus is on the presence of the density stratification that induces velocity differences along the water column. For practicality the interface delineation is based upon these velocity profiles.

The echosounder profiles were expected to provide an indication of the distinctiveness of the density transition. This could only be used to a very limited extent in the form of distinguishing between the times that the echosounder peaks at the density interface or not during the first and second monitoring period. The density difference induced by the salt water accumulated in the more landward hollow during the second period is not sufficient to noticeably affect the echo profile, despite being enough to trigger differences in velocity. Would the dataset have been free of unexpected variations, a wider peak would have indicated a more gradual transition than a narrower and stronger one. Inherently the echo backscatter intensity decreases away from the instrument for a homogeneous water column. Clearing the echosounder data of this decrease could then have allowed to more intuitively compare the profiles indicative of the density gradient present.

While salinity induces density difference, using the echo data in the study of suspended sediment or plankton is more promising. Indeed, Gostiaux and Van Haren (2010) indicate the possibility to connect the echo profiles to those types of datasets. To relate the echo data to an actual physical quantity, it is necessary to have instruments to calibrate the relation of this association (Gostiaux & Van Haren, 2010). Potentially this could work for salinity as well if the associated density alteration is sufficient. Based upon preliminary testing using the CTD and echo data, such efforts are not relevant for the available data.

Turbulence is dominated by a background value not fully explained by Doppler noise

When considering the depth averaged TKE in Figure 27 and Figure 41, it appears that a consistent background along beam velocity variance induces the constant lower TKE threshold, set around 0.0075 m^2/s^2, above which only occasionally values occur. This average value is representative of the water column and thus is not affected by near surface turbulence. Considering that each along beam velocity variance is composed partly of noise it applies for beam b that $\overline{b'^2_{reported}} = \overline{b'^2_{actual}} + \overline{b'^2_{noise}}$. Thereby $\overline{b'^2_{noise}}$ is the Doppler noise component. Using this in the equations for the normal Reynolds covariances allows to rewrite the equation for the reported TKE into the sum of its actual value and the noise component as shown in equation 23.

$$TKE_{reported} = TKE_{actual} + TKE_{noise} = \frac{1}{2}\left(\overline{u'^2} + \overline{v'^2} + \overline{w'^2}\right) + \left(\frac{2-2\cos^2(\theta)}{\sin(\theta)} + 1\right)\overline{b'^2_{noise}} \quad (23)$$

Would the reported 0.0075 m^2/s^2 TKE value be attributable to the Doppler noise, constant amongst the beams, then this would take a value of 0.004 m^2/s^2. Guerra and Thomson (2017) claim that, for the Signature 1000, the horizontal level of the frequency spectrum associated to the along beam vertical velocity fluctuations is at 0.0001 and 0.0002 $m^2s^{-2}Hz^{-1}$ when respectively sampling at 16 Hz and 8 Hz. Both lead to the same value of 0.0008 m^2/s^2 of Doppler noise when multiplied with their Nyquist frequencies respectively to find the area under the spectrum. Accordingly the 0.004 m^2/s^2 derived from the TKE appears too large to consist of noise inherent to the acoustic sampling only. Instead, the value of 0.0012 m^2/s^2 is more realistic and results from the 0.00062 $m^2s^{-2}Hz^{-1}$ obtained from averaging over the last 100 frequency bins, that indeed show a horizontal pattern, in the periodogram displayed in Figure 64. While this thus exceeds the potentially fostered expectation of a 0.0004 $m^2s^{-2}Hz^{-1}$ value when a 4 Hz sampling rate is used, it is lower than the variance observed for most spectrums without the inertial subrange. This suggests that the steady TKE value observed is in a large part true to its presence, with the turbulence just not decaying into the inertial subrange.

While the noise could have been removed according to the suggestion of Greene et al. (2015) by subtracting it from the along beam variance this is not used. Indeed, just being aware of the variance value and its implications is appropriate in the context where an additional steady background value appears to be the potential limiting component for the study of turbulence. This is confirmed by actually implementing the proportion of Greene et al. (2015) through subtracting the 0.0012 m^2/s^2 value from each of the along beam velocity fluctuations $\overline{b'^2}$ of each beam. Thereby, as expected, the TKE values are just slightly lowered with the main patterns observed naturally persisting. The TKE production rates are not affected as already explained in section 6.2. Finaly for the TKE dissipation rate, shifting the periodogram line downwards by the 0.00062 $m^2s^{-2}Hz^{-1}$ amount does allow to obtain better $\log_{10}(D|_f)$ values. However, the derived dissipation rates remain unrealistic due to the low velocity environment.

Insight into the general applicability of the observed phenomenon is limited in the dynamic conditions across the monitoring periods for a single winter

The diversity of the velocity conditions during the monitoring periods is advantageous to see variations in responses, to indicate how under the observed accumulated salinities flushing can be initiated. The monitored winter does not allow to get confirmation on how generally the observations apply for the location. Indeed, the main interface lowering events discussed for location 1 occur under different conditions. While the turbulence related entrainment could be expected based upon the flume experiments discussed in Section 2.2 and is observed across two events, there is no support for the mechanism associated with the first flushing event. The dataset only allows to note the more

disequilibrated below interface dynamics of which the lack of another similar observation gives no confirmation. Instead, the flushing pattern observed at location 2 is consistent across the three events involved. Because the monitoring period only comprises low accumulated saltwater concentrations it could well be that the observations would differ if higher salinities were involved.

8. Conclusion

The study of the flow dynamics during the observed flushing events incorporated within the dataset, collected between November 2022 and March 2023 across two bathymetric hollows of the Haringvliet estuary, allows to answer the main research question. Despite that the echosounder profiles only have a mere contribution to the understanding of variations in the vertical stratification over the hollow, the study of the available density data and stratification interface position did provide insight into the role of velocity and turbulent energy on flushing out salt water accumulated in hollows.

At both locations the presence of accumulated salt water affects the velocity profiles, reducing the magnitude and altering the orientation below the interface while above it the flow conditions subject to external forcings directly are strongly correlated to those observed just upstream of the hollow. The vertical stratification influences the TKE that can be detected to a more limited extent. When the density gradient is sufficiently high such that it can be picked up by the echosounder, a TKE peak is present at the interface. This occurs for interface overflowing conditions that maintain their directionality beyond that of just a single ebb event when the accumulated salinity concentration is sufficiently high to not be flushed by direct shear entrainment. Thereby the interfacial layer, from which turbulent entrainment, occurs features a higher density gradient than that applicable after the ebb outwash that follows an observed controlled tidal flood. However, the study of turbulence beyond the observation of its influence on increasing the variability of ADCP along beam velocity variances is not suitable under the low velocity conditions prevalent in the dataset.

At the hollow that is closest to the sea, salt water with a salinity up to around 5 PSU accumulates. Over a period that the flood gates are kept closed, observed wind induced currents are insufficient to induce flushing. However these should not be ruled out because an event sustaining inland directed velocities around 0.1 m/s does induce some perturbation in the salinity time series collected closest to the density interface. Of the three flushing events available, the first occurs while the interface overflowing current is alternatingly directed landwards and seawards according to the tidal cycle. This tidally dominated overflowing pattern also prevails when the interface is not lowered. The only found property that appears typical to the interfacial lowering observed is that the flow orientation pattern below the interface appears less equilibrated. The two other flushing events occur at the only times that seawards directed velocities are sustained such that interfacial instabilities maintain an interfacial layer from which the overflowing shear can continue to entrain the salt water from. The velocities therefore required are very variable and certainly do not need to be amongst the strongest observed in the dataset, suggesting that the 0.1 m/s value mentioned in relation to the near wind induced event is close to inducing turbulent entrainment.

The response to the currents overflowing the density interface differs between the two hollows addressed. This is attributed to the bathymetry alongside the concentration of the accumulated salinity. Indeed at the hollow that is furthest from the sea there is no TKE peak in the region of the density transition. Nevertheless, the elongated hollow is rapidly flushed from the accumulated salinity concentrations up to 1 PSU upon the establishment of an overflowing seawards directed velocity with velocity magnitudes exceeding 0.1 m/s. The interface tilts during the three flushing events available for study. This is attributed to direct shear just moving the salt water along in the downstream direction where its exit is to some extent restrained by the upward slopping bed out of the hollow. Thereby it is interpreted that the low accumulated saltwater concentration allows that the top denser fluid layer is transported away without the need for turbulence to smoothen the transition first.

9. Recommendations

Additional work and resources are necessary to further improve the understanding of the flushing of salt water accumulated in hollows. Some areas to focus upon can be suggested based upon the results obtained with the available data.

CTD profiles

Of the three occasions that CTD profiles are collected at the ADCPs, only one pair shows the density interface. Vertical profiles of the salinity are useful to understand the stability of the interface, in the context of the derived TKE, to distinguish between the importance of direct shear and turbulent entrainment. While Kranenburg et al. (2023) indicate for their study of location 2 quite constant density gradients, under various accumulated salt water concentrations between 17 and 22 PSU, it is expected that for lower salinities, as reported in Section 6, it can be insightful to obtain an impression of variations in the sharpness of the density transition. The echosounder data suggests that there are differences present in the dataset while the instrument is insufficient to properly take record of those. Therefore it is recommended to support ADCP datasets with CTD profiles. It is judged relevant to potentially prioritize profiles to the constant deployment of a CTD instrument at a single depth. Indeed, the usefulness of those observations are strongly dependent upon the interface position.

The flushing dependency on accumulated salinity

While the previous suggestion would allow to improve the study of the flushing event dependency on the accumulated salinity with field data, flume experiments could potentially be useful too. Indeed, the observations that stem from the small scales described in section 2.2 already provided valuable insights to interpret the ADCP observations. Therefore there is potential to consider studies that investigate how the known important mechanism of flushing contribute to removing various salinity levels of salt. This could allow to further discuss the importance of not letting the saltwater concentration build up. Debler and Armfiled (1997) do use different salinity values in their experiments but do not comment on induced differences. Indeed, their use of simultaneous changes in the geometry do not allow to focus on the salinity itself.

Near the bed CTD on the seaward side of the hollow

With the studied data collection set up in the Haringvliet estuary, it can not be confirmed if salt water actually approaches the hollow near the bed with an incoming flood tide. Therefore a CTD placed on the seawards side of the hollow is proposed for such data collection schemes. The information from the CTD could improve the understanding of the condition under which salt water accumulates. Further if a saline outflow stream establishes at the exit of the hollow this could potentially also be revealed by a CTD placed as proposed.

Flushing occurring with alternating current orientation

While the previous comment could have provided an additional source of information to possibly identify a justification for the observed first flushing event of the second monitoring period, the actual obtained understanding of this event is very limited. Small scale experiments targeted at the effect, on the accumulated salt, of a dominant current overflowing the hollow with an intermittent oppositely directed one are deemed relevant. This even if the inland directed currents observed during the flood times of the

tidal cycle during the first flushing event distinguish themselves, from those when there is no flushing, by not bringing in new salt water. Indeed the experiments could potentially indicate how it occurs that higher interfacial turbulence values are attained at the interface under a unidirectional forcing current compared to those present during a single ebb tide where the ADCP data makes the flushing look like a direct shear entrainment case. Thereby it would be interesting to see if the below interface dynamics have a role. However potentially this is a behavior of which the observation lends itself better to large scales. Therefore a wider diversity of large scale studies can also contribute to the understanding of the response of the accumulated salt water to a non sustained forcing current direction.

References

American meteorological society. (2012, February 20). *Taylor's hypothesis*. Glossary of Meteorology. Retrieved December 28, 2023, from https://glossary.ametsoc.org/wiki/Taylor%27s_hypothesis#:~:text=An%20assumption%20that%20advection%20contributed,Taylor%20%22frozen%20turbulence%22%20hypothesis.

Aupoix, B., Blaisdell, G. A., Reynolds, W. C., & Zeman, O. (1990). Modeling the turbulent kinetic energy equation for compressible, homogeneous turbulence. http://web.stanford.edu/group/ctr/Summer/SP90/11_Aupoix.pdf

Balakrishnan, A. V., & Mazumdar, R. R. (2011). On powers of Gaussian white noise. *IEEE Transactions on Information Theory*, *57*(11), 7629–7634. https://doi.org/10.1109/tit.2011.2158062

Bender, L. C., & DiMarco, S. F. (2009). *Quality control and analysis of acoustic Doppler current profiler data collected on offshore platforms of the gulf of Mexico*. U.S. Department of the Interior. https://cdn.ioos.noaa.gov/media/2017/12/qc_analysis_acoustic_Doppler_current_profiler_data.pdf

Blaise, S., & Deleersnijder, É. (2008). Improving the parameterisation of horizontal density gradient in one-dimensional water column models for estuarine circulation. *Ocean Science*, *4*(4), 239–246. https://doi.org/10.5194/os-4-239-2008

Buitenhuis, Y., & Dieperink, C. (2019). Governance conditions for successful ecological restoration of estuaries: lessons from the Dutch Haringvliet case. *Journal of Environmental Planning and Management*, *62*(11), 1990–2009. https://doi.org/10.1080/09640568.2018.1529556

Cheng, P., & Valle-Levinson, A. (2009). Spatial variations of flow structure over estuarine hollows. *Continental Shelf Research*, *29*(7), 927–937. https://doi.org/10.1016/j.csr.2009.01.011

Davies, A. G., & Brown. (2007). Field measurement and modelling of scour pit dynamics in a sandy estuary. *Coastal Sediments '07*.

Davis, J. C. (2002). *Statistics and data analysis in Geology* (3rd ed.). Wiley. ISBN 9780471172758

Debler, W. R., & Armfield, S. (1997). The purging of saline water from rectangular and trapezoidal cavities by an overflow of turbulent sweet water. *Journal of Hydraulic Research*, *35*(1), 43–62. https://doi.org/10.1080/00221689709498643

De Serio, F., & Mossa, M. (2014). Analysis of mean velocity and turbulence measurements with ADCPs. *Advances in Water Resources*, *81*, 172–185. https://doi.org/10.1016/j.advwatres.2014.11.006

Dewey, R., & Stringer, S. (2007). Reynolds stresses and turbulent kinetic energy estimates from various ADCP beam configurations: Theory. https://doi.org/10.13140/RG.2.1.1042.8002

Fugate, D., & Jose, F. (2019). Forces in an estuary: tides, freshwater, and friction. *Oceanography*, *32*(1), 231–236. https://doi.org/10.5670/oceanog.2019.105

Garrett, C. (2001). What is the "Near-Inertial" band and why is it different from the rest of the internal wave spectrum? *Journal of Physical Oceanography*, *31*(4), 962–971.

Geyer, W., Trowbridge, J. H., & Bowen, M. M. (2000). The dynamics of a partially mixed estuary. *Journal of Physical Oceanography*, *30*(8), 2025–2048.

Gostiaux, L., & Van Haren, H. (2010). Extracting meaningful information from uncalibrated backscattered echo intensity data. *Journal of Atmospheric and Oceanic Technology*, *27*(5), 943–949. https://doi.org/10.1175/2009jtecho704.1

Greene, A. D., Hendricks, P. J., & Gregg, M. C. (2015). Using an ADCP to estimate turbulent kinetic energy dissipation rate in sheltered coastal waters. *Journal of Atmospheric and Oceanic Technology*, *32*(2), 318–333. https://doi.org/10.1175/jtech-d-13-00207.1

Guerra, M., & Thomson, J. (2017). Turbulence Measurements from Five-Beam Acoustic Doppler Current Profilers. *Journal of Atmospheric and Oceanic Technology*, *34*(6), 1267–1284. https://doi.org/10.1175/jtech-d-16-0148.1

Kadaster. (2022). *Hydrografie (INSPIRE geharmoniseerd)* [Dataset; WMS]. Nationaal georegister. https://service.pdok.nl/kadaster/hy/wms/v1_0?request=GetCapabilities&service=WMS

Kadaster. (2023). *Zeegebieden (INSPIRE geharmoniseerd)* [Dataset; WMS]. Nationaal georegister. https://service.pdok.nl/kadaster/sr/wms/v1_0?request=GetCapabilities&service=WMS

KNMI. (2024). *Daggegevens van het weer in Nederland* [Dataset]. https://www.knmi.nl/nederland-nu/klimatologie/daggegevens

Korotenko, K. A., Sentchev, A., Schmitt, F. G., & Jouanneau, N. (2013). Variability of turbulent quantities in the tidal bottom boundary layer: Case study in the eastern English Channel. *Continental Shelf Research*, *58*, 21–31. https://doi.org/10.1016/j.csr.2013.03.001

Kranenburg, W., Tiessen, M., Blaas, M., & Van Veen, N. P. (2023). Circulation, stratification and salt dispersion in a former estuary after reintroducing seawater inflow. *Estuarine, Coastal and Shelf Science*, *282*, 108221. https://doi.org/10.1016/j.ecss.2023.108221

Krvavica, N., Travaš, V., & Ožanić, N. (2016). A field study of interfacial friction and entrainment in a microtidal salt-wedge estuary. *Environmental Fluid Mechanics*, *16*(6), 1223–1246. https://doi.org/10.1007/s10652-016-9480-1

Lange, X., Klingbeil, K., & Burchard, H. (2020). Inversions of estuarine circulation are frequent in a weakly tidal estuary with variable wind forcing and seaward salinity fluctuations. *Journal of Geophysical Research: Oceans*, *125*(9). https://doi.org/10.1029/2019jc015789

Lewis, P. (1970). Remarks on the theory, computation and application of the spectral analysis of series of events. *Journal of Sound and Vibration*, *12*(3), 353–375. https://doi.org/10.1016/0022-460x(70)90077-5

MacDonald, D. G., & Geyer, W. R. (2004). Turbulent energy production and entrainment at a highly stratified estuarine front. *Journal of Geophysical Research*, *109*(C5). https://doi.org/10.1029/2003jc002094

Nortek. (2017). *Signature principles of operation* (No. N3015-009 1). Retrieved December 29, 2023, from https://www.nortekgroup.com/assets/software/N3015-011-SignaturePrinciples.pdf

Nortek. (2023, December 20). *What is bin mapping?* Nortek Support Center. Retrieved December 29, 2023, from https://support.nortekgroup.com/hc/en-us/articles/8161198775452-What-is-bin-mapping-

O'Higgins, T. G., Lago, M., & DeWitt, T. H. (2020). Using the concepts and tools of social ecological systems and ecosystem services to advance the practice of ecosystem-based management. In *Ecosystem-based management, ecosystem services and aquatic biodiversity* (pp. 3–14). Springer. https://doi.org/10.1007/978-3-030-45843-0

Osalusi, E., Side, J. C., & Harris, R. E. (2009). Reynolds stress and turbulence estimates in bottom boundary layer of Fall of Warness. *International Communications in Heat and Mass Transfer*, *36*(5), 412–421. https://doi.org/10.1016/j.icheatmasstransfer.2009.02.004

Petrie, J., & Diplas, P. (2015). Evaluation of the Logarithmic Law of the wall for river flows. *River Research and Applications*, *32*(5), 1082–1093. https://doi.org/10.1002/rra.2920

Reeze, B. (2016, June). *Vismigratie kalender Haringvliet*. Bart Reeze Water & Ecologie. https://waterecologie.nl/portfolio/vismigratiekalender-haringvliet/

Rijkswaterstaat. (n.d.-a). *Kier Data Tool*. Waterberichtgeving. Retrieved April 28, 2024, from https://waterberichtgeving.rws.nl/wb/kier/

Rijkswaterstaat. (n.d.-b). *Waterinfo*. Retrieved April 28, 2024, from https://waterinfo.rws.nl/#/nav/index

Rijkswaterstaat. (2023a). *Actueel Hoogtebestand Nederland (AHN)* [WMS]. https://service.pdok.nl/rws/ahn/wms/v1_0?SERVICE=WMS&request=GetCapabilities

Rijkswaterstaat. (2023b). *WNZ zuid NAP* [Dataset; WMS]. https://geo.rijkswaterstaat.nl/services/ogc/gdr/bodemhoogte_1mtr/ows?version=1.3.0.

Rijkswaterstaat. (2023c, June 12). *Haringvliet: Haringvlietsluizen op een kier*. Rijkswaterstaat Ministerie Van Infrastructuur En Waterstaat. Retrieved December 11, 2023, from https://www.rijkswaterstaat.nl/water/projectenoverzicht/haringvliet-haringvlietsluizen-op-een-kier

Robinson, S. (2014). *Simulation The practice of model development and use* (2nd ed.). Red globe press. ISBN 9781373232802

Roos, P. C., Hulscher, S. J., & De Vriend, H. (2008). Modelling the morphodynamic impact of offshore sandpit geometries. *Coastal Engineering*, *55*(9), 704–715. https://doi.org/10.1016/j.coastaleng.2008.02.019

Salas-Monreal, D., & Valle-Levinson, A. (2009). Continuously stratified flow dynamics over a hollow. *Journal of Geophysical Research*, *114*(C3). https://doi.org/10.1029/2007jc004648

Seuront, L. (2008). Microscale complexity in the ocean: turbulence, intermittency and plankton life. *Mathematical Modelling of Natural Phenomena*, *3*(3), 1–41. https://doi.org/10.1051/mmnp:2008063

Simpson, J. H., Brown, J., Matthews, J., & Allen, G. (1990). Tidal straining, density currents, and stirring in the control of estuarine stratification. *Estuaries*, *13*(2), 125–132.

Simpson, J. H., Fisher, N. R., & Wiles, P. J. (2004). Reynolds stress and TKE production in an estuary with a tidal bore. *Estuarine, Coastal and Shelf Science*, *60*(4), 619–627. https://doi.org/10.1016/j.ecss.2004.03.006

Stacey, M. T., Monismith, S. G., & Burau, J. R. (1998). Observations of Turbulence in a partially stratified estuary. *Journal of Physical Oceanography*, *29*(8), 1950–1969.

Stacey, M. T., Monismith, S. G., & Burau, J. R. (1999). Measurements of Reynolds stress profiles in unstratified tidal flow. *Journal of Geophysical Research*, *104*(C5), 10933–10949. https://doi.org/10.1029/1998jc900095

Sullivan, G. D., & List, E. J. (1994). On mixing and transport at a sheared density interface. *Journal of Fluid Mechanics*, *273*, 213–239. https://doi.org/10.1017/s0022112094001916

Teledyne RD Instruments. (2011). Acoustic Doppler current profiler principles of operation a practical primer. In *Teledyne Marine*. https://www.teledynemarine.com/en-us/support/SiteAssets/RDI/Manuals%20and%20Guides/General%20Interest/BBPRIME.pdf

Terekhov, V. I., Dyachenko, A. Y., Smulsky, Y. J., Bogatko, T. V., & Yarygina, N. I. (2022). Flow separation in the field of the longitudinal pressure gradient. In *Heat transfer in subsonic separated flows* (pp. 179–202). Springer Nature. https://doi.org/10.1007/978-3-030-94557-2

Unesco. (1991). *Processing of oceanographic station data*. United Nations Educational Scientific and Cultural Organization. ISBN 92-3-102756-5

Van Der Nat, A., Vellinga, P., Leemans, R., & Van Slobbe, E. (2016). Ranking coastal flood protection designs from engineered to nature-based. *Ecological Engineering*, *87*, 80–90. https://doi.org/10.1016/j.ecoleng.2015.11.007

Van Gastel, P., & Pelegrí, J. L. (2004). Estimates of gradient Richardson numbers from vertically smoothed data in the Gulf Stream region. *Scientia Marina*, *68*(4), 459–482. https://doi.org/10.3989/scimar.2004.68n4459

Vermeulen, B. (2023). *adcptools* (Version 1) [Software]. Matworks file exchage. https://github.com/bartverm/adcptools

Wells, M. G., & Troy, C. D. (2022). Surface mixed layers in lakes. *Encyclopaedia of Inland Waters*, *1*(2), 546–561. https://doi.org/10.1016/b978-0-12-819166-8.00126-2

Western, A. W., Nolan, J. B., Hughes, R. L., & O'Neill, I. C. (1998). Mixing behaviour of density stratified pools. *Journal of Hydraulic Engineering*, *124*(3), 280–287.

Wiles, P. J., Rippeth, T. P., Simpson, J. H., & Hendricks, P. J. (2006). A novel technique for measuring the rate of turbulent dissipation in the marine environment. *Geophysical Research Letters*, *33*(21). https://doi.org/10.1029/2006gl027050

Zheng, Z., Fu, Y., Liu, K., Xiao, R., Wang, X., & Shi, H. (2018). Three-stage vertical distribution of seawater conductivity. *Scientific Reports*, *8*(1). https://doi.org/10.1038/s41598-018-27931-y

Appendix 1 From Reynolds covariance to TKE production rate

The steps presented in Stacey et al. (1999) and De Serio and Mossa (2014) for an RDI ADCP are repeated here for the Signature ADCP to motivate the choice of the sign convention for $\overline{u'w'}$ and $\overline{v'w'}$. These insights are subsequently useful to give further clarification about the practical application of the production rate equation.

Deriving the Guerra and Thomson (2017) $\overline{u'w'}$ based upon the steps of Stacey et al. (1999)

The Signature ADCP has positive along beam velocities pointing away from the instrument. The axis system is positioned at the ADCP as shown in Figure 73 as previously introduced in Figure 11.

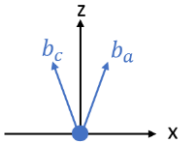

Figure 73: Schematic illustration of the along beam orientation, with respect to the axis system centered at the ADCP, as applies in Guerra and Thomson (2017). The angle between the z axis and each respective beam is θ.

Each along beam velocity consists of the sum of its projections onto the x and z axis. Therefore, the equations for b_a and b_c of Stacey et al. (1999) become, in the context of Figure 73, those of equations 24 and 25.

$$b_c = -u\sin(\theta) + w\cos(\theta) \quad (24)$$

$$b_a = u\sin(\theta) + w\cos(\theta) \quad (25)$$

Conform to the Reynolds decomposition the velocity consists of the sum of the mean and a fluctuating component. This allows to rewrite equations 24 and 25 to equations 26 and 27.

$$\overline{b_c} + b_c' = -(\bar{u} + u')\sin(\theta) + (\bar{w} + w')\cos(\theta) \quad (26)$$

$$\overline{b_a} + b_a' = (\bar{u} + u')\sin(\theta) + (\bar{w} + w')\cos(\theta) \quad (27)$$

Focusing on the fluctuating part allows, for each beam, to take the mean of the square of its velocity fluctuations over a certain time frame. This gives the along beam variances shown in equations 28 and 29.

$$\overline{b'_c b'_c} = \overline{u'}\sin^2(\theta) + \overline{w'}\cos^2(\theta) - 2\overline{u'w'}\sin(\theta)\cos(\theta) \quad (28)$$

$$\overline{b'_a b'_a} = \overline{u'}\sin^2(\theta) + \overline{w'}\cos^2(\theta) + 2\overline{u'w'}\sin(\theta)\cos(\theta) \quad (29)$$

Taking the difference between these along beam variances gives equation 30 that rearranges to equation 31. Thereby it should be noted that the order of subtraction does not alter the result.

$$\overline{b'_c b'_c} - \overline{b'_a b'_a} = -4\overline{u'w'}\sin(\theta)\cos(\theta) \quad (30)$$

$$\overline{u'w'} = \frac{\overline{b'_a b'_a} - \overline{b'_c b'_c}}{4\sin(\theta)\cos(\theta)} \quad (31)$$

Equation 31 is the same as the simplified equation of as Guerra and Thomson (2017) that is instead written in the format of equation 32 in Section 2.5 where it is referred to as equation 11.

$$\overline{u'w'} = -\frac{\overline{b_c'^2} - \overline{b_a'^2}}{4\sin(\theta)\cos(\theta)} \quad (32)$$

While it can thus be shown how this equation is obtained, there is a problem with it regarding its interpretation. Indeed, the formulation implies that if the flow is along the positive x axis direction and turbulence increases along that same orientation it follows that the along beam velocity variance at beam

a, denoted $\overline{b_a'^2}$ exceeds that of beam c referred to with $\overline{b_c'^2}$. Accordingly, the $\overline{u'w'}$ result is positive. The turbulent stress $-\rho\overline{u'w'}$ then takes a negative value. This appears contradictory with the increased turbulence, reflected by the increase in variance. Indeed, this poses a problem in the TKE production rate equation where $-\overline{u'w'}\frac{\delta u}{\delta z}$ is used. Indeed, with standard positive velocity profiles expected for a stratified water column, such as shown in the first window of Figure 75, the $\frac{\delta u}{\delta z}$ would be positive too, resulting in a negative production value.

Changing the Stacey et al. (1999) $\overline{u'w'}$ for an RDI ADCP to that for a Signature instrument

To demonstrate how the brought forward problem is created, the set up of Stacey et al. (1999) needs to be analogously considered. Next to having an RDI ADCP, its downwards orientation is another difference that sets it apart from Guerra and Thomson (2017) who deployed their Signature ADCP looking upwards. This is shown in Figure 74. One could make the observation that the beams are just mirrored while the ADCP is rotated. However, this action of making the ADCP downwards facing, can only be done by rotating it either around the y or x axis such that it always follows that one beam pair appears mirrored while the other rotated alongside with its corresponding axis orientation.

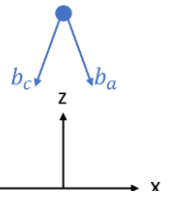

Figure 74: The Figure 73 equivalent but with the same set up as Stacey et al. (1999) here shown for a Signature ADCP.

Applying the same derivation as Stacey et al. (1999) on Figure 74 is equivalent to taking their equations with the sign of the along beam velocities reversed due to the difference between the RDI and Signature ADCPs. Accordingly this gives equations 33 and 34 as replacements for the previously used equations 24 and 25.

$$b_c = -u\sin(\theta) - w\cos(\theta) \tag{33}$$

$$b_a = u\sin(\theta) - w\cos(\theta) \tag{34}$$

Applying upon these the same steps as shown previously from equation 26 to 30 instead leads to equation 35.

$$\overline{u'w'} = \frac{-\overline{b'_a b'_a} + \overline{b'_c b'_c}}{4\sin(\theta)\cos(\theta)} \tag{35}$$

This is exactly the same as the formulation presented in Stacey et al. (1999) as equation 36 even if they considered the along beam velocities towards the ADCP.

$$\overline{u'w'} = \frac{\overline{b_c'^2} - \overline{b_a'^2}}{4\sin(\theta)\cos(\theta)} \tag{36}$$

The in equation 36 shown order of $\overline{b_a'^2}$ and $\overline{b_c'^2}$ is desirable because under conditions that the variance increases along a positively oriented flow, the result of $\overline{u'w'}$ is negative. As such this leads to a positive production rate as is expected for such a situation.

Comparing the two derivations of $\overline{u'w'}$

Obtaining equation 36, that is identical to the result of Stacey et al. (1999), could only be expected because naturally the along beam directionality of the velocity does not affect the value of the along beam variance. This is why in the example based upon Figure 74 it is specifically chosen to use the mirrored counter part of the ADCP beam positions with respect to the axis from Figure 73. If instead the rotation

around the y axis option is used, instead of the currently exemplified rotation around the x axis, it would follow that the b_c and b_a are switched in the figure but consequently also the $\overline{b_c'^2}$ and $\overline{b_a'^2}$ in equation 36. Thereby this provides the equivalent result to equation 31.

Equations 24 and 25 can produce identical results to equations 33 and 34 given the same inputs framed around their respective systems as schematized by Figure 73 and Figure 74. This however does not hold true for their respectively derived Reynolds covariances equations because the along beam velocity variances included in those are always positive. Indeed, only keeping the fluctuating parts of equations 26 and 27 makes that the inputs are always positive while the signs in between the terms are still for adaptive input directionalities. Therefore, it seems more suitable to actually fix the subtraction direction employed in equation 30 and use only positive sings in between the terms of the input equations. Indeed, while currently the subtraction direction does not alter the result, it dictates the sign of $\overline{u'w'}$ if no subtraction signs return in the equations of $\overline{b'_c b'_c}$ and $\overline{b'_a b'_a}$. The subtraction order should be based upon the beam positioning in the context of the positive axis orientation. Thereby subtracting the beam that that is further towards the positive axis side from the one that is further towards the negative axis side.

There are no complications for the normal Reynolds covariances. Indeed, the vertical $\overline{w'w'}$ is only based upon the variance of the vertical beam velocity. Further because $\overline{u'u'}$ and $\overline{v'v'}$ are calculated from the addition of the along beam variances of opposite beams (Dewey & Stringer, 2007) it follows that it is irrelevant for which beam of the pair the $2\overline{u'w'}\sin(\theta)\cos(\theta)$ part of the covariance equation, like those of equation 26 and 27, it is negative. Indeed because one of the pair will be negative while the other positive the concerned portion cancels in the addition.

For the TKE production rate a further intervention on its sign is proposed

In the equation of the TKE production rate the negative Reynolds covariance and the gradient along the profile of the corresponding velocity component dictates the sign of the result. For the basic case velocity profiles shown in Figure 75 it is considered that the variance in velocity increases along the flow direction. This can be observed with the ADCP because of the horizontal separation of the position sampled by a pair of opposite slanted beams. It would follow that $\overline{u'w'}$ and $\frac{\delta u}{\delta z}$ have opposite signs such that a positive production follows from $P = -\overline{u'w'}\frac{\delta u}{\delta z}$. Therefore the increase in variance in velocity is linked to the increase in turbulence suggested by the positive TKE production rate which follows from a positive turbulent or Reynolds stress $-\rho\overline{u'w'}$.

Despite that the production equation applies in line with the expectations for basic cases, this is different when situations are encountered where the flow direction changes along the water column as is shown in the most right window of Figure 75. There is not always the opposition in sign that leads to

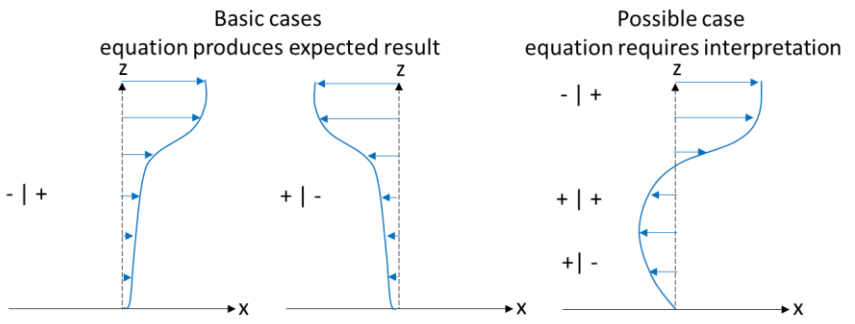

Figure 75: Schematic velocity profiles with associated signs of $\overline{u'w'}$ | $\frac{\delta u}{\delta z}$ considering that the variance in velocity increases with the flow direction.

a positive P. However such negative values for production do not have the same meaning as ones related to conditions where the variance in velocity actually decreases with the flow direction. Therefore it is proposed to calculate the production rate along an axis component based upon the product between the Reynolds covariance and the along depth velocity gradient of the profile while only subsequently accord the positive or negative sign to P based upon if respectively the observed along beam variance increases with the flow direction or not.

Appendix 2 Inventory of found instrument positioning characteristics

An overview of the valid portion of the raw data used and the derived details from the instrument positioning are provided from Table 2 to Table 5.

Table 2: Overview of the available time range and position for each ADCP alongside the derived orientation characteristics.

		ADCP Signature properties		ADCP RDI properties	
		ADCP1 1000kHz	ADCP2 1000kHz	ADCP3 600kHz	ADCP4 1200kHz
Period 1					
Longitude		4° 4.997′ E	4° 5.097′ E	4° 5.534′ E	4° 6.361′ E
Latitude		51° 49.072′ N	51° 49.033′ N	51° 48.842′ N	51° 48.217′ N
Mean heading	deg	259.49	173.44	326.99	162.41
Vertical cells used		50	50	11	17
Vertical cells used echosounder beam		300	300		
Start time		10-Nov-2022 11:39:59	10-Nov-2022 10:39:59	10-Nov-2022 10:00:00	10-Nov-2022 13:10:00
End time		19-Dec-2022 12:27:07	19-Dec-2022 11:05:21	19-Dec-2022 13:20:00	19-Dec-2022 14:00:00
Orientation PC1 (w.r.t x instrument axis)	deg	-43.78	51.40	23.63	21.04
Variance explained PC1	%	74.16	71.87	69.23	96.84
Heading PC1 (w.r.t North)	deg	303.27	302.04	303.36	321.37
Selected x axis orientation (w.r.t North)	deg	303.50	303.50	302.13	310.25
Period 2					
Longitude		4° 4.997′ E	4° 5.097′ E	4° 5.534′ E	4° 6.361′ E
Latitude		51° 49.072′ N	51° 49.033′ N	51° 48.842′ N	51° 48.217′ N
Mean heading	deg	170.51	104.65	327.6	88.25
Vertical cells used		50	50	11	17
Vertical cells used echosounder beam		300	300		
Start time		20-Dec-2022 11:20:19	20-Dec-2022 10:40:10	20-Dec-2022 09:10:00	20-Dec-2022 14:30:00
End time		23-Jan-2023 13:04:23	23-Jan-2023 14:26:44	23-Jan-2023 15:20:00	23-Jan-2023 17:00:00
Orientation PC1 (w.r.t x instrument axis)	deg	42.91	-16.44	26.70	-30.99
Variance explained PC1	%	96.72	96.61	94.57	98.74
Heading PC1 (w.r.t North)	deg	307.60	301.09	300.90	299.24
Selected x axis orientation (w.r.t North)	deg	303.50	303.50	302.13	310.25
Period 3					
Longitude		4° 7.229′ E	4° 7.423′ E	4° 8.084′ E	4° 6.361′ E
Latitude		51° 47.844′ N	51° 47.776′ N	51° 47.567′ N	51° 48.217′ N
Mean heading	deg	91.55	83.44	161.16	123.02
Vertical cells used		48	48	12	17
Vertical cells used echosounder beam		288	288		
Start time		24-Jan-2023 10:16:09	24-Jan-2023 13:43:18	24-Jan-2023 12:10:00	24-Jan-2023 11:10:00
End time		15-Mar-2023 10:43:11	15-Mar-2023 13:15:41	15-Mar-2023 11:20:00	15-Mar-2023 15:00:00
Orientation PC1 (w.r.t x instrument axis)	deg	-32.71	-38.90	48.27	-7.12
Variance explained PC1	%	93.21	94.98	94.90	95.39
Heading PC1 (w.r.t North)	deg	304.26	302.34	292.89	310.14
Selected x axis orientation (w.r.t North)	deg	303.50	303.50	292.89	310.25

Table 3: The time of the available CTD profiles and that of the closest corresponding ADCP time of which the pressure is used to obtain an estimate of the depth difference between the Signature instruments.

	Signature ADCP 1	Signature ADCP 2	
Period 1			
Start time	10-Nov-2022 11:25:17	10-Nov-2022 10:29:34	
End time	10-Nov-2022 11:26:35	10-Nov-2022 10:31:00	
Central time of 10 min window	10-Nov-2022 11:45:00	10-Nov-2022 10:45:00	
Pressure Signature ADCP	16.73	16.83	dbar
Estimated ADCP depth from pressure	17.06	17.14	m
Depth difference (HV2 -/- HV1) from pressure	0.08		m
Depth difference (HV2 -/- HV1) from echosounder	0.00		m
Period 2			
Start time	20-Dec-2022 11:09:27	20-Dec-2022 10:32:18	
End time	20-Dec-2022 11:10:10	20-Dec-2022 10:33:27	
Central time of 10 min window	20-Dec-2022 11:22:00	20-Dec-2022 10:44:46	
Pressure Signature ADCP	16.30	16.49	dbar
Estimated ADCP depth from pressure	16.59	16.78	m
Depth difference (HV2 -/- HV1) from pressure	0.19		m
Depth difference (HV2 -/- HV1) from echosounder	0.10		m
Period 3			
Start time	24-Jan-2023 10:20:21	24-Jan-2023 10:42:40	
End time	24-Jan-2023 10:21:56	24-Jan-2023 10:42:49	
Central time of 10 min window	24-Jan-2023 10:26:20	24-Jan-2023 10:47:22	
Pressure Signature ADCP	16.03	15.60	dbar
Estimated ADCP depth from pressure	16.33	15.89	m
Depth difference (HV2 -/- HV1) from pressure	-0.44		m
Depth difference (HV2 -/- HV1) from echosounder	-0.45		m

Table 4: Invalid time entries present during the first monitoring period.

	Signature ADCP 1	Signature ADCP 2
Segment of missing data followed by extreme pitch, roll and heading that then gradually tend back to the average level.		
Start Time	22-Nov-2022 11:57:36	19-Nov-2022 15:10:17
End Time	22-Nov-2022 13:00:00	19-Nov-2022 16:24:39
Start Time	15-Dec-2022 09:20:04	01-Dec-2022 09:34:18
End Time	15-Dec-2022 10:07:09	01-Dec-2022 10:19:21
Start Time		05-Dec-2022 15:43:03
End Time		05-Dec-2022 16:19:50
Start Time		15-Dec-2022 06:36:55
End Time		15-Dec-2022 07:14:57
Start Time		16-Dec-2022 07:59:56
End Time		16-Dec-2022 11:13:58
Segment of missing data.		
Start Time		14-Dec-2022 23:59:55
End Time		15-Dec-2022 01:00:00
Start Time		18-Dec-2022 07:59:38
End Time		18-Dec-2022 09:00:00
Start Time		18-Dec-2022 15:59:22
End Time		18-Dec-2022 16:48:01
Two segments of missing data in between which there is a portion where the by the echosounder indicated heading, pitch and roll differs from the slanted and vertical beam, but not beyond the noise of the time series.		
Start Time		07-Dec-2022 23:19:04
End Time		08-Dec-2022 08:01:59

Table 5: The valid time range for the CTD time series, the used raw data sampling interval and the derived distance of each instrument to the closest positioned Signature ADCP.

		ctd a	ctd b	ctd c	
Period 1 Line 1					
Distance above ADCP 1		2.05	5.73	8.17	m
Interval sampling		60	60	60	s
Start Time	10/11/2022 13:50:00				
End Time	05/12/2022 14:20:00				
Period 1 Line 2					
Distance above ADCP 2		1.89	5.52	7.12	m
Interval sampling		60	60	60	s
Start Time	10/11/2022 12:30:00				
End Time	19/12/2022 11:00:00				
Period 2 Line 2					
Distance above ADCP 2		1.93		7.10	m
Interval sampling		10		10	s
Start Time	20/12/2022 13:00:00				
End Time	23/01/2023 14:00:00				
Period 3 Line 2					
Distance above ADCP 2		3.55		5.50	m
Interval sampling		10		10	s
Start Time	24/01/2023 11:20:00				
End Time	15/03/2023 14:10:00				

Appendix 3 CTD data to salinity and density

The empirical expressions from Unesco (1991) that allow to estimate the water salinity and density using CTD data are presented in the two sections below. Thereby, the standard conductivity of sea water with a salt content of 35 ppt for 15 degrees Celsius at atmospheric pressure, designated with $C_{35,15,0}$, is taken to be 4.2914 Simens/m according to Zheng et al. (2018). The original notation of Unesco (1991) is converted to one based upon matrices for conciseness while also edited to have consistent units of the quantities involved in the two expression sets that allow to derive salinity and density respectively.

Conductivity C [Simens/m], temperature T [°C] and pressure P [dbar] to salinity S [PSU]

Coefficient matrix

$$X = \begin{bmatrix} 0.008 & -0.1692 & 25.3851 & 14.0941 & -7.0261 & 2.7081 \\ 0.0005 & -0.0056 & -0.0066 & -0.0375 & 0.0636 & -0.0144 \\ 6.766097 * 10^{-1} & 2.00564 * 10^{-2} & 1.104259 * 10^{-4} & -6.9698 * 10^{-7} & 1.0031 * 10^{-9} & NaN \\ 3.426 * 10^{-2} & 4.464 * 10^{-4} & 4.215 * 10^{-1} & -3.107 * 10^{-3} & NaN & NaN \\ 2.07 * 10^{-5} & -6.37 * 10^{-10} & 3.989 * 10^{-15} & NaN & NaN & NaN \end{bmatrix}$$

Expressions

$$\begin{bmatrix} a \\ b \\ c \\ d \\ e \end{bmatrix} = \begin{bmatrix} a_0 & a_1 & a_2 & a_3 & a_4 & a_5 \\ b_0 & b_1 & b_2 & b_3 & b_4 & b_5 \\ c_0 & c_1 & c_2 & c_3 & c_4 & c_5 \\ d_0 & d_1 & d_2 & d_3 & d_4 & d_5 \\ e_0 & e_1 & e_2 & e_3 & e_4 & e_5 \end{bmatrix} = X$$

$$R = \frac{C_{S,T,P}}{C_{35,15,0}}$$

$$r_T = \sum_{n=0}^{4} c_n T^n$$

$$R_P = \frac{e \cdot [P, P^2, P^3]}{1 + d \cdot [T, T^2, R, TR]}$$

$$R_T = \frac{R}{r_T R_P}$$

$$S = \sum_{n=0}^{5} \left(a_n + \frac{T - 15}{1 + 0.0162 * (T - 15)} b_n \right) R_T^{n/2}$$

Temperature T [°C], pressure P [dbar] and salinity S [PSU] to density ρ [kg/m^3]

Coefficient matrix

$$X = \begin{bmatrix} 9.99842594 * 10^{2} & 6.793953 * 10^{-2} & -9.09529 * 10^{-3} & 1.001685 * 10^{-4} & -1.120083 * 10^{-6} & 6.536332 * 10^{-9} \\ 8.2449 * 10^{-1} & -4.0899 * 10^{-3} & 7.6438 * 10^{-5} & -8.2467 * 10^{-7} & 5.3875 * 10^{-9} & \text{NaN} \\ -5.7246 * 10^{-3} & 1.0227 * 10^{-4} & -1.6546 * 10^{-6} & \text{NaN} & \text{NaN} & \text{NaN} \\ 4.8314 * 10^{-4} & \text{NaN} & \text{NaN} & \text{NaN} & \text{NaN} & \text{NaN} \\ 1.965221 * 10^{4} & 1.484206 * 10^{2} & -2.327105 * 10^{0} & 1.360477 * 10^{-2} & -5.155288 * 10^{-5} & \text{NaN} \\ 5.46746 * 10^{1} & -6.03459 * 10^{-1} & 1.09987 * 10^{-2} & -6.167 * 10^{-5} & \text{NaN} & \text{NaN} \\ 7.944 * 10^{-2} & 1.6483 * 10^{-2} & -5.3009 * 10^{-4} & \text{NaN} & \text{NaN} & \text{NaN} \\ 3.2399 * 10^{0} & 1.43713 * 10^{-3} & 1.16092 * 10^{-4} & -5.77905 * 10^{-7} & \text{NaN} & \text{NaN} \\ 2.2838 * 10^{-3} & -1.0981 * 10^{-5} & -1.6078 * 10^{-6} & \text{NaN} & \text{NaN} & \text{NaN} \\ 1.91075 * 10^{-4} & \text{NaN} & \text{NaN} & \text{NaN} & \text{NaN} & \text{NaN} \\ 8.50935 * 10^{-5} & -6.12293 * 10^{-6} & 5.2787 * 10^{-8} & \text{NaN} & \text{NaN} & \text{NaN} \\ -9.9348 * 10^{-7} & 2.0816 * 10^{-8} & 9.1687 * 10^{-10} & \text{NaN} & \text{NaN} & \text{NaN} \end{bmatrix}$$

Expressions

$$\begin{bmatrix} a \\ b \\ c \\ d \\ e \\ f \\ g \\ h \\ i \\ j \\ m \\ n \end{bmatrix} = \begin{bmatrix} a_0 & a_1 & a_2 & a_3 & a_4 & a_5 \\ b_0 & b_1 & b_2 & b_3 & b_4 & b_5 \\ c_0 & c_1 & c_2 & c_3 & c_4 & c_5 \\ d_0 & d_1 & d_2 & d_3 & d_4 & d_5 \\ e_0 & e_1 & e_2 & e_3 & e_4 & e_5 \\ f_0 & f_1 & f_2 & f_3 & f_4 & f_5 \\ g_0 & g_1 & g_2 & g_3 & g_4 & g_5 \\ h_0 & h_1 & h_2 & h_3 & h_4 & h_5 \\ i_0 & i_1 & i_2 & i_3 & i_4 & i_5 \\ j_0 & j_1 & j_2 & j_3 & j_4 & j_5 \\ m_0 & m_1 & m_2 & m_3 & m_4 & m_5 \\ n_0 & n_1 & n_2 & n_3 & n_4 & n_5 \end{bmatrix} = X \quad , \quad \begin{bmatrix} A \\ B \\ C \\ D \\ E \\ F \\ G \\ H \\ I \\ J \\ M \\ N \end{bmatrix} = X * \begin{bmatrix} T^0 \\ T^1 \\ T^2 \\ T^3 \\ T^4 \\ T^5 \end{bmatrix}$$

$$K_{S,T,P} = E + FS + GS^{\frac{3}{2}} + (H + IS + JS^{\frac{3}{2}})(0.1P) + (M + NS)(0.1P)^2$$

$$\rho_{S,T,0} = A + BS + CS^{3/2} + DS^2$$

$$\rho_{S,T,P} = \frac{\rho_{S,T,0}}{1 - \frac{0.1P}{K_{S,T,P}}}$$